SCATTERING OF ALPHA PARTICLES FROM ^{20}Ne

William Patrick Bourke

A Thesis Submitted for the
Degree of Doctor of Philosophy
in the Australian National University

October 1968

The studies described in this thesis have been carried out in the Department of Nuclear Physics of the Australian National University. The experimental work employed the major facility of the laboratory - the model EN tandem accelerator.

The study of alpha scattering from ^{20}Ne was suggested to me by my supervisor, Dr Jan Nurzynski.

The experimental work was jointly conducted by myself and Dr Nurzynski with some assistance during the initial measurements from Dr Kevin Bray who was then a fellow student.

The data reduction and theoretical analysis represent my own endeavours.

No part of this thesis has been submitted for a degree at any other university.

William Bourke.

ACKNOWLEDGEMENTS

It is with pleasure that I acknowledge that the experimental studies described in this thesis depended on the close collaboration between my supervisor Dr Nurzynski and myself. In addition I am grateful to Dr Nurzynski for discussion of many facets of this work and for arranging with Dr Tamura and Dr Perey of the Oak Ridge Laboratory for copies of their codes to be sent to us.

I would like to thank the technical staff for their assistance in running the accelerator and Mr C. Hill who implemented the modifications to the negative ion source at the instigation of Dr Ophel.

I am grateful to Dr Kevin Bray for assistance in the initial stages of the experiment and to Dr P. Young for guidance in initial usage of the gas cell and gas handling facilities which were in the main inherited from him.

I am particularly grateful to Dr Tamura for several communications clarifying the formulation of his code and for his co-operation in verifying the accuracy of one of the present calculations, and to Dr Ivascu for communicating his results.

Thanks are due to Dr Nurzynski, Dr Ophel and Dr Treacy for comments on differing aspects of this thesis and to Dr Barker, Dr Robson and Dr Treacy for illuminating discussion of a number of theoretical details.

The use of the IBM 360/50 facilities in hours and in particular out of hours was essential to these studies and thanks are offered to the computer centre staff for the availability of the computer. The expertise of my fellow student Mr C. Osman in computer job control language greatly facilitated my re-arrangement of the coupled channels code and I would like in addition to thank him for his interest in and discussion of my studies. The kinematics codes, coulomb function codes and the fitting code were readily explained and made available by Dr Hay of this laboratory.

I would like to thank Professor Titterton for the opportunity to carry out these studies. Financial assistance of the Commonwealth Government and the Australian National University is gratefully acknowledged.

I would like to offer particular thanks to my fiancee Miss Robin Pooley for her excellent typing of this thesis.

CONTENTS

CHAPTER 1

Introduction

The studies described in this thesis have been concerned with experimental and theoretical aspects of elastic and inelastic scattering of alpha particles from ^{20}Ne. The description of elastic and inelastic alpha scattering at energies somewhat in excess of those available from electrostatic accelerators ($\geq$28 MeV) has received considerable experimental and theoretical attention and is well described in terms of direct scattering models such as the optical model and diffraction model. An interpretation of alpha scattering at lower energies of <20 MeV, particularly on light nuclei, is rather more complicated by the influence of resonance effects. The prime interest of the present studies has been to consider the extent to which direct scattering contributes to the observed scattering at these lower energies.

At bombarding energies of <20 MeV elastic alpha scattering on a number of light nuclei such as ^{12}C, ^{16}O, ^{24}Mg, ^{26}Mg and ^{32}S has been measured in detail. The present measurements have been directed towards measuring both elastic and inelastic scattering in an attempt to define more clearly the role of direct scattering. The present target nucleus ^{20}Ne is particularly amenable to a consideration of inelastic scattering as a direct process since the ground state is strongly deformed and rotational excitations can be strongly coupled to the elastic scattering via simple and direct collective excitation.

An energy level diagram displaying the low lying levels of ^{20}Ne is shown in figure 1.1. In the present studies the cross sections for elastic scattering and scattering corresponding to excitation of the target nucleus to its first five excited states have been measured for bombarding alpha energies from ≈12 to 15 MeV. Throughout the thesis specification of scattering either elastic or that involving excitation is often referred to simply as the 0^+, 2^+, 4^+, 2^- or $(3^-,1^-)$ scattering; the 5·63 and 5·80 MeV states were unresolved in these measurements. Excitation of the 2^- unnatural parity state is of particular interest for reaction mechanism studies and, although not theoretically interpreted here, it was the subject of some experimental effort as there are virtually no measurements of such unnatural parity excitation at the present energies as far as is known to the author. The experimental facilities and techniques, the data reduction and obtained measurements are considered in chapters two, three and four.

The scattering of alpha particles such as in the present studies gives rise to excitations in the compound system at which the average level width $<\Gamma>$ is much greater than the average level spacing $<D>$. The appropriateness of this description of the level density at ≈20 MeV excitation in ^{24}Mg, as presently attained, is indicated by Vogt et al; a calculation considering only even spin states yielded

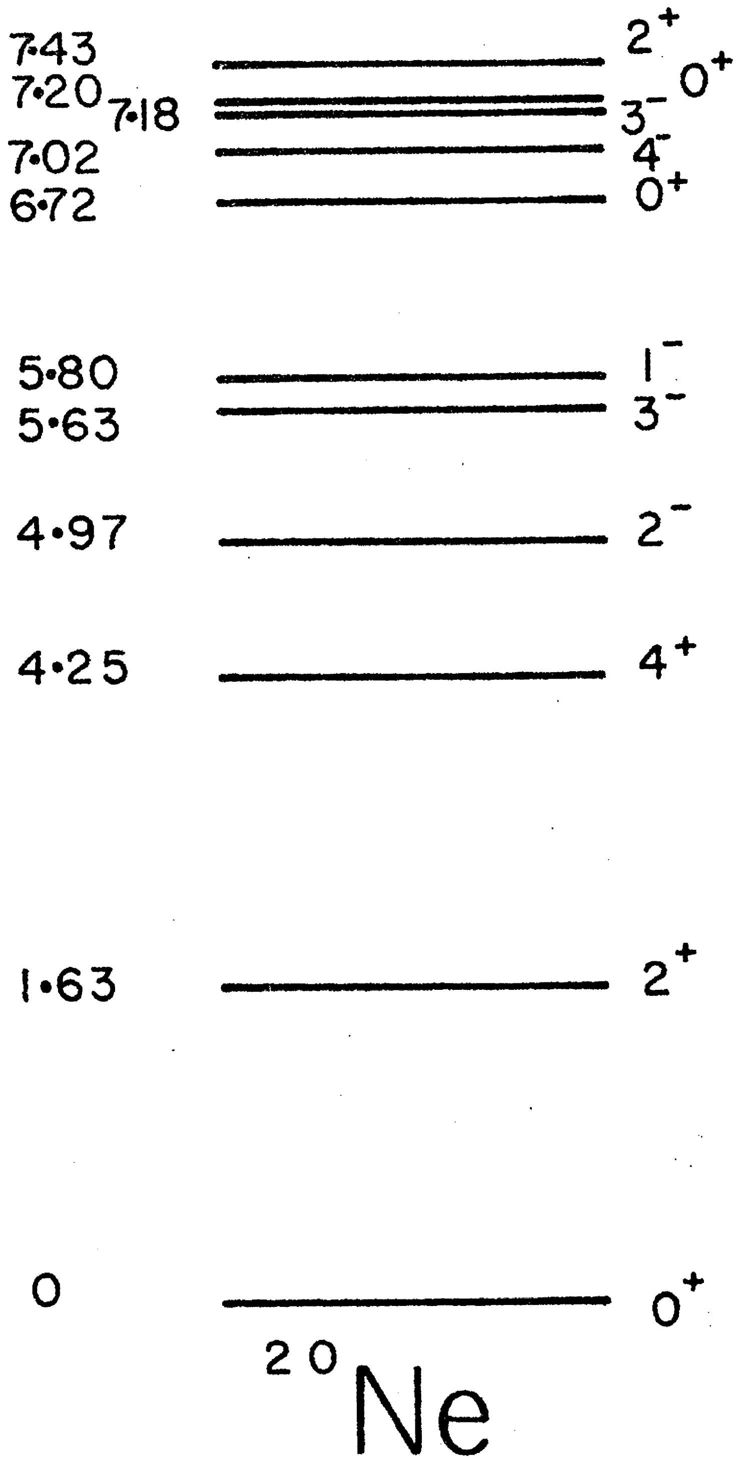

FIGURE 1.1 Low lying energy levels of ^{20}Ne; the energies in MeV and spin and parity of the states are shown.

$\langle\Gamma\rangle/\langle D\rangle > 17$ (Vo 64).

It could be expected at energies yielding excitations in the compound system for which $\langle\Gamma\rangle \gg \langle D\rangle$ that relatively energy-independent scattering as predicted by the one body optical potential would become evident. However random correlations between overlapping resonances may give, as is widely considered, statistical fluctuations and pronounced energy dependence of cross section (Er 66). Indeed the most obvious feature of elastic and inelastic scattering of alpha particles from light nuclei at the energies of the present measurements is the marked cross section energy dependence. Davis (Da 66) and Singh et al (Si 66) both suggest the formation of intermediate states as a possible explanation of the broader structure accompanying the finer structure apparent in the elastic scattering excitation functions. Moldauer (Mo[1] 67) has suggested that the structure designated as intermediate in the elastic scattering of alpha particles can arise from the more conventional statistical theories.

One method of theoretical interpretation of such energy dependent scattering is afforded by energy averaging either arithmetically or experimentally over resonance effects thus enabling a simpler study of direct and resonant amplitudes which can then be considered as incoherent. An alternative procedure which is consistent with a model proposed by Robson, as is discussed by Davis (Da 66), is to consider the energy dependence of cross section in terms of variations in the strength of the optical potential. This procedure permits the definition of an average optical potential such as would describe scattering unperturbed by resonance effects. This latter procedure has been considered in the analysis of the elastic scattering as is discussed in chapter five.

The theoretical analysis has been extended to consider the inelastic scattering as a means of defining the influence of direct scattering more precisely. This procedure is discussed in chapter six in terms of the extended optical model and resultant coupled channels formalism. Some detail of the formalism is discussed as it is considered to be the most rigorous approach presently adopted.

A procedure commonly employed in analyzing energy dependent data in which a direct scattering contribution is considered significant is to modify the direct scattering amplitude via a resonance term. As rather prominant resonance structure in the elastic scattering was apparent at ≈12·3 MeV bombarding energies of the present measurements some analysis was performed in which a Breit-Wigner resonant amplitude was added to an optical model scattering amplitude. This analysis is discussed in chapter seven. A procedure recently employed by Singh et al (Si 66) provides a particularly impressive account of resonance effects by phase shift fitting of the elastic scattering. Limited attempts to apply this type of analysis were made but in view of the complexity of fitting approximately 33 data points with up to 20 freely varying parameters the procedure was abandoned in favour of the above mentioned Breit-Wigner approach which was rather more constrained and consistent with the present attempts to consider a direct scattering contribution. A procedure of modifying a direct scattering amplitude via a resonance form was also considered by Carter et al (Ca 64) as a means of describing the elastic scattering of alpha particles on ^{12}C at energies of <20 MeV; the method required the addition of a resonance phase to diffraction model phases.

The final discussion in chapter eight presents a summary of the present studies.

CHAPTER 2

Experimental Facilities and Techniques

The scattering measurements to be described have employed the $^4He^{++}$ beam obtained by $^4He^-$ injection into the tandem van de Graaff accelerator. Solid state surface barrier detectors were used to observe the alpha particles scattered from ^{20}Ne gas contained in a thin windowed gas cell. The detector signals were fed via preamplifiers and amplifiers to multichannel analyzers and the accumulated spectra were recorded in printed and punched format.

2.1 Helium Beam

Until recently, acceptable beam currents of helium ions from tandem accelerators were most readily obtained by injection of neutral helium. A fraction of positive helium ions injected from a single-ended 500 kv van de Graaff accelerator through a gas exchange canal is neutralized and drifts to the high voltage terminal of the tandem where the ions are stripped of electrons and accelerated away from the terminal. Beam currents obtained in this way at the A.N.U. laboratory are typically 0·1 to 0·5 x 10^{-6} amps of $^4He^{++}$ in the energy range 2 to 12 MeV.

Negative helium ion injection can be achieved by using the duoplasmatron ion source in which ≈50 kv charge exchange of $^4He^+$ ions yields ≈100 kev $^4He^-$ ions. The advantage of using negative injection is that the energy obtainable is proportional to 3 x terminal volts since the ions are accelerated towards the terminal as well as away from it. The disadvantage has been that the yield of the negative ion employing the normal duoplasmatron ion source with hydrogen exchange gas is small.

Carter (Ca 62) described detailed studies of negative helium injection into a tandem accelerator. Using hydrogen exchange gas, which was found more satisfactory than either helium or air, beams from 4 to 13 x 10^{-9} amps of $^{4}He^{++}$ were obtained. More recently Holbrow et al (Ho 66) have obtained an analyzed $^{3}He^{++}$ beam of 400 x 10^{-9} amps. This improvement was primarily achieved by the addition of a plasma expansion cone at the exit of the extraction aperture of the source and by increasing the length of the exchange canal. $^{3}He^{++}$ and $^{4}He^{++}$ beam intensities were found to be comparable although the latter was less (Mi 67).

More significant improvements have been made recently using as exchange metallic vapour instead of hydrogen. Aldridge et al (Al 67), using potassium vapour exchange, obtained analyzed beams of 300 to 800 x 10^{-9} amps of $^{4}He^{++}$. Rose et al (Ro 67) achieved similar performance using a radio-frequency ion source with cesium vapour exchange. Middleton, with either potassium or lithium vapour exchange, obtained analyzed beams of $^{3}He^{++}$ and $^{4}He^{++}$ of several microamps.

The alpha beam employed in the measurements to be described was improved during the course of the experiment as a result of implementing some of the modifications described above. Initial measurements were carried out with beam intensities of 10 to 15 x 10^{-9} amps of $^{4}He^{++}$.

With the modified ion source, in which a plasma expansion cone was added and the length of the hydrogen gas exchange canal was increased, analyzed beams of $^{4}He^{++}$ of intensity 50 to 100 x 10^{-9} amps were available as a matter of course, the best performance being a beam of ≈150 x 10^{-9} amps. These beams were obtained by injection of from 150 to 300 x 10^{-9} amps of $^{4}He^{-}$. As commonly found, higher exchange voltage increased the yield and operation for the present measurements typically employed the available maximum of 50 kv. Middleton pointed out that independent power supplies for the extractor and exchange electrodes permit improved performance. Using hydrogen exchange gas he cited optimum performance with exchange voltages of 60 to 70 kv and extractor voltages of 48 to 50 kv.

Due to increased loading with helium source gases, a molybdenum tip was attached to the front of the extractor electrode as suggested by Middleton. An earlier modification suggested by High Voltage Corporation (HV 65) was also implemented; the mild steel end-plate confining the magnet coil surrounding the source filament was replaced with one of non-magnetic steel (HV 65). The improvement in beam intensity here was slight. The current required in this magnet for optimum beam conditions depended on the diameter of the extraction aperture. The best performance of 150 x 10^{-9} amps of $^4He^{++}$ on target was obtained with low magnet current which was indicative of an enlarged aperture.

2.2 Beam Transport

In the present experimental studies the two target rooms available in the laboratory were used. Beam transport from the accelerator to either room is achieved by +90° (-90°) deflection via an analyzing magnet with subsequent 20° (zero) deflection through a switching magnet to the scattering chamber of station one (station two); the scattering chambers of the two target stations are essentially identical. The typical beam energy resolution of electrostatic accelerators was obtainable and at energies in the range 12 to 15 MeV was considered to be within ±5 kev. The beam energy was determined by observing the frequency corresponding to proton nuclear magnetic resonance in the field of the 90° magnet. Feedback of the difference signal of the beam current on the two image slits to the corona stabilizer provided energy stability.

For most of the present measurements the object and image slit gaps of the 90° analyzing magnet were set at 2·5 and 2·0 mm respectively. Some initial measurements using slit settings of 7·5 and 2·5 mm (see section 4.1)

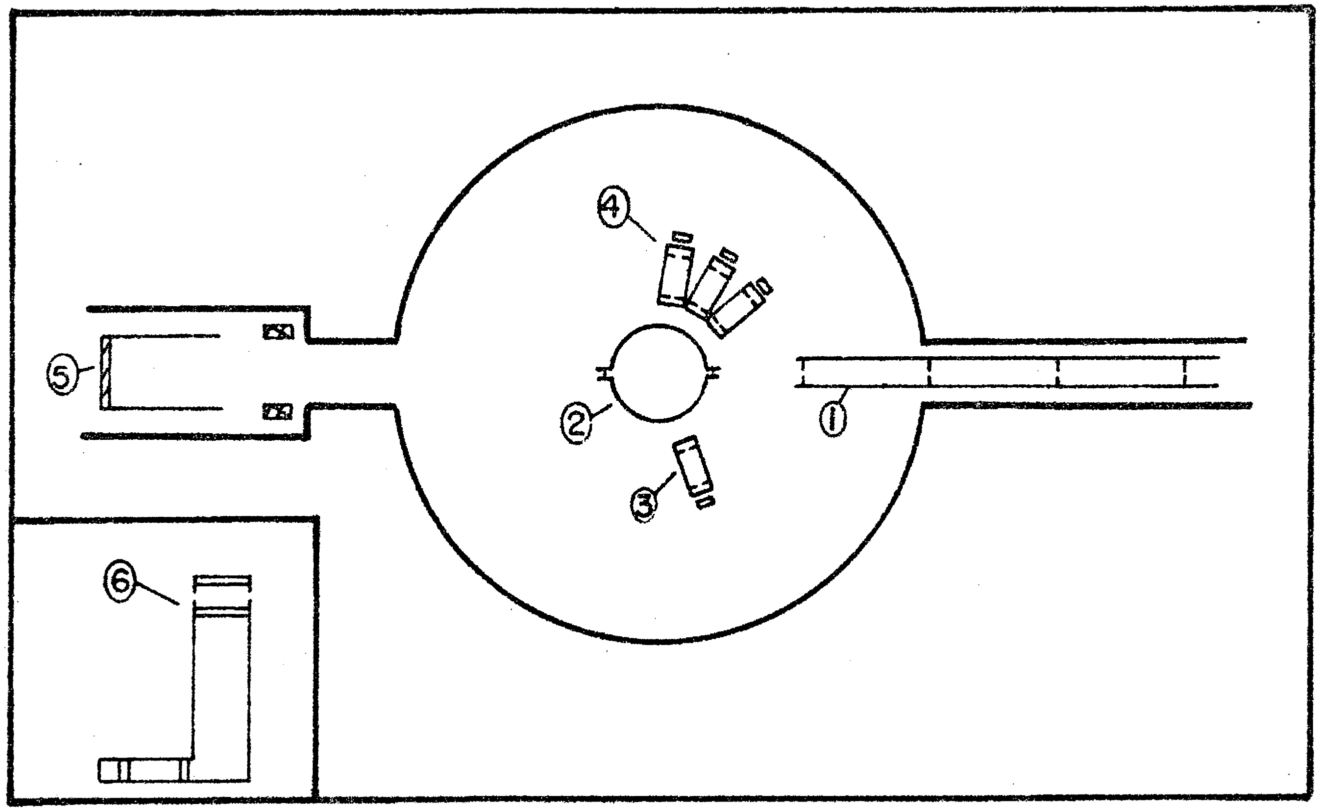

FIGURE 2.1 Horizontal cross section of scattering chamber gas cell and detector mounts. The numerals indicate :

1 collimator holder and tantalum collimators;
2 gas cell; 3 monitor counter;
4 triple detector array; 5 Faraday cup;
6 vertical cross section of a detector mount.

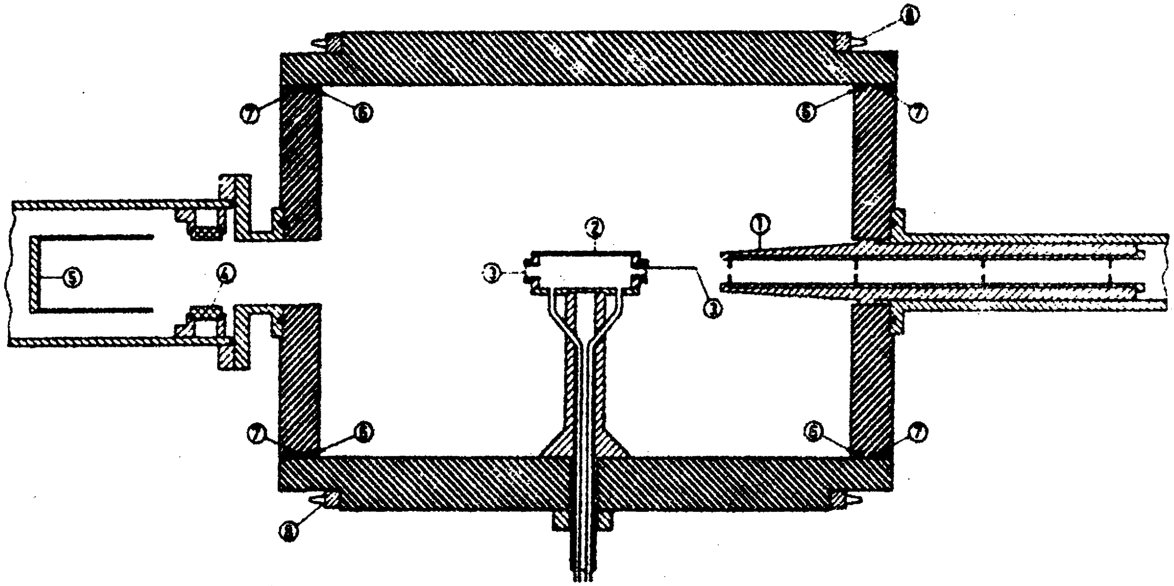

FIGURE 2.2 Vertical cross section of scattering chamber and gas cell. The numerals indicate :

1 the entrance port, collimator holder and tantalum collimators;
2 gas cell; 3 nickel entrance and exit windows of gas cell; 4 magnetic suppressor of Faraday cup; 5 Faraday cup; 6 top and bottom lid o-ring seals; 7 teflon lid bearings;
8 lid sprockets (rotation by chain drive).

Optical alignment of the chamber ensured precise correspondence of the beam axis and the axis of rotation of the detector assemblies together with accurate location of the zero of the angle scale of the chamber. Subsequent checks by several groups in the laboratory indicated that this alignment located the "zero" of the chamber to within $\pm 0{\cdot}1^{\circ}$ and that the absolute angles were correct to within $\pm 0{\cdot}1^{\circ}$. These checks were made by measuring Rutherford scattering angular distributions on either side of zero (Mo 67).

2.4 Gas Target

The cross-sectional views of the gas cell are included in figures 2.1 and 2.2. A detailed description of the cell design was given by Ohlsen and Young (Oh 64, Yo 65). Some of the features of the cell are summarized below.

The cell has an inside diameter of 7·5 cm and an inside height of 2·5 cm. The frame of the cell together with the top and bottom plates were constructed from stainless steel. The bottom plate is attached on a brass support which in turn can be mounted on the bottom lid of the scattering chamber with an o-ring vacuum seal on the inside of the chamber. Gas filling leads of 0·15 cm internal diameter pass through the bottom plate and brass support and couple the cell to the external gas handling system.

The supporting pillars of the gas cell frame, at the entrance and exit apertures, define the range of angles of observation through the 1·25 cm window to be $12^{o}<\theta<168^{o}$; θ is the laboratory angle setting of a detector with respect to the incident beam direction. The entrance and exit apertures are 0·8 and 1·12 cm in diameter respectively.

Mylar foil aluminized on one side, of thickness $0{\cdot}38 \times 10^{-3}$ cm, was employed for the windows on both sides of the cell. The mylar was glued to the inner walls of the cell with an expoxy resin. Nickel foils of nominal thickness $0{\cdot}064 \times 10^{-3}$ cm were similarly attached to frames which were coupled to the exit and entrance apertures via o-ring seals. Both top and bottom plates made o-ring seals with the cell frame.

The experimental measurements were carried out with a ^{20}Ne gas pressure of 70 mm of Hg or less. A new gas cell could contain pressures in excess of 200 mm but the maximum allowable pressure decreased with use. The mylar foils were observed to become brittle in the regions of the exit and entrance apertures and with continued use of the cell finally ruptured in these regions. This deterioration is attributed to radiation damage and decomposition of the foil under the higher intensity radiation at these angles. Build up of carbon and oxygen indicated both in spectra and by the increasing gas pressure confirmed that the mylar $(C_{10}H_8O_4)_n$ was decomposing.

2.5 Gas Handling System

A flow diagram of the gas handling system used at station 2 is shown in figure 2.3. A similar system, used by Ohlsen and Young (Oh 64, Yo 65), was located at station 1.

Both systems employed Wallace-Tiernan aneroid manometers, model FA-145, which were calibrated against the liquid manometer described by Young. The 300 cm columns of the manometer contained dibutyl phthalate which has a low vapour pressure and a density of 1.0465 gm/ml at 20°C. The calibration curve for the two gauges is shown in figure 2.4. The scale of the manometers could be read to an accuracy of ±0.1 mm which together with the absolute calibration yielded an uncertainty in the pressure reading, in the range 20 to 70 mm, of ±0.35 mm.

In the absence of heating along the beam path, the gauge pressure will give the gas cell pressure accurately. Young (Yo 65) considered the effect of beam heating both experimentally and theoretically and showed that an error in the calculated yield proportional to the beam current could be introduced. Bray (Br 66) applied these considerations to 200×10^{-9} amps of 10 MeV $^{3}He^{++}$ through an identical gas cell containing ^{22}Ne at 70 mm and estimated a possible error in yield calculations of -1.5%. In the present experiment the beam was never in excess of 150×10^{-9} amps and generally was less than 100×10^{-9} amps. Thus the possible error in yield measurements arising from beam heating effects is estimated to be less than -1%.

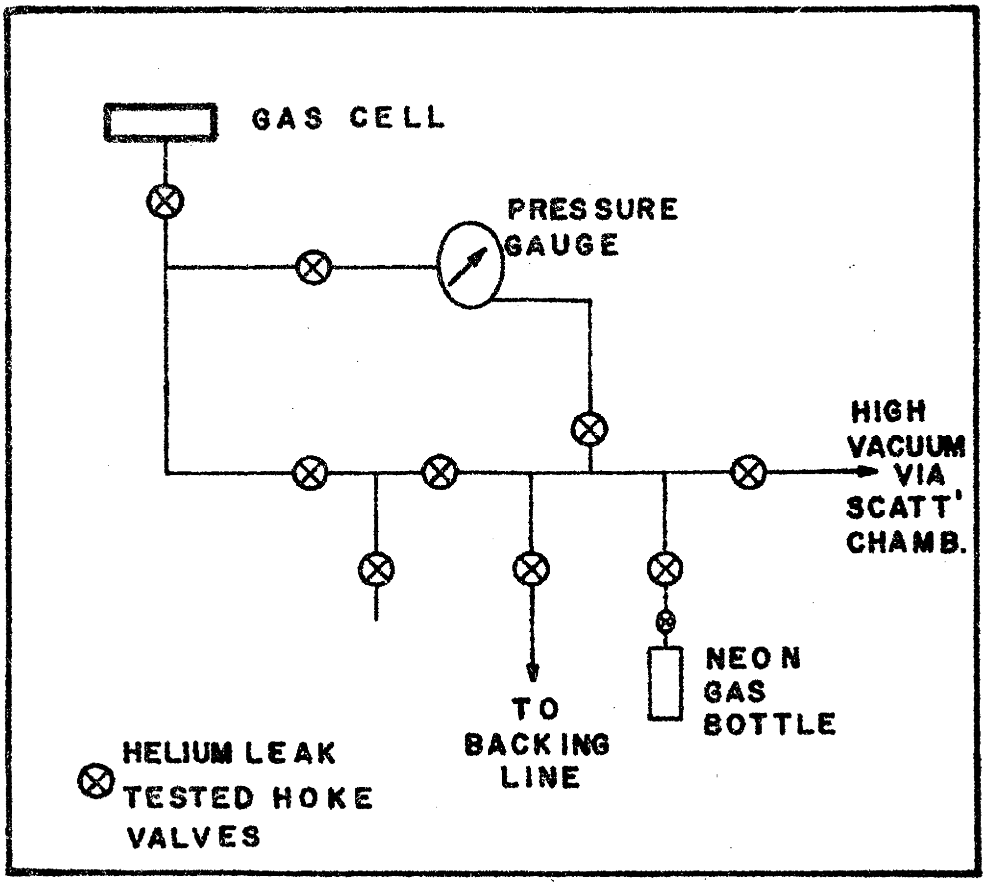

FIGURE 2.3 Gas Handling System

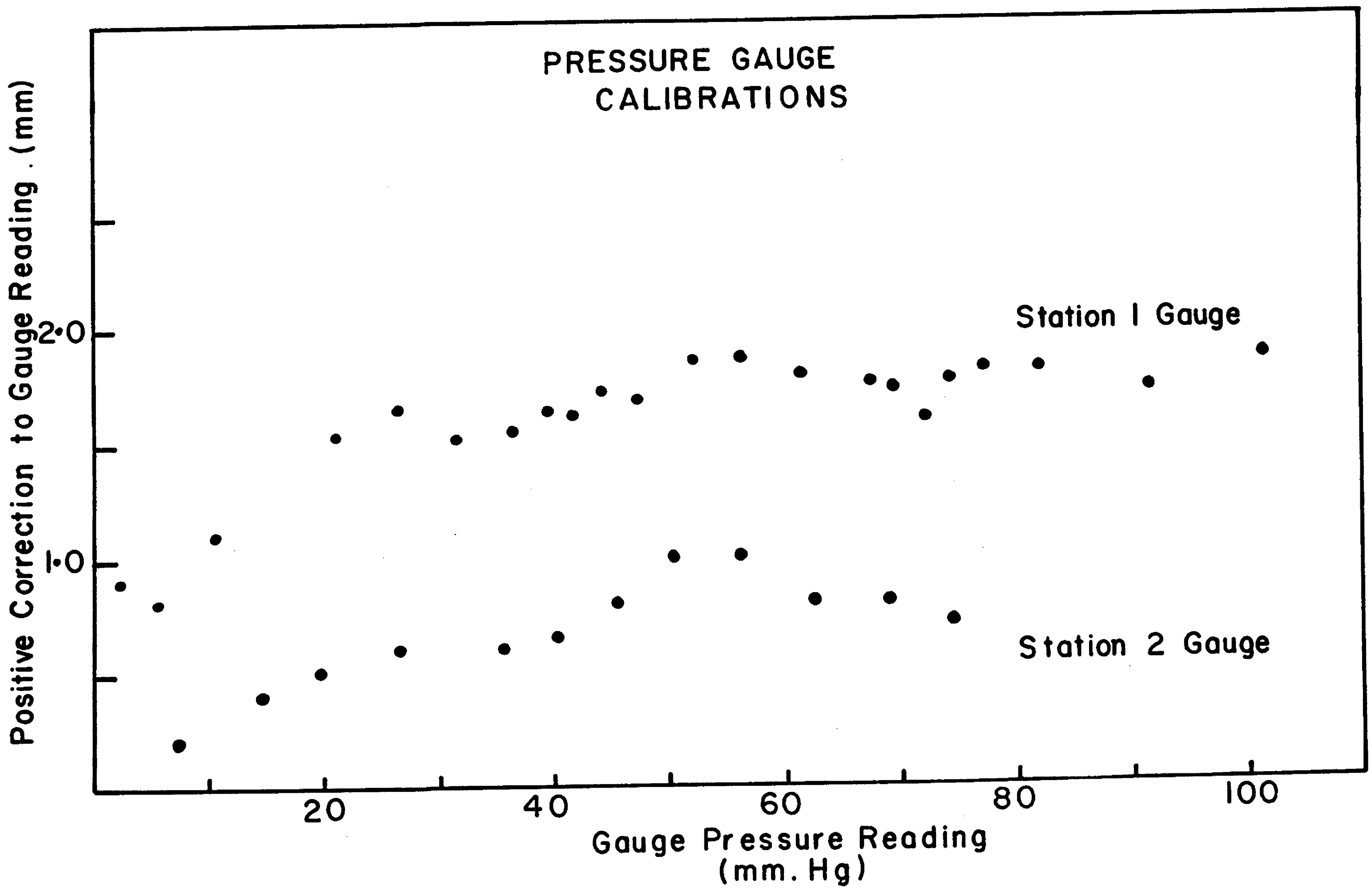

FIGURE 2.4 Calibration of Pressure Gauges

During the course of the measurements, the gas cell and gauge were coupled to permit regular monitoring of the gas cell pressure. An initial pressure typically of 70 mm could after 72 hours of bombardment increase by as much as 2 to 3 mm. As mentioned in section 2.4, this effect was almost certainly due to release of carbon and oxygen associated with the mylar decomposition. Spectra recorded during the course of such a 72 hour series of measurements showed a corresponding increase in the yield of groups scattered from oxygen and carbon. Groups scattered from nitrogen would have resulted from a leaking system; such groups could not be identified.

The temperature of the gas cell environment was monitored with a mercury thermometer. This thermometer was placed in contact with the bottom stainless steel plate of the gas cell. These temperature readings were considered to indicate the gas temperature to within $\pm 3^{\circ}C$. The error in the calculated yield introduced by such inaccuracy is less than 1%. For the yield calculations, the initial temperature and pressure were used to determine the target density.

The ^{20}Ne gas as supplied by Monsanto Research Corporation was of high isotopic and elemental purity ($\geq 99{\cdot}8\%$ ^{20}Ne).

The gas cell, scattering chamber and gas handling equipment were coupled into the high vacuum system for 24 hours prior to the commencement of a run on the accelerator. This seemed an appropriate precaution in view of the small bore high impedance tubing of the gas handling equipment.

2.6 Charge Collection

The Faraday cup immediately behind the scattering chamber employed both magnetic and electrostatic suppression. A calculation of the maximum divergence of the beam as defined by the collimating apertures and multiple scattering on traversing the cell indicated that the acceptance angle of the Faraday cup was more than adequate to collect the total incident charge.

The multiple scattering of the beam traversing the gas cell was estimated according to the formulation of Williams (Wi 39) which assumes the angular distribution of multiply scattered beam will be gaussian. More recent theories and experimental measurements indicate the inadequacy of this description particularly in the tail of the distribution (Ma 67). For the purposes of the present calculation, it seemed sufficient to use the simpler theory and consider the most extreme trajectory through the cell. The root mean square angle of multiple scattering for 12 MeV $^{4}He^{++}$ in each nickel foil was calculated to be $\approx 0{\cdot}009$ radians while that in the ^{20}Ne (at 70 mm) to be $\approx 0{\cdot}008$ radians. Such distributions of the beam would not cause significant loss of charge. The current integrator used was an Elcor model A309A. With calibration against a constant current source, the specifications cite an integration accuracy of better than 1%. Routine calibrations and checks during the measurements and by other workers in the laboratory indicated that the stability and accuracy of integration can be regarded as within 1%.

2.7 Detector Assembly

An array of four silicon surface barrier semiconductor diodes detected the scattered particles. The active volume of the gas target viewed by each detector was defined by a pair of rectangular collimating slits.

The counters, which were supplied by Ortec, were of 200 mm^2 surface area; the maximum depletion depth was 100 microns for three of them and 310 microns for the fourth which was used for forward angle measurements.

The triple counter array mounted on the rotatable top lid is illustrated in figure 2.1. The angular location of the three collimating systems defined three angles of observation of θ and $\theta \pm 20^\circ$ to within $\pm 0{\cdot}07^\circ$. The array could be located $2{\cdot}2485 \pm 0{\cdot}0005$ inches from the axis of rotation using dowel pins after initial positioning on a jig-borer. The fourth detector was located on the fixed bottom lid using a similarly positioned single block. A single counter assembly is illustrated in vertical cross-section in figure 2.1 The quadrature sum of :

(i) the uncertainty of $\pm 0{\cdot}1^{\circ}$ in the alignment of the scattering chamber (section 2.3); and

(ii) the uncertainty in angular location of the counter blocks of $\pm 0{\cdot}07^{\circ}$

defined an uncertainty of $\pm 0{\cdot}12^{\circ}$ in the angle of observation.

The collimating slits were constructed from four pieces of 1/16 inch precision flat steel screwed onto a frame of the same material. The rectangular aperture of each slit thus defined was inspected and measured under a microscope. The imperfections seen in these apertures were too slight to be of significance. The apertures were located in the counter blocks by precision cut slots and the accuracy of location of the apertures, and their dimensions, are considered in terms of the G factor in section 3.4.

2.8 Electronics

A block diagram of one of the several configurations of electronics employed is shown in figure 2.5. The preamplifiers and amplifiers were provided by Ortec. The model 103/203 valve series were used for the first half of the measurements and the modular transistorized 109/410 series for the later measurements. In both cases double delay line clipping of the pulses from each detector was usual.

Two 400 channel RIDL and two 512 channel RCL multichannel analyzers were available for use in the laboratory. Occasional unavailability of all these simultaneously necessitated the routing of the RIDL analyzers. In this way two 200 channel spectra were accumulated in each of the RIDLs. The procedure was quite satisfactory for the count rates observed; reflections between spectra were identified for some forward angle measurements of elastic scattering but they were too small to affect the accuracy of the measurements.

Various forms of this routing system were used for approximately 75% of the measurements; the block diagram 2.5 shows a typical mode of operation. The four routing signals were derived from COSMIC single channel discriminators and mixing of each pair of spectra was achieved via a simple diode circuit. The outputs of each discriminator were scaled to provide a check of the system.

Dead time corrections were recorded with each spectra. Scalers counting 100 counts/sec pulse trains gated by the analyzer 'busy' outputs provided this information.

2.9 Gas Target Thickness

The active volume of the gas target varies as a function of the angle of observation. The target thickness, as defined by the slit geometry common to all detectors and

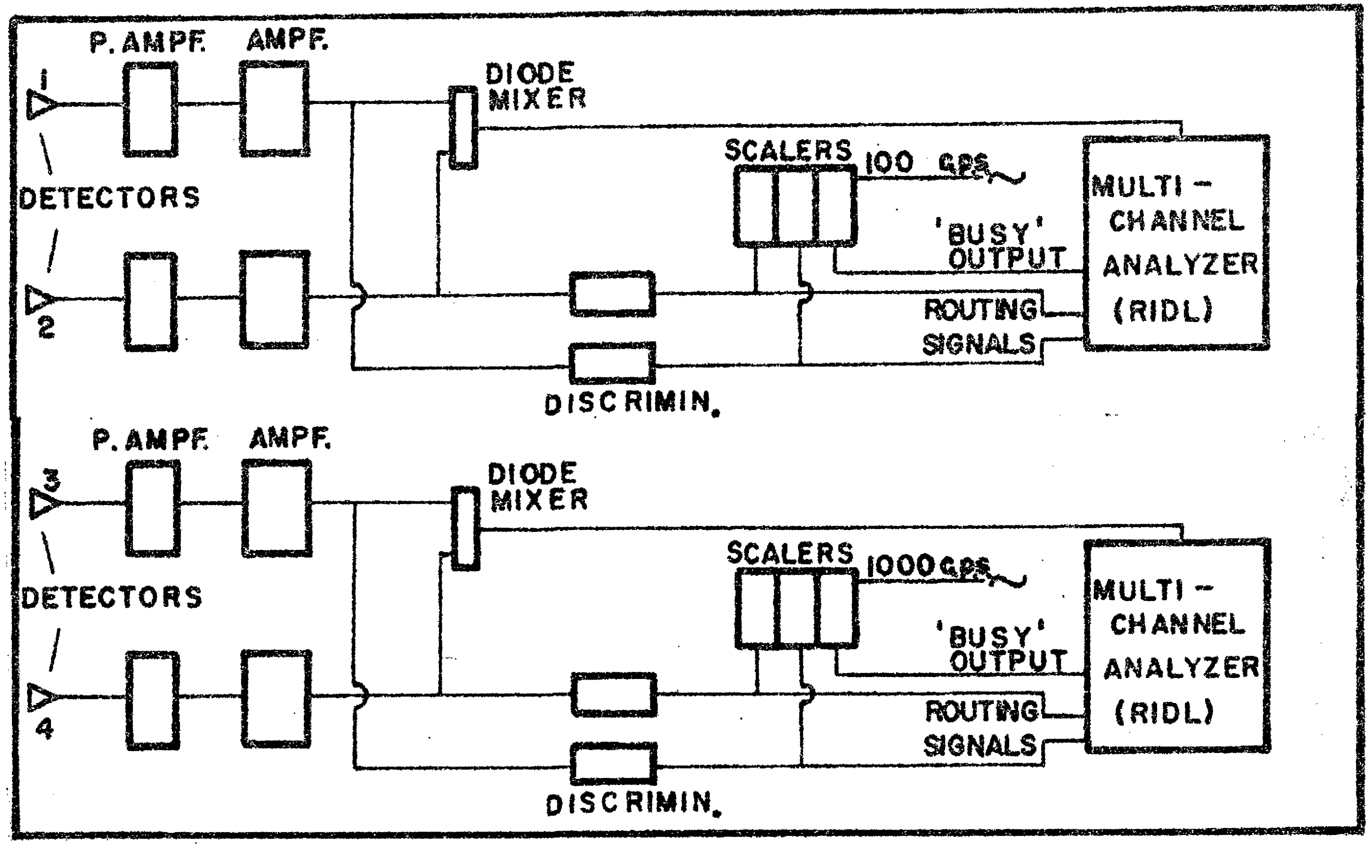

FIGURE 2.5 Block diagram of electronics configuration.

illustrated in figure 3.3, is given in kev in table 2.1 as a function of angle and gas cell pressure for an incident $^4He^{++}$ beam of 12·0 MeV. These values were obtained from a computer code incorporating the expressions for z_1 and z_2 of figure 3.3 with the energy loss subroutine described in appendix 1.

Table 2.1

Gas Target Pressure	Target Thickness in kev at Angle				
	20°	30°	50°	70°	90°
20 mm	13·2	9·0	5·8	4·8	4·5
40 mm	26·4	17·9	11·7	9·5	8·9
70 mm	46·4	31·5	20·5	16·7	15·7

2.10 Energy Definition and Detection Resolution

The incident $^4He^{++}$ beam on passing through the nickel entrance window and target gas is degraded in energy and has its beam energy profile broadened.

Calculations of the mean energy at the centre of the gas cell were incorporated in the kinematics code considered in section 3.1 and the uncertainties arising in the calculations are typified in table 2.2. These values apply to an incident beam of 12·0 MeV $^4He^{++}$ and a gas cell pressure of 70 mm.

Table 2.2

		Uncertainty	
Mean Incident Energy	12·0 MeV	±0·006 MeV	(a)
Mean Energy Loss in Nickel	0·150	±0·030	(b)
Mean Energy Loss in Neon	0·137	±0·007	(c)
Mean Energy at Centre of Gas Cell	11·713	±0·032 MeV	

(a) See section 2.2.

(b) and (c) arise from thickness uncertainties and the stated accuracy of the energy loss tables (Wi 66). The nickel foil specifications quote a manufacturing tolerance of ±20% in thickness.

The beam energy profile broadening was considered in terms of the Vavilov distribution as discussed by Seltzer et al (Se 64). The incident beam energy profile was considered gaussian and interpolation from the tables of Seltzer et al yielded Vavilov distributions which indicated that the gaussian profile was retained at the centre of the gas cell although broadened and with a small tail on the low energy side.

The broadening of the incident beam energy profile, associated with the energy loss discussed above, for the case of the 12 MeV $^4He^{++}$ incident beam and a gas pressure of 70 mm is listed in table 2.3.

Table 2.3

Beam	Half-width at Half-intensity of Gaussian Profile
Incident	5 kev
Through Nickel Foil	16 kev
Through Nickel and Neon to gas cell centre	22 kev

In view of the small area of the beam spot and the manufacturing porosity specifications for the grade of nickel foil used, the thickness of foil has been assumed constant over the beam spot area and contributions to beam energy broadening from non-uniformity of the foil have been regarded as negligible.

The energy resolution of the measurements, i.e. the finite range of energies contributing to a particular scattering measurement, is estimated by compounding both the broadening and the target thickness discussed in section 2.9. The algebraic sum of the target thickness for an observation angle of 30° (or 150°) and the above-estimated beam energy profile width are listed in table 2.4 for three gas cell pressures appropriate to measurements at 12 MeV.

Table 2.4

Gas Cell Pressure	Energy Resolution of Measurement
20 mm	±19 kev
40 mm	±26 kev
70 mm	±38 kev

The energy resolution of detection was further determined by :

(i) finite range of detection angle - see figure 3.3;

(ii) straggling in energy of the scattered particles in passing through the neon and mylar; and

(iii) electronic resolution.

Table 2.5 exemplifies the contributions to the energy definition of groups observed in a typical 30° spectra such as recorded for a 12 MeV incident beam and 70 mm gas cell pressure.

Table 2.5

Energy Resolution of Measurement	± 38 kev
Finite Range of Angle of Detection	± 80 kev
Straggling in Neon and Mylar	± 30 kev
Electronic Resolution	± 50 kev
R.M.S. Detection Resolution	±110 kev

The spectra shown in figure 3.1 are compatible with this evaluation of the resolution; the two groups corresponding to the excitation of the fourth and fifth excited states, kinematically separated by ≈70 kev, are unresolved.

From the discussion hitherto the following summary can be drawn :

(a) The absolute scale of energies at the centre of the gas cell was considered accurate to within ±30 kev.

(b) The only significant uncertainty in the relative scale of energies at the centre of the gas cell for measurements over a limited energy range of ≈1 MeV using the same nickel entrance foil was considered due to the uncertainty of ±6 kev in the incident beam energy definition.

(c) The energy resolution of measurement was considered to be of the order of ±35 kev at 70 mm gas pressure and ±25 kev at 40 mm gas pressure.

(d) The overall detection resolution was of the order of ±110 kev.

2.11 Data Accumulation

With the exception of the most forward angle measurements, it was usual to take spectra at each angle corresponding to an incident charge of from 30 to 100 x 10^{-6} coulombs. This was found to yield adequate statistics although the low yield of the groups corresponding to the 2^- state of ^{20}Ne occasionally necessitated extended counting.

Reduction in beam intensity to several millimicroamps during the most forward angle measurements ensured counting losses in the multichannel analyzers of $\lesssim 3\%$. Counting losses for the majority of the measured spectra were typically $\lesssim 1\%$ with the full beam intensity.

The depletion depths of the counters were varied to be comparable with the range of the most energetic alpha group being detected but bias voltages were sufficient to preserve linearity of the spectra and to ensure against line shape distortion. It was important in using the nominal 310 micron counter at backward angles to reduce the depletion depth in order to avoid a background continuum, attributed to partially stopped protons from the ^{20}Ne (α,p) ^{23}Na reaction or deutrons from the ^{20}Ne (α,d) ^{22}Na reaction.

The accumulated spectra were recorded on printed tape as well as on punched cards or punched paper tape.

CHAPTER 3
Data Analysis

Subsequent to identification of the particle groups in the recorded spectra the counts in the peaks of interest were summed and the yields converted to absolute cross sections, the accuracy of which was considered in terms of relative and absolute errors.

3.1 Scattering Kinematics

A table of Q values of competing reactions for alpha particles incident on ^{20}Ne as well as on the major gas contaminants ^{16}O and ^{12}C is shown in table 3.1.

Table 3.1

Target	Reaction Products	Q Value (MeV)*
^{20}Ne	^{23}Na + p	- 2·38
	^{22}Na + d	-12·57
	^{21}Na + t	-17·36
	^{21}Ne + ^{3}He	-13·82
^{16}O	^{19}F + p	- 8·11
	^{18}F + d	-16·33
	^{17}F + t	-19·21
	^{17}O + ^{3}He	-16·44
^{12}C	^{15}N + p	- 4·96
	^{14}N + d	-13·57
	^{13}N + t	-17·87
	^{13}C + ^{3}He	-15·63

* Taken from Nuclear Data Tables of Everling et al (Ev 61)

The (α,^{3}He), (α,t) and (α,d) reactions all have relatively high negative Q values and the possible particle groups from these reactions are confined to the low energy region of the spectra. Similarly, protons from the (α,p) reactions are restricted to the same region of the spectra since only a small fraction of their energy is deposited in the thin depletion detectors.

Characteristic of the recorded spectra are those shown in figure 3.1 where the elastic scattering and inelastic scattering from the first five excited states of ^{20}Ne are seen. A study of groups in the lower portion of the spectra corresponding to excitation of ^{20}Ne in excess of 6 MeV was not possible with the energy resolution of the detection system used. The presence of groups elastically scattered from ^{16}O and ^{12}C is evident in the spectrum at 85^{o}. Rigorous identification of all alpha groups was based on kinematic calculations of position in the spectra as a function of angle. In view of the energy loss of the alpha particles, both incident and scattered, on passing through the windows and gas, a relativistic kinematics code (Ha 66) was modified to include evaluation of the losses (see appendix 1). Such kinematic calculations were particularly desirable in identifying and locating the contaminant groups precisely. Assumption of linearity of the spectra was compatible with the consistency of calibration obtained between all alpha groups.

3.2 Data Reduction

The summation of counts in spectral peaks of interest was performed on a desk calculator. Background, if significant, was evaluated together with an estimate of the possible error in the evaluation. The groups corresponding to the $(3^-,1^-)$ doublet were not resolved and thus composite yields were extracted.

The major task in obtaining the yields was in correcting for the ^{16}O and ^{12}C contaminants. An illustration of the characteristic energy variation of observed groups as a function of laboratory angle is shown in figure 3.2; this kinematic plot corresponds to an incident $^{4}He^{++}$ energy of 14·50 MeV, an energy for which contaminant corrections, as indicated in table 3.2, were made.

Table 3.2

^{20}Ne Group	Angles of Correction for Carbon Contaminant	Angles of Correction for Oxygen Contaminant
0^+	$\theta \leqslant 25^\circ$	$\theta \leqslant 35^\circ$
2^+	$55^\circ \leqslant \theta \leqslant 65^\circ$	$\theta \geqslant 110^\circ$
4^+	$\theta \geqslant 135^\circ$	
2^-	$25^\circ \leqslant \theta \leqslant 35^\circ$	
$(3^-,1^-)$	$45^\circ \leqslant \theta \leqslant 65^\circ$	

The corrections were typically $\leqslant 5\%$ of the yield, although the corrections for the 2^- yields were as much as 20%.

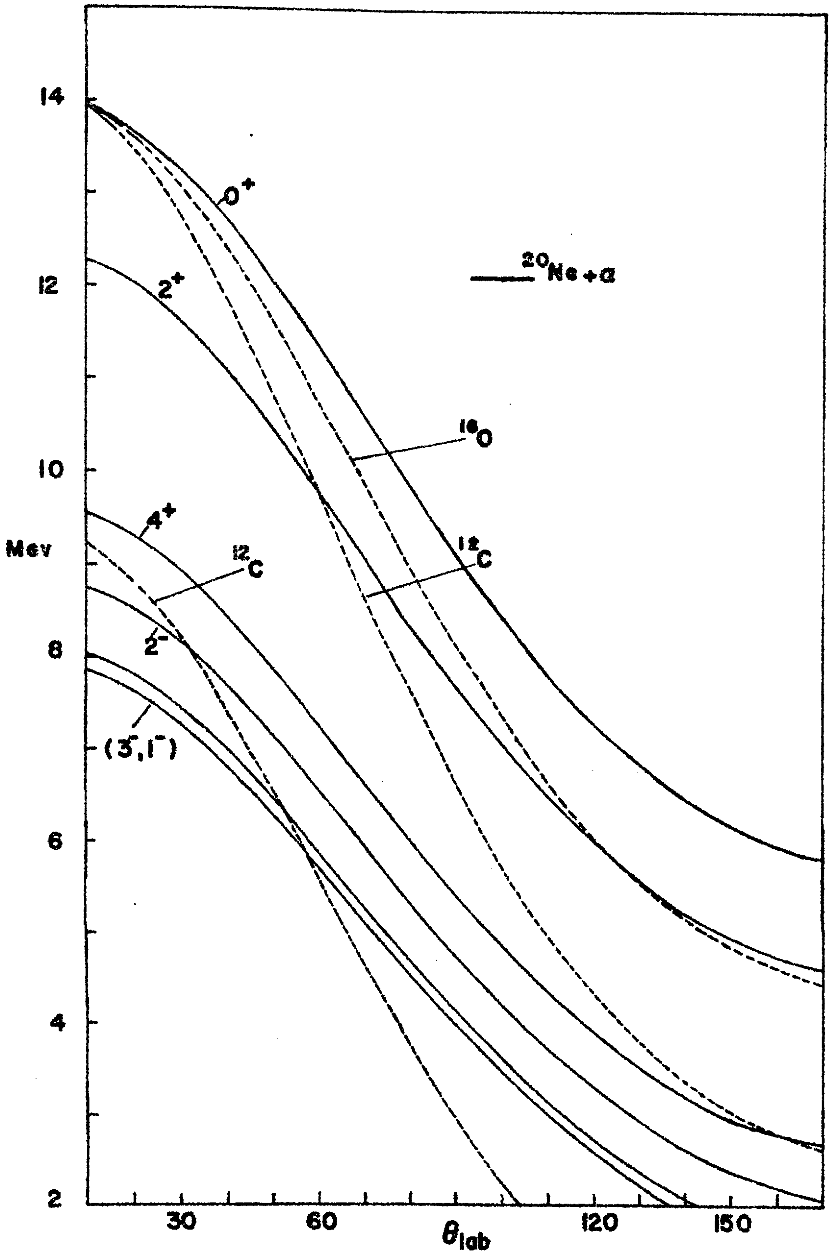

FIGURE 3.2 Energy variation of observed groups as a function of scattering angle at an incident energy of 14·50 MeV.

The $^{16}O(\alpha,\alpha_0)^{16}O$ measurements of Mehta et al (Me 67) and the $^{12}C(\alpha,\alpha_0)^{12}C$ and $^{12}C(\alpha,\alpha_1)^{12}C$ measurements of Mitchell et al (Mi 64) were used to establish the contaminant corrections. These data were available in graphical form only and as a result the uncertainties in some corrections were large. Other inaccuracies in these corrections arose because of the extrapolations between energies and angles necessary to obtain a reasonable estimate of the cross-section. The amount of ^{16}O and ^{12}C in the gas cell at any time was estimated by considering spectra, usually from the monitor, in regions where the available cross sections were considered reliable.

3.3 Absolute Cross Sections

The yields were converted to absolute cross sections according to the relation for gas targets of Silverstein (Si 59).

$$\sigma(\theta) = \frac{Y \sin\theta}{n\ N\ G} \qquad (3\text{-}1)$$

where $\sigma(\theta)$ is the differential cross section at laboratory angle θ,

θ is the laboratory angle of detection defined by the central axis of the detection collimating system,

n is the total number of incident particles,

N is the number of target nuclei per unit volume,

Y is the yield of scattered particles at angle θ, and

G is the factor describing target thickness, angle of acceptance of detection system and finite geometry effects (see section 3.4).

For doubly charged ions incident on a monatomic gas at pressure p and temperature T, this expression can be re-written in the form :

$$\sigma(\theta) = \frac{Y \sin\theta}{G\ X} \times \frac{(T+273.2)}{p} \times 3.320 \times 10^{-5} \qquad (3\text{-}2)$$

where $\sigma(\theta)$ is given in mb/sr,
p is given in mm of Hg,
T is given in degrees centigrade,
X is the incident charge in microcoulombs, and
G has the dimensions of cm.

Computer codes were developed to evaluate expression (3-2) for the angular distribution data and the excitation function data. Incorporated in the codes were kinematic (Ha 66) and energy loss subroutines to enable conversion to cross section in the centre of mass co-ordinate system. Repeated data points were averaged and errors as discussed in section 3.5 were evaluated. All data were corrected for dead time losses in the multichannel analyzers. The resultant cross sections were available together with error estimates in numerical, punched and graphical format.

The monitor counter yields taken during the angular distribution measurements and corresponding to excitation of the ground and first two excited states were obtained in the course of this data reduction. Where statistics were adequate, long term stability of within 3% was obtained for these yields. In view of the reproducibility of the angular distribution data and the stability of the monitor yields, no attempt was made to normalize to these monitor yields.

For the angular distribution data, an option of finite geometry corrections was available (see section 3.4).

3.4 G Factor

Figure 3.3 shows in detail the geometry of the detection systems used for all four counters. An inset tabulates the angular resolution and active gas length as a function of θ for such a geometry. The quantity G of equation (3-1) is given by Silverstein as

$$G = G_{00}\left[1 + \Delta_0 + \Delta_1 \frac{\sigma^1}{\sigma} + \Delta_2 \frac{\sigma^2}{\sigma} + \Delta_3 \frac{\sigma^3}{\sigma} + \quad \ldots\right] \qquad (3\text{-}3)$$

where $G_{00} = \dfrac{4\, b_1\, b_2\, \ell}{R_0\, h}$

and where b_1, b_2, ℓ, R_0 and h are as in figure 3.3,

- σ is the differential cross section at θ,
- σ^n is the n^{th} derivative of the differential cross section with respect to θ at angle θ,
- Δ_n are terms indicating the "poorness" (Si 59) or finite nature of the geometry and are given explicitly up to $n = 4$,
- Δ_0, Δ_1 and Δ_3 are functions of the angle of observation and the dimensions and location of the collimating apertures, and

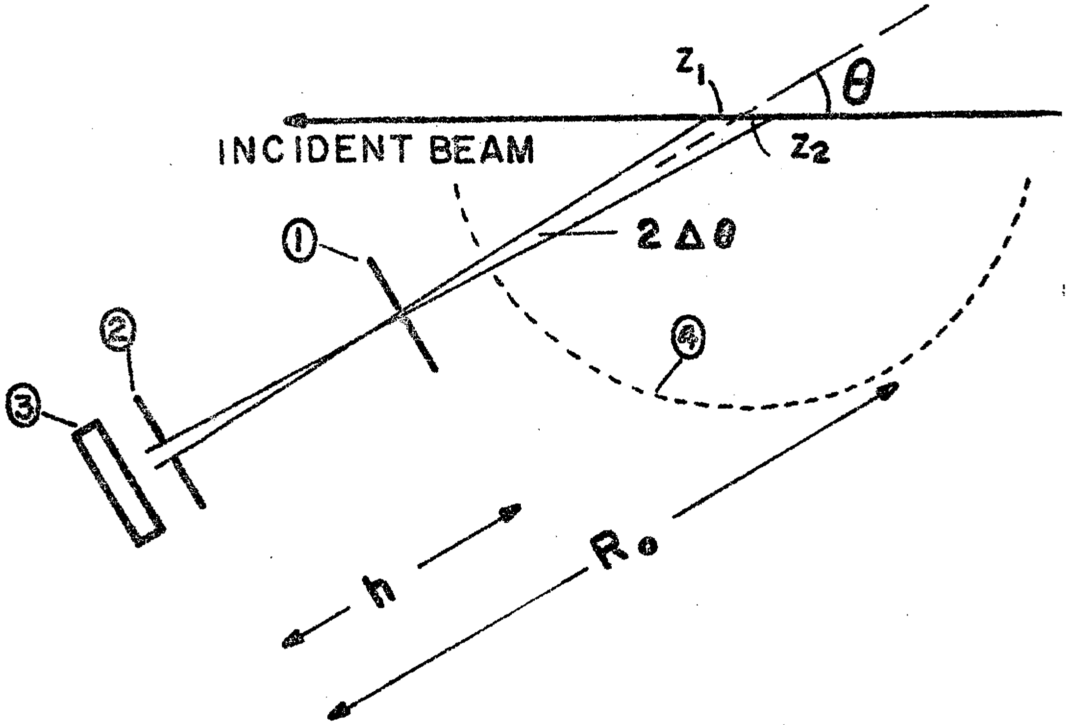

1 Rectangular collimating apertures of half width b_1 and height ℓ.
2 Rectangular collimating aperture of half width b_2.
3 Surface barrier detector.
4 Mylar window.

b_1 = 0·05 cm; b_2 = 0·1 cm; ℓ = 1·2 cm;
R_0 = 10·3 cm; h = 4·13 cm

θ	Z_1 (cm)	Z_2 (cm)	$\Delta\theta$
10°	1·30	1·97	2·07
30°	0·51	0·58	2·07
90°	0·27	0·27	2·07

FIGURE 3.3 Detection Geometry defined by collimating apertures

Δ_2 and Δ_4 are functions only of the aperture dimensions and their separation.

R_0 and h, obtained from precision jig-borer measurements, and b_1, b_2 and ℓ obtained from microscope measurements on a calibrated stage, determined the value of G_{00} to an accuracy of ±1·1%.

A subroutine was incorporated in the data reduction code to evaluate finite geometry corrections up to second order for the angular distribution data. These corrections were applied to the cross sections expressed in the laboratory system of co-ordinates.

To obtain the quantity $\sigma^1(\theta)$ and $\sigma^2(\theta)$ of equation (3-3), a quadratic was fitted through successive groups of three data points. The first and second derivatives of the mid-data point of the three were thus estimated. An estimate of the higher order derivatives was made by application of this quadratic fitting to the first derivatives and then successive application to the subsequently derived derivatives. The estimates of the third and fourth order terms indicated that these higher order corrections were insignificant. The most significant corrections were of second order occurring at minima in the angular distributions; as the corrections described above are necessarily derived from uncorrected data the procedure outlined was repeated to obtain convergence. One iteration gave convergence to<<1% on the majority of corrections although convergence for large corrections required several iterations. Four iterations were thus applied as a standard procedure. The 13·92 MeV elastic scattering angular distribution in the laboratory system of co-ordinates and the ratio $(G - G_{00})/G$ for this data are illustrated in figure 3.4. The correction at the 45° minimum is the largest to any of the data points measured. Typically this ratio was <0·1 for most minima of the angular distributions.

The largest corrections were due to the finite definition of geometry provided by the dimensions and separation of the collimating apertures. This is in contrast to corrections which in addition depend on the aperture locations relative to the target. In retrospect it is considered that an equivalent geometry less subject to corrections would require smaller apertures similarly separated but closer to the gas cell.

3.5 Error Analysis

The accuracy of cross section evaluation according to equation (3-2) is subject to uncertainties in Y, G, X, p, T and θ.

The uncertainty in Y is taken to be the quadrature sum of :

(i) the standard deviation of total counts in the summed peak (assuming Poisson statistics); and

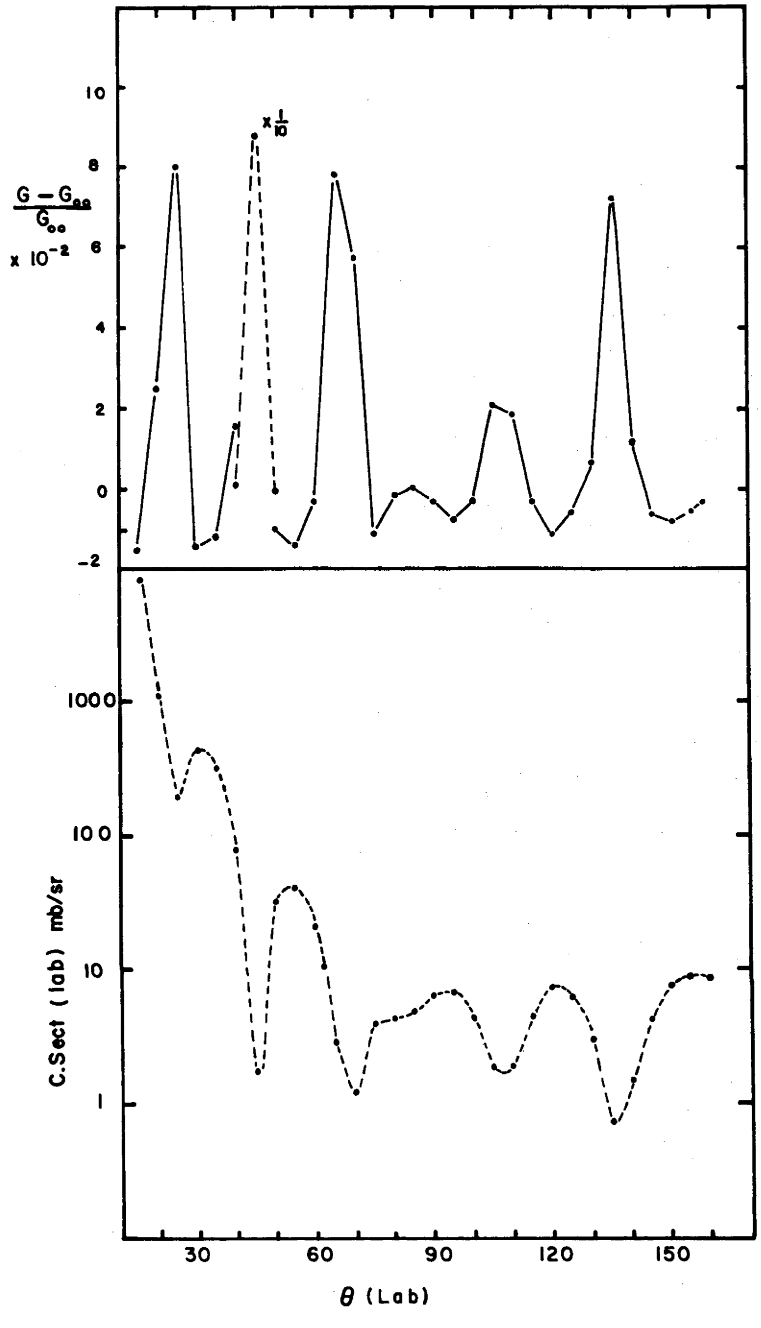

FIGURE 3.4 Finite geometry corrections to 13·92 MeV elastic scattering

(ii) the estimated uncertainty in the background subtraction.

In considering repeat measurements a weighted mean of the data points was obtained. The weight assigned to each datum point was equal to the square of the inverse of the uncertainty in Y. A weighted mean error was also obtained. The actual quantities averaged were cross sections.

In a few cases, the weighted mean deviation of the averaged data points from the mean was greater than the weighted mean error. This was interpreted as a systematic error as could arise between two different accelerator runs and the error assigned in these cases was the quadrature sum of the mean deviation and mean error. The two sets of measurements of the 14·30 MeV angular distributions showed such non-statistical deviations; this was attributed to a slight energy discrepancy between the runs (see section 4.2).

The accuracy of the finite geometry corrections is difficult to establish. However, confidence is placed in the evaluation as convergence of almost all corrections to within 1% of their value was obtained with one iteration (see section 3.4). A nominal error of ±50%, in the magnitude of the corrections, introduced an error in cross section of $\leq\pm4\%$ for most data points. The largest uncertainty of the finite geometry corrections was associated with the 45° data point of figure 3.4 where the 50%

correction uncertainty lead to an uncertainty in the absolute cross section of ±20%.

The finite dimensions of the incident beam path and the possible divergence of the beam (section 2.2) contribute to the finite geometry effects. More general expressions for the coefficients of equation (3-3) include dependence on the finite diameter of the beam path. Inclusion of a beam path diameter of 0·15 cm produces a variation of $\lesssim$0·1% in the cross section calculations. These generalized expressions for the coefficients assume that the active volume of gas is a cylinder parallel to the central beam axis. With this assumption, the divergence of the beam can be considered as effectively contributing to the angular resolution of detection. The most extreme trajectories of ±0·25° divergence from the central axis would correspond to increasing the angular resolution of detection by ≈10%. In view of the ±50% error assigned to the finite geometry corrections it is considered this additional angle averaging effect would not contribute significantly to the accuracy of already assigned corrections or to their associated errors.

The relative uncertainties in the angular distribution cross section data have been obtained from the quadrature sum of :

(i) the uncertainty arising from the nominal ±50% error assigned to the finite geometry correction; and

(ii) the statistical and averaging errors.

The limits of accuracy in determining the absolute cross section are, in addition, fixed by uncertainties in the quantities G_{00} (equation (3-3)), X, p, T and θ (equation (3-2)). From the discussion of these quantities in sections 3.4, 2.6, 2.5 and 2.7, the summary in table 3.3 of contributions to absolute cross section uncertainties can be drawn.

Table 3.3

Source of Uncertainty	Contribution to Absolute Cross Section Uncertainty
G_{00}	$\pm$ 1·1%
X	$\pm$ 1 %
p	$\pm$ 0·5%
T	$\pm$ 1 %
θ	$\leqslant\pm$ 2 % (a)
R.M.S.	$\leqslant\pm$ 2·8%

(a) The contribution of the $\pm 0{\cdot}12^{\circ}$ uncertainty in θ is significant for measurements dominated by Rutherford scattering and for measurements such as the 40° data point of figure 3.4.

An estimate of the overall accuracy of the absolute cross section data of the angular distributions is obtainable then from the quadrature sum of :

(i) the relative uncertainties; and

(ii) an absolute error of the order of $\pm 3\%$.

As it was not possible to correct the excitation function data for finite geometry effects and as the absolute cross sections were not of importance for analysis, the errors considered for this data indicate the relative accuracy of one point to the next. In regions where finite geometry corrections could be expected to be small the absolute magnitude determinations are considered to be of the same accuracy as the angular distribution data.

The measured cross sections for the angular distributions are tabulated in appendix IV together with the associated relative errors. The relative errors are included since they were used in the theoretical analysis. The requirement of balanced weighting of the data points (discussed in section 5.3 in terms of the optical model fitting procedures) was satisfied by assigning a 4% error to those relative errors less than 4%, while retaining those in excess of 4%; it is these modified errors which are tabulated.

The excitation function data are tabulated in appendices II and III together with associated statistical and averaging errors.

CHAPTER 4
Experimental Results

In this chapter the present measurements of excitation functions and angular distributions of elastic and inelastic alpha scattering from ^{20}Ne are presented together with a qualitative discussion of the results.

4.1 Excitation Functions

The initial measurements were taken to establish the energy dependence of the cross sections for both elastic and inelastic scattering. The pronounced energy dependence for incident energies of <20 MeV characterizing alpha scattering (Ca 64 and So 66) on light mass nuclei motivated the excitation function measurements.

Excitation curves were measured in ≈100 kev steps in the bombarding energy range of 11·71 to 14·93 MeV at laboratory angles of 40°, 80° and 150°. Remeasurements at the angles of 40° and 80° with additional measurements at 60° were made in the energy range 13·23 to 15·23 MeV, also in ≈100 kev steps. The remeasured data were in good agreement with the original measurements but were not used to obtain an average measurement as there were small systematic energy differences apparent in the two energy scales. The most significant effect was seen at 14·5 MeV in the 80° excitation curve of elastic scattering where an 8% variation in cross section measurement occurred. As all the above measurements were recorded using object and image slit gaps of 7·5 and 2·5 mm respectively (see section 2.2), it was considered that the optimization of beam during the course of the measurements produced variations in trajectory through the 90° analyzing magnet and gave rise to energy shifts of within 15 to 20 kev about the nominal beam energy. The data presented for 40° and 80° comprise the initial measurements plus three higher energy data points from the second set of measurements. Table 4.1 summarizes the excitation functions measured in ≈100 kev steps. The measurements were taken with the gas cell pressure at ≈70 mm and an energy resolution of approximately ±35 kev (see section 2.10).

Table 4.1

Laboratory Angle of Detection	Scattering State of ^{20}Ne	Laboratory Energy at Centre of Gas Cell (MeV)
40°	0^+	11·71 - 15·23
	2^+	11·71 - 15·23
	4^+	11·71 - 15·23
	2^-	13·43 - 15·23
	$(3^-,1^-)$	12·32 - 15·23
60°	0^+	13·23 - 15·23
	4^+	13·23 - 15·23
	2^-	13·53 - 15·23
80°	0^+	11·71 - 15·23
	2^+	11·71 - 15·23
	4^+	11·71 - 15·23
	2^-	11·91 - 14·02
	$(3^-,1^-)$	12·62 - 14·93
150°	0^+	11·71 - 14·93

The cross section measurements described in table 4.1 are tabulated in appendix II and plotted in figures 4.1(a), (b), (c) and (d). The cross sections are tabulated and plotted with relative errors and are given in the centre of mass co-ordinate system for elastic scattering and in the laboratory co-ordinate system for inelastic scattering; the energy scale is subject to relative uncertainties of ≤ 20 kev as was discussed above.

The lower range of incident energies of the excitation functions corresponds to excitation energies in the compound system ^{24}Mg of ≈ 20 MeV, energies at which there are several well defined states described as quasi-molecular (Al 63). The pronounced peak in the elastic scattering excitation function at 150° (Lab) for an incident energy of 12·32 MeV suggested that these states may be populated in the ^{20}Ne+α interaction; the energy of 12·32 MeV corresponds to an excitation energy in ^{24}Mg of within 10 kev of the lowest of the quasi-molecular states at 19·58 MeV excitation. Although such correspondence could be regarded as fortuitous in view of the uncertainties in the absolute energy scale of the order of ± 30 kev and in the relative energy scale of within ± 20 kev, the possibility of some significance in the correspondence motivated more detailed measurements.

Consequently, additional excitation functions were measured in the incident energy range 12·045 to 13·457 MeV

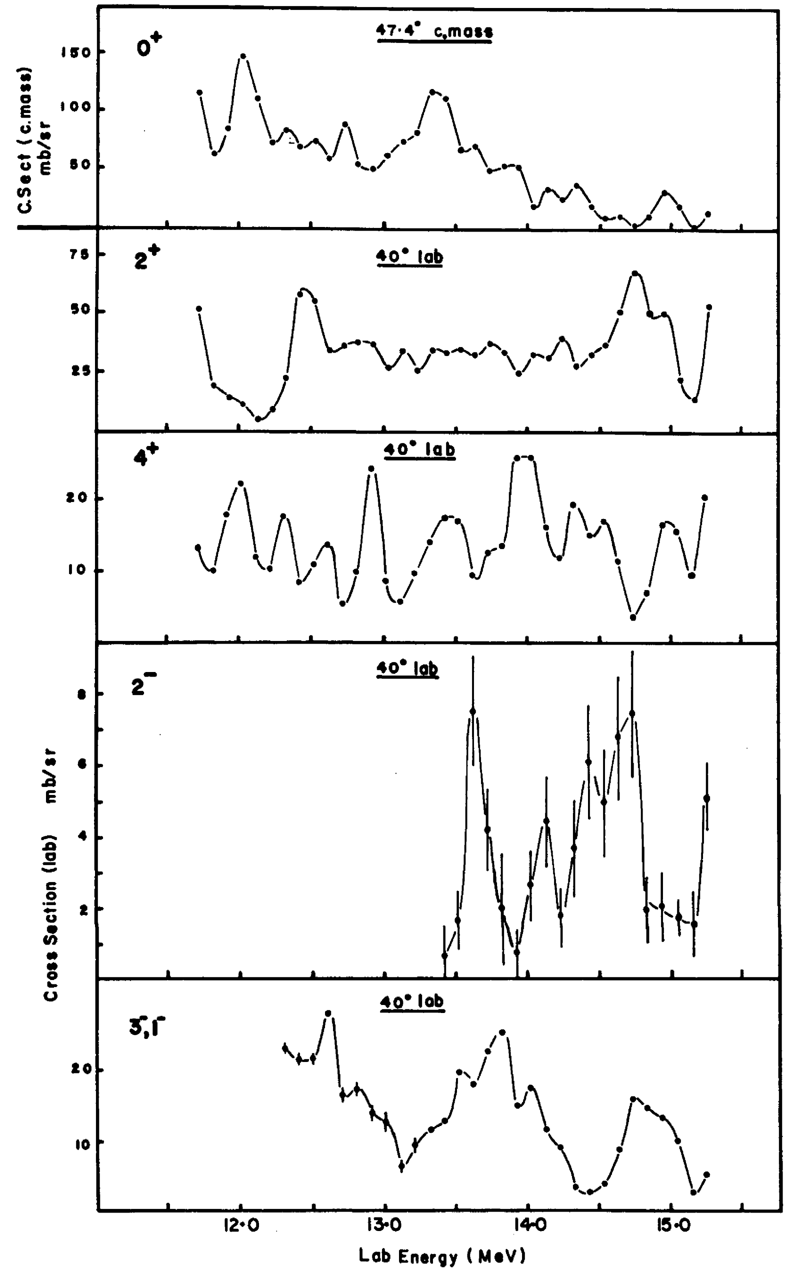

FIGURE 4.1(a) Excitation functions of alpha scattering on ^{20}Ne measured in ≈100 kev intervals at 40^{0} (Lab); the solid lines through the data points have been drawn by eye and significant error bars are shown

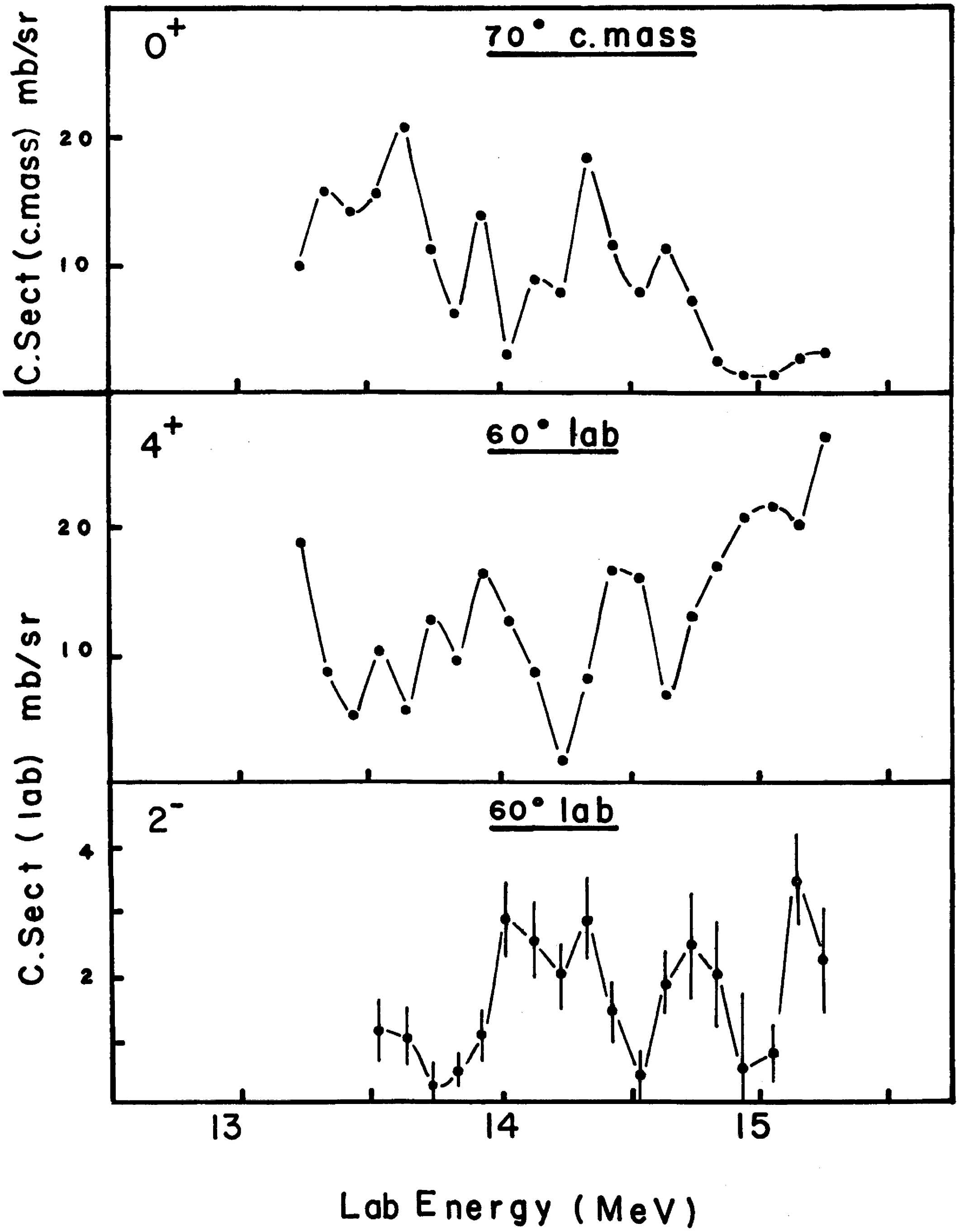

FIGURE 4.1(b) Excitation functions of alpha scattering on ^{20}Ne measured in ≈100 kev intervals at 60° (Lab); the solid lines through the data points have been drawn by eye and significant error bars are shown

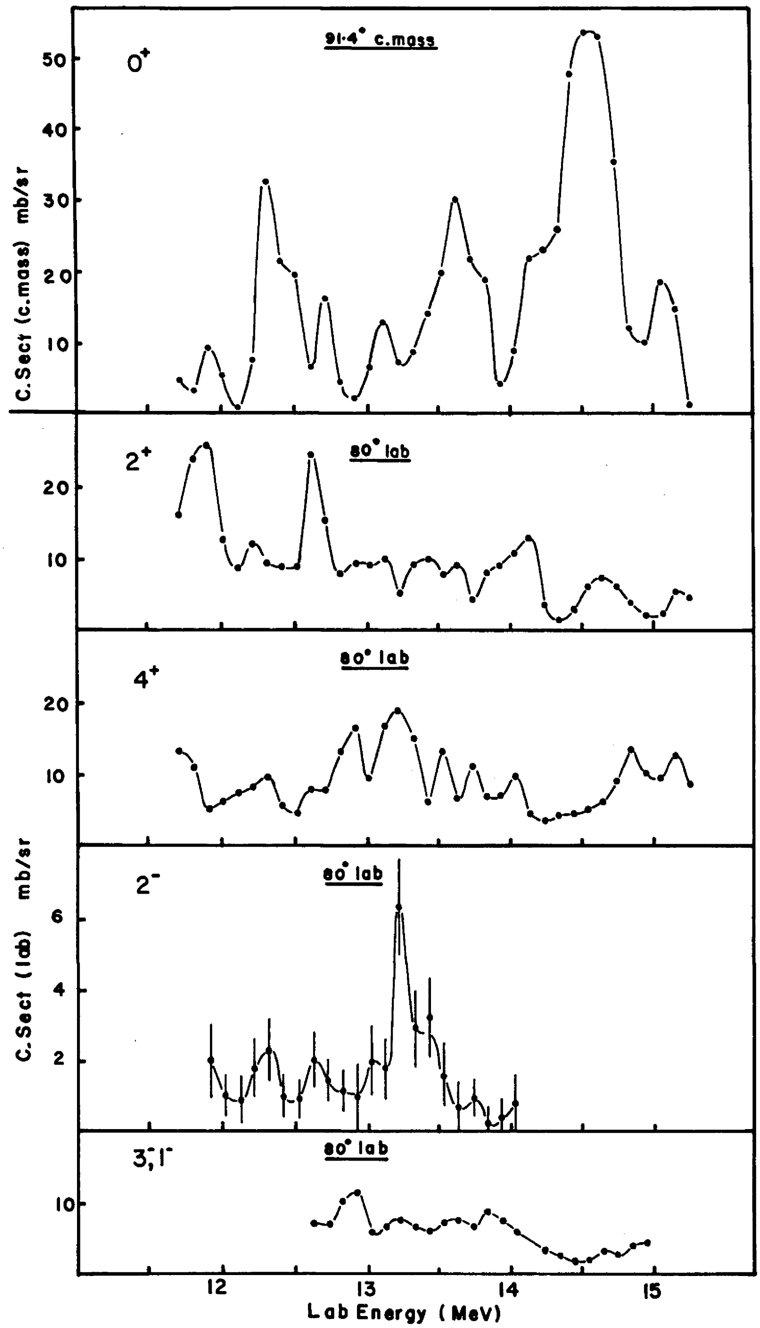

FIGURE 4.1(c) Excitation functions of alpha scattering on ^{20}Ne measured in ≈100 kev intervals at 80^{o} (Lab); the solid lines through the data points have been drawn by eye and significant error bars are shown

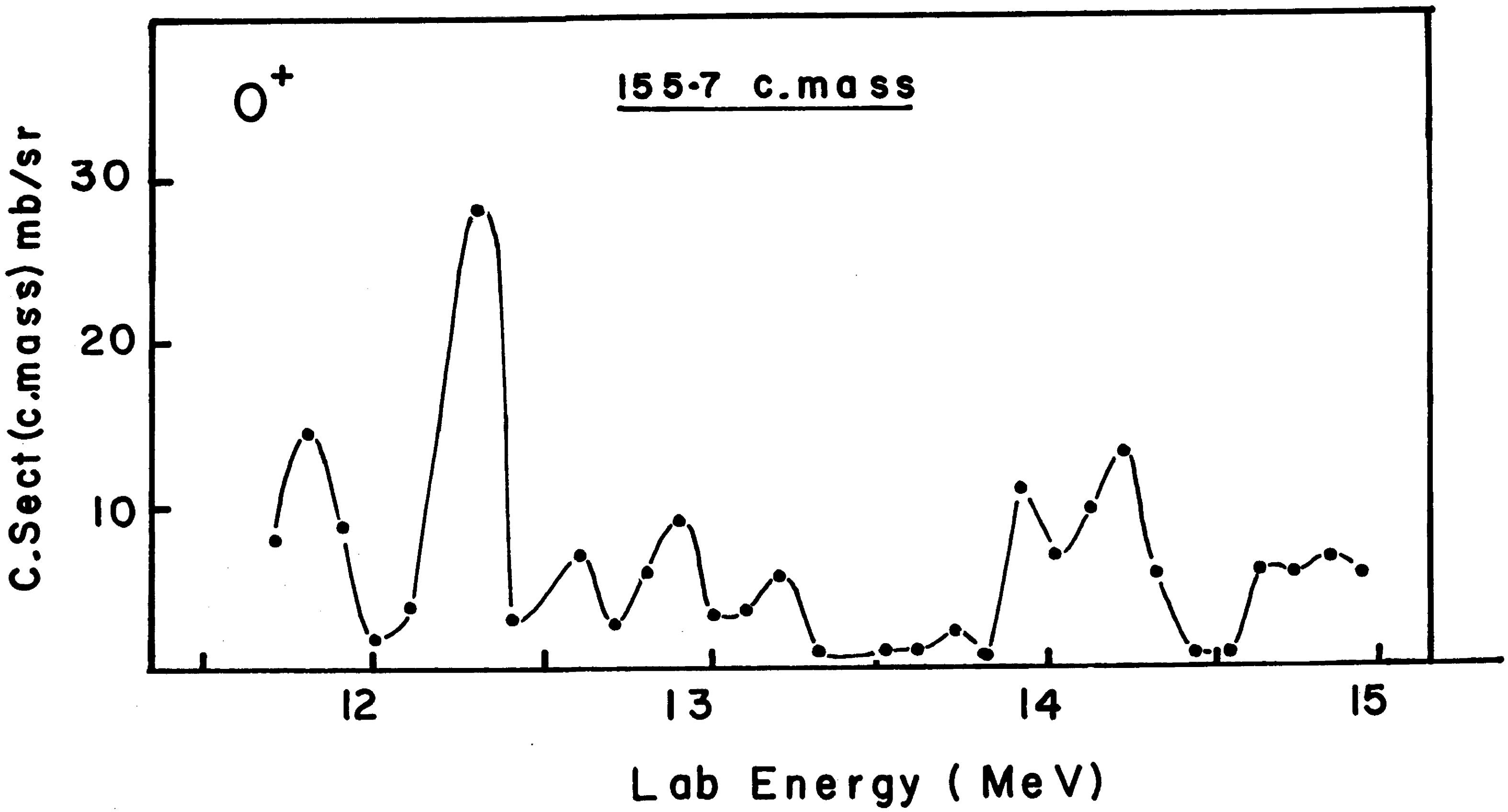

FIGURE 4.1(d) Excitation function of alpha elastic scattering on ^{20}Ne measured in $\approx$100 k ev intervals at 150^{0} (Lab); the solid line through the data points has been drawn by eye

in steps of ≈25 kev at laboratory angles of 80°, 120°, 140° and 160°; preliminary measurements had indicated that the structure in the 150° excitation function was more enhanced at 140°. The energy range of the measurements yielded a range of excitations in ^{24}Mg encompassing the excitation energies of four of the states described as quasi-molecular. The measurements were taken with a gas cell pressure of ≈40 mm and an energy resolution of approximately ±25 kev; the relative energy scale was accurate to within ±6 kev with the object and image slit gaps set at 2·0 mm and 2·5 mm respectively; the absolute energy scale was accurate to within ±30 kev (see sections 2.2 and 2.10). Table 4.2 summarizes these excitation function measurements at ≈25 kev intervals.

Table 4.2

Laboratory Angle of Detection	Scattering State of ^{20}Ne	Laboratory Energy at Centre of Gas Cell (MeV)
80°	0^+	12·045 - 13·457
	2^+	12·045 - 13·457
	4^+	12·045 - 13·457
	2^-	12·776 - 13·457
120°	0^+	12·045 - 13·457
	2^+	12·045 - 12·903
	4^+	12·827 - 13·457
140°	0^+	12·045 - 13·457
160°	0^+	12·045 - 13·457

The cross section measurements described in table 4.2 are tabulated in appendix III and plotted in figures

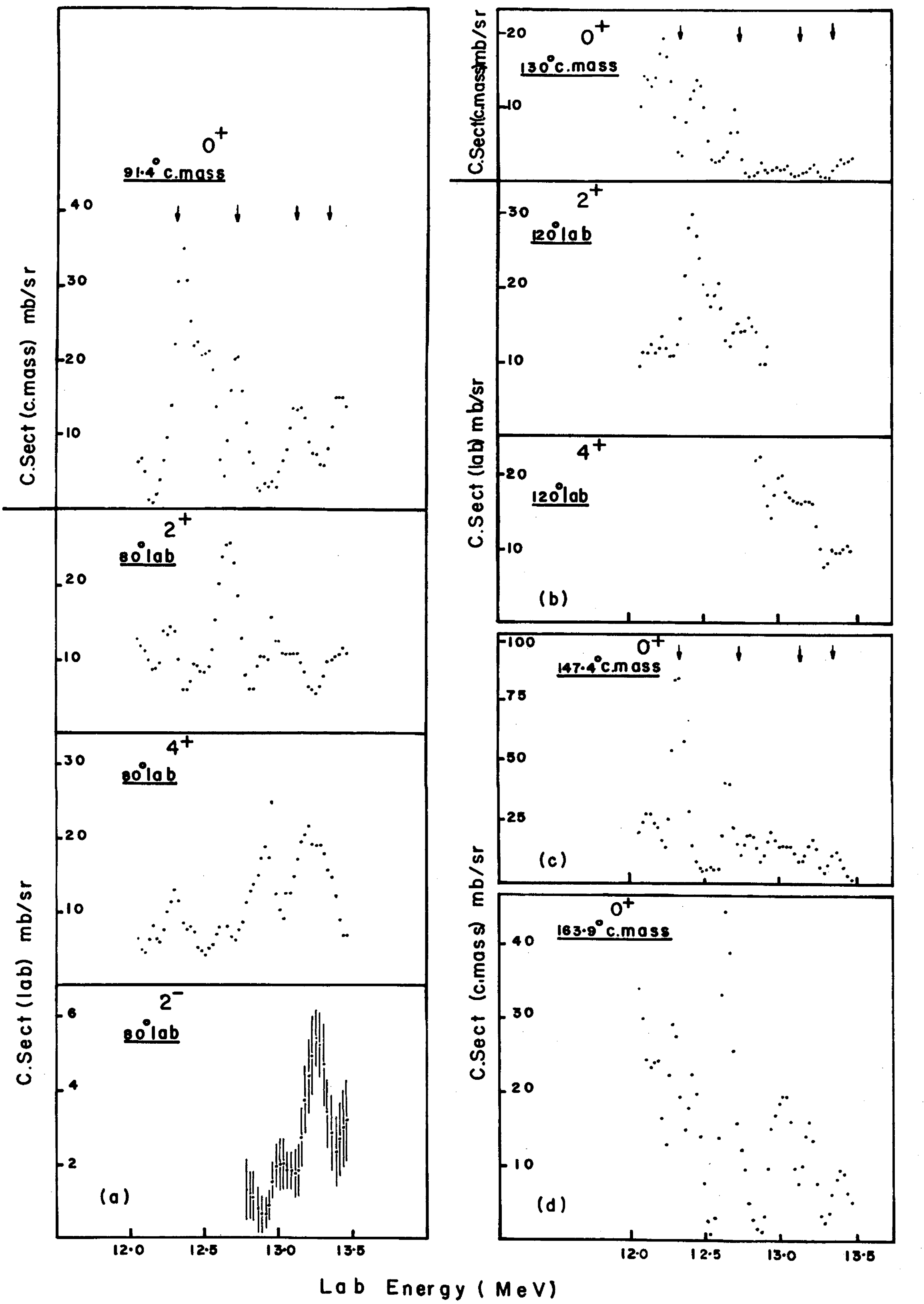

FIGURES 4.2(a), (b), (c) and (d) Excitation Functions of Alpha Scattering on ^{20}Ne Measured in ≈25 kev Intervals

4.2(a), (b), (c) and (d). As before the cross sections are tabulated and plotted with relative errors and are given in the centre of mass co-ordinate system for elastic scattering and in the laboratory co-ordinate system for inelastic scattering. In the figures 4.2, arrows indicate the incident energies corresponding to excitations in ^{24}Mg of the quasi-molecular states.

It was not possible to satisfactorily estimate over the wide energy range of the excitation functions contaminant corrections due to $^{12}C(\alpha,\alpha_0)^{12}C$ at $\theta(lab)=60^\circ$ and $^{16}O(\alpha,\alpha_0)^{16}O$ at $\theta(lab)>120^\circ$ and as a result the scattering via the 2^+ state is not given at these angles. Further gaps in the data of tables 4.1 and 4.2 correspond to measurements for which the groups of interest were obscured by background in the low energy region of the spectra.

4.2 Angular Distributions

The greater part of the experimental work was devoted to the measurement of angular distributions of alpha particles scattered elastically and inelastically from ^{20}Ne. With the view that some systematics in the characteristic energy dependence of the excitation function could become apparent, the angular distribution measurements were confined almost entirely to two energy ranges encompassing pronounced structure in the elastic scattering excitation functions.

One series of angular distributions was measured at seven incident energies, included in table 4.3, from 13.69 to 14·90 MeV at intervals of ≈200 kev. This range of energies includes the pronounced structure observed at an angle of 91·4° (c.mass) in the excitation function of elastic scattering; see figure 4.1(c). Additional measurements were obtained at 12·70 MeV and 11·67 MeV thus providing some indication of the cross section angular dependence over the full energy range covered in the excitation function data. These distributions were measured using a gas cell pressure of ≈70 mm and consequent energy resolution of approximately ±35 kev (see section 2.10).

The second series of angular distributions was measured at five energies, also included in table 4.3, in the range 12·217 to 12·404 MeV at intervals of ≈50 kev. The data were recorded using a gas cell pressure of ≈40 mm and attendant energy resolution of approximately ±25 kev (see section 2.10). It was considered that angular distributions spanning the well defined structure at ≈12·31 MeV in the backward angle elastic scattering excitation function, seen in figure 4.2(c), would provide data particularly amenable to analysis incorporating resonant energy dependence and would consequently furnish some information on a region of excitation in the compound system already noted to be of interest (see section 4.1).

Table 4.3

Energies (Lab) at Centre of Gas Cell in MeV for Angular Distribution Measurements

11·67	12·217	12·257	12·307	12·358	12·404	12·70
13·69	13·92	14·09	14·30	14·50	14·70	14·90

The angular distributions at these fourteen energies were measured at 5° intervals within the angular range of 15° to 160° (Lab); there were a few measurements at intervals of $<5^\circ$ and at angles $>160^\circ$. The angular range of the distributions for inelastic scattering decreases with increasing angle at the lower energies, and the distributions for scattering via the 2^- state and $(3^-,1^-)$ states are restricted to the seven highest energies; with decreasing beam energy and increasing angle the groups in the spectra successively merged with low energy background such as is seen in figure 3.1.

All angular distribution data are plotted in figures 4.3(a), (b), (c), (d) and (e). The data have been plotted to show the angular distributions of scattering from each state as a function of the incident energy. The cross sections and associated errors (see section 3.5) for the elastic and inelastic angular distributions are tabulated in appendix IV.

The angular distributions measured at incident energies of 11·67, 12·70 and 14·50 MeV were each measured

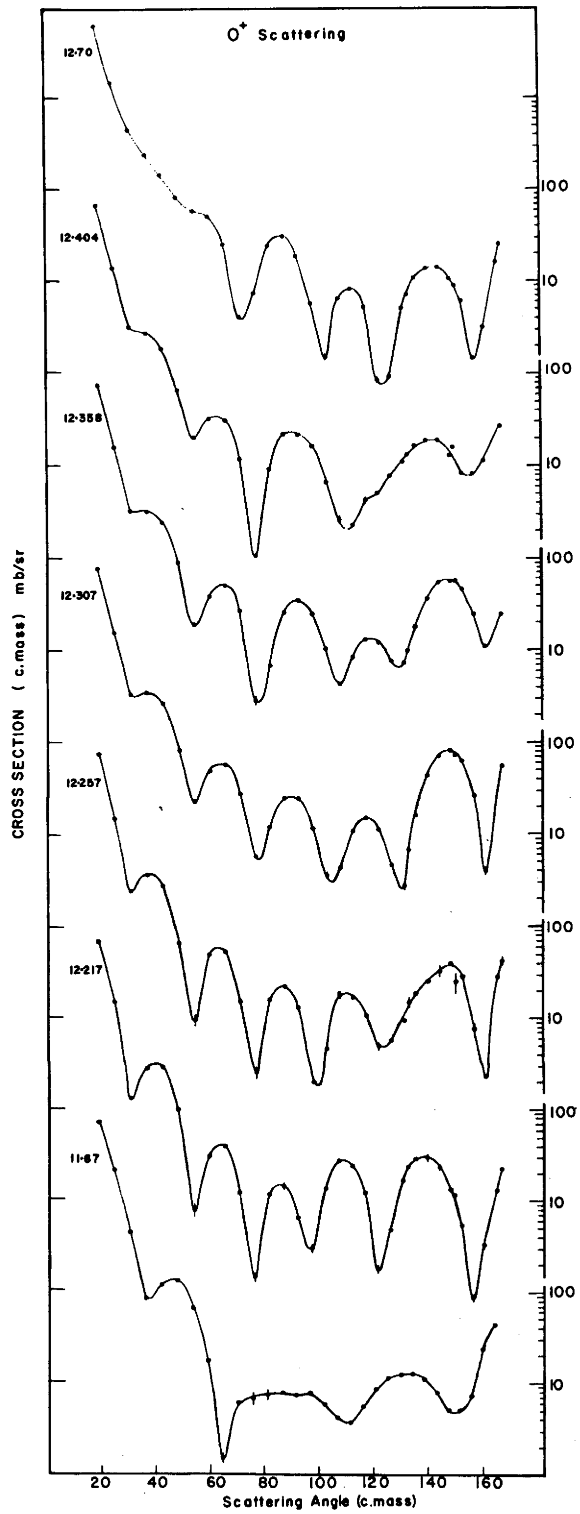

FIGURE 4.3(a) Angular Distributions of the Elastic Scattering of Alpha Particles from ^{20}Ne; the solid lines through the data points have been drawn by eye and significant error bars are shown

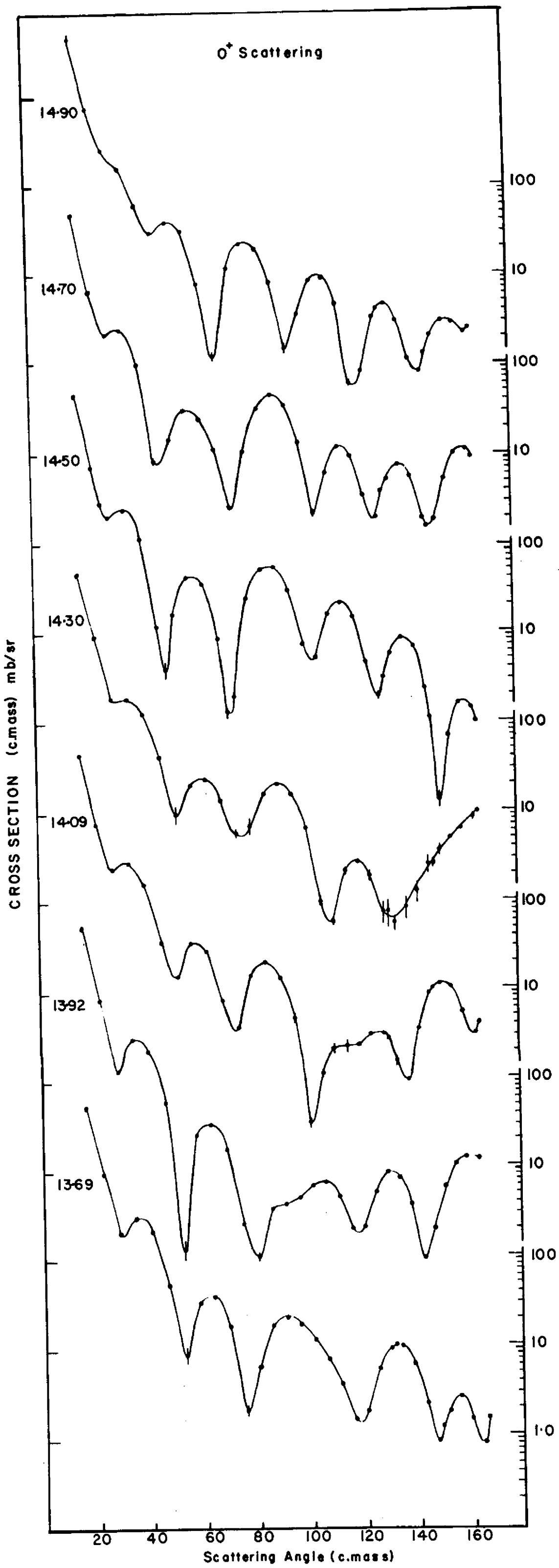

FIGURE 4.3(a) Continued

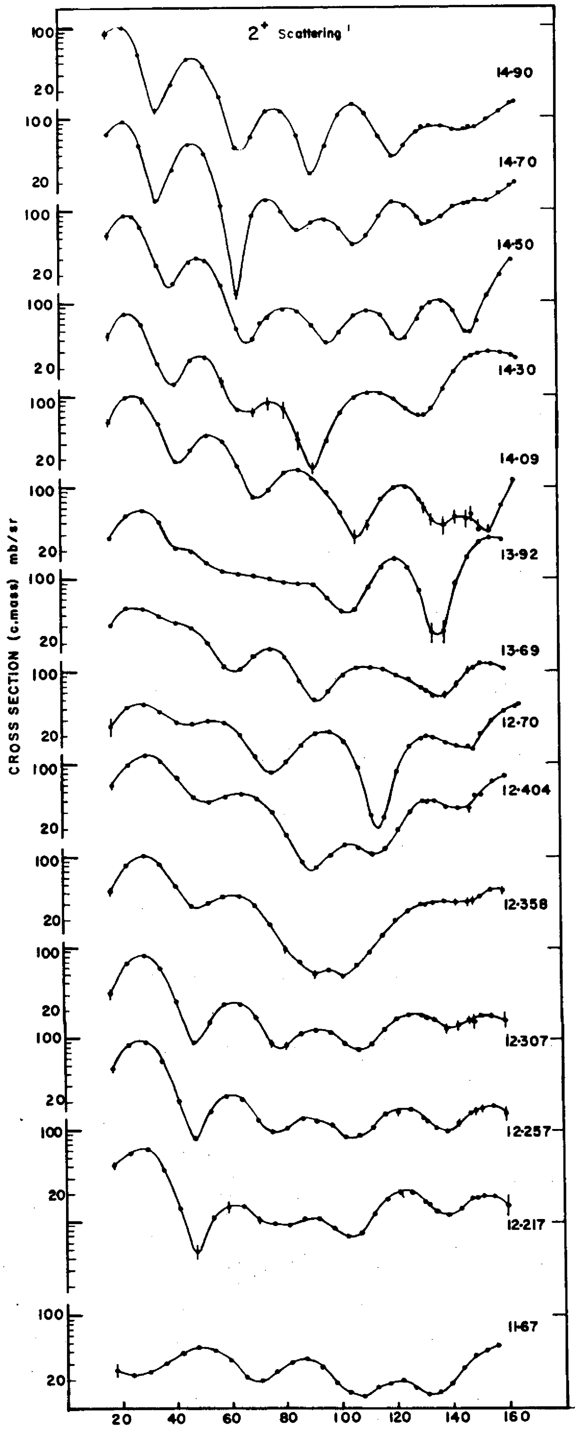

FIGURE 4.3(b) Angular distributions of inelastic alpha scattering from the 1·63 MeV state of ^{20}Ne; the solid lines through the data points have been drawn by eye and significant error bars are shown

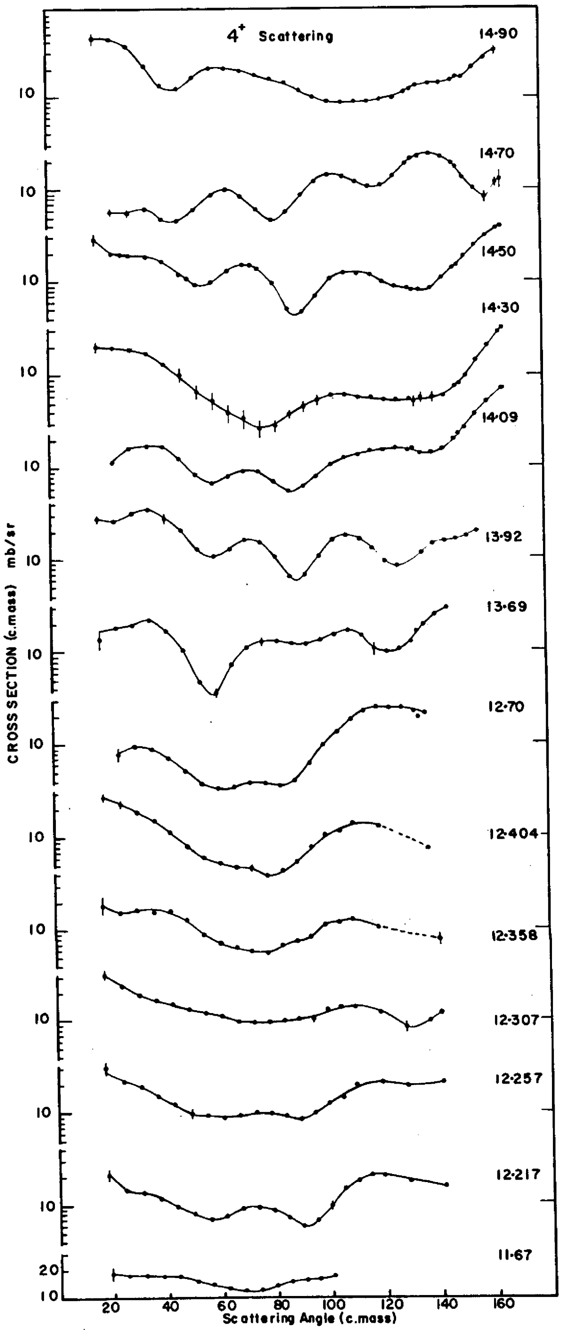

FIGURE 4.3(c) Angular Distributions of Inelastic Alpha Scattering from the 4·25 MeV state of ^{20}Ne; the solid lines through the data points have been drawn by eye and significant error bars are shown

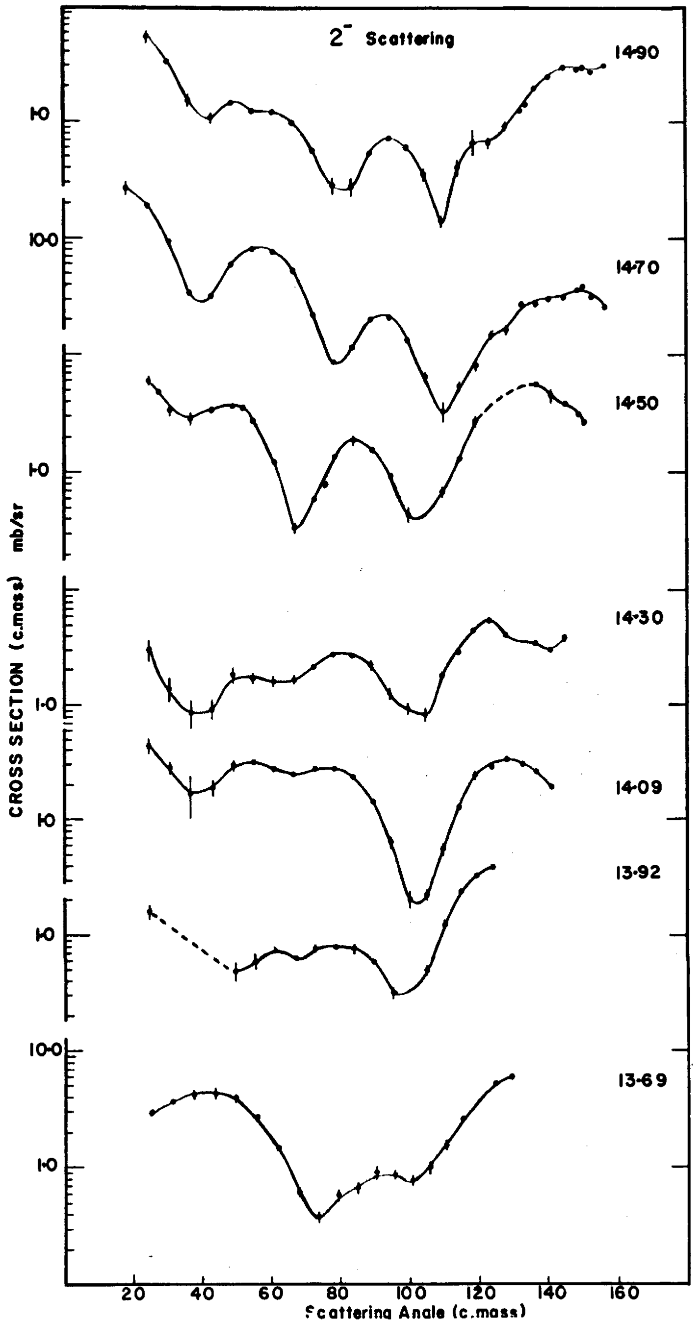

FIGURE 4.3(d) Angular distributions of inelastic alpha scattering from the 4·97 MeV state of ^{20}Ne; the solid lines through the data points have been drawn by eye and significant error bars are shown

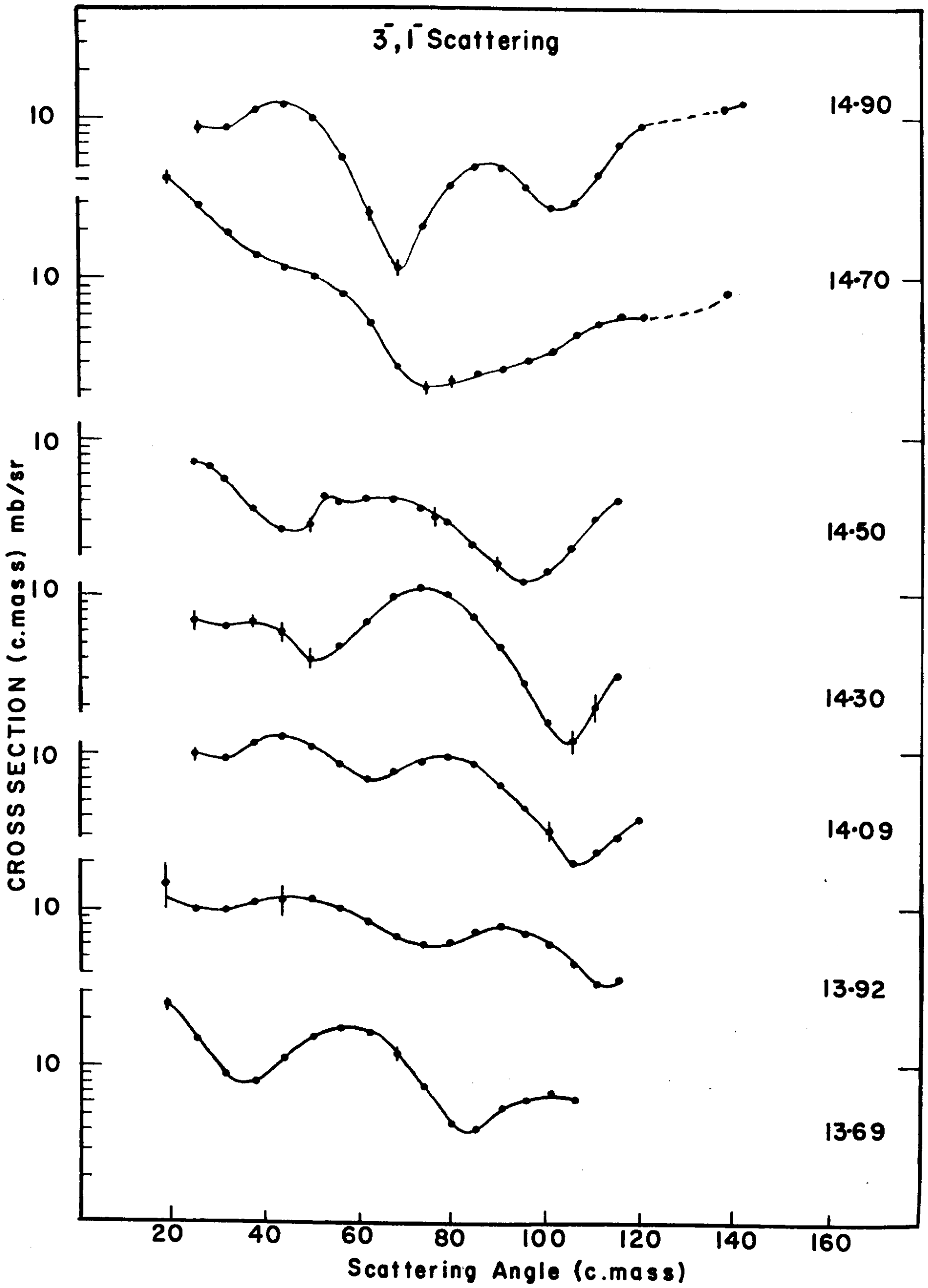

FIGURE 4.3(e) Angular distributions of inelastic alpha scattering from the 5·63 and 5·80 MeV states of ^{20}Ne; the solid lines through the data points have been drawn by eye and significant error bars are shown

twice but the final cross sections are those of the re-measurements and not a mean of the two sets of data although good overall agreement was obtained. The initial measurements at these three energies had been obtained under the same experimental conditions as the 100 kev excitation function measurements and because of the energy shifts thus possible (see section 4.1) were considered the source of non-statistical discrepancies between the two sets of data. The remeasurements at these three energies as well as the angular distributions at all other energies were obtained with the incident energy more precisely defined by object and image slit gaps of 2·0 and 2·5 mm respectively (see sections 2.2 and 4.1). The greatly improved reproducibility of data under these conditions highlighted the problem and effect of energy shifts and justified the neglect of the initial measurements at 11·67, 12·70 and 14·50 MeV.

The angular distributions at the energies 13·69, 14·09, 14·30, 14·70, 14·90 and at the five energies from 12·217 to 12·404 MeV were all derived from the mean of cross sections from two separate sets of measurements in which the overlap of angles covered in each was for the most part complete. A few data points were measured once only while within the initial measurements at each energy there were numbers of repeat measurements. As it eventuated all re-measurements at a given energy were performed at the experimental station alternative to that used initially (see section 2.2). The distributions at the five energies from 12·217 to 12·404 MeV were initially measured over the full angular range for each energy in turn as was the usual practice; the remeasurements were obtained by varying the energy at each angular setting of the three detectors.

The angular distributions at 13·92 MeV were derived from one series of measurements; the additional accelerator run necessary for remeasurement was not warranted in view of the reproducibility of data obtained at other energies during the same series of measurements.

Non-statistical deviations were apparent however in the two sets of distributions measured at 14·30 MeV; the extent of the deviations is indicated by the relatively larger error bars seen in the plots of the data at this energy in figures 4.3(a) to 4.3(d). The cause of the deviations is almost certainly a systematic energy difference, estimated to be ≈20 kev, between the two sets of measurements. The source of such an energy difference is not apparent as all remeasurements were conducted after normalization of the energy scale by an appropriate excitation function measurement. The uncertainty of normalization of the energy scale prior to all other remeasurements was considered better than ±10 kev and the reproducibility of the distributions at the five energies 12·217 to 12·404 MeV at ≈50 kev intervals illustrated the adequacy of energy definition and reproducibility. The need for this energy scale normalization occurred because of the number of nickel entrance foils used (see section 2.10).

The values of the five energies from 12·217 to 12·404 MeV are quoted to three decimal places as the uncertainty in the relative energy scale was estimated to be within ±10 kev. All other energies of distribution measurements are given subject to the absolute uncertainty of ±30 kev and are thus quoted to two decimal places.

The measurements common to the angular distributions and excitation functions were found to be in satisfactory agreement; some differences were apparent in the comparison involving the excitation functions measured in 100 kev steps but these were consistent with the evaluation of energy scale discrepancies discussed in section 4.1.

4.3 General Remarks on Cross Section Measurements

The 0^+ scattering angular distributions seen in figure 4.3(a) are characterized by diffraction type oscillations with the trend in cross section at forward angles determined by coulomb scattering. The distribution shapes show a marked energy dependence and in particular the enhancement of the maxima at $\approx 90^\circ$ and $\approx 150^\circ$ at incident energies of 14·50 and 12·307 MeV respectively reflects the pronounced structure of the elastic scattering excitation functions (see figure 4.1(c) and 4.2(c)). The angular distributions for inelastic scattering are also seen to exhibit diffractive structure and energy dependence of shape although to lesser degrees to that seen in the elastic scattering (see figures 4.3(b) to (d)). The diffractive nature and energy dependence of the shape of the elastic scattering angular distributions are akin to that seen in equivalent measurements on other light nuclei (So 66, Wa 66, Me 67). For the inelastic angular distributions such a comparison cannot be made as there is a paucity of related results published.

The positions of the maxima and minima of the elastic scattering angular distributions are plotted as a function of incident energy in figure 4.4(a). The detail of lines through points in regions where behaviour is irregular is rather subjectively drawn. The regions of the figure donoted by *a*, *b*, *c*, *d* and *e* indicate where a diffraction maximum is seen to vanish. A decrease in cross section over a substantial angular range adjacent to a maximum accompanies its disappearance and the energies at which these changes occur correspond to minima in the integrated cross section which is plotted in figure 4.6 and discussed below. This correspondence suggests that the terminology of a disappearing maximum is appropriate and that energy dependence of the integrated and differential cross section is reflected in a plot such as that of figure 4.4(a).

The 2^+ angular distributions are characterized by

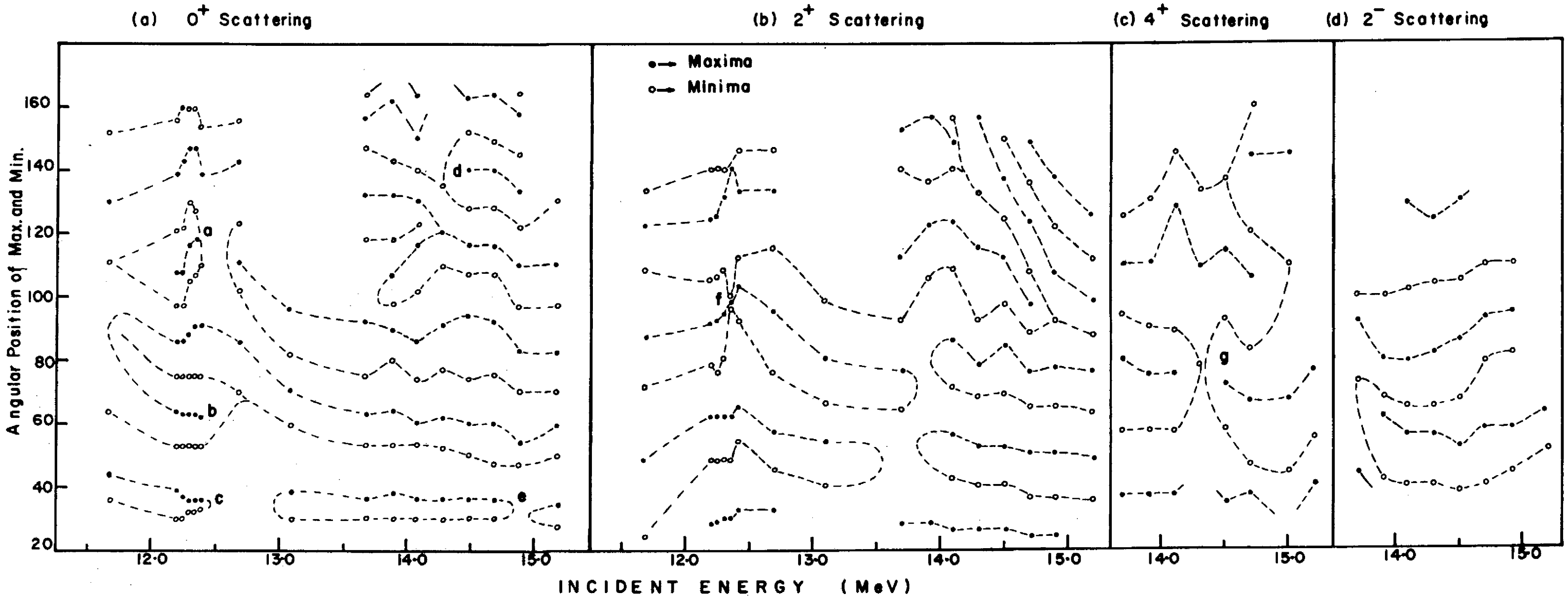

FIGURES 4.4(a), (b), (c) and (d)

Angular Variation of Maxima and Minima
of Angular Distributions

diffractive oscillations of smaller amplitude than those of elastic scattering and by in general a well-defined forward angle peak. The positional variation of the maxima and minima as a function of energy, as shown in figure 4.4(b), is ill-defined at the backward angles for higher energies and underlines the energy dependence of shape. The letter f denotes, in figure 4.4(b), a region where the disappearance of a maximum is clearly seen. Although the correlation discussed above for elastic scattering is not evident the energy dependence of the differential cross section is reflected in this figure.

The distributions of inelastic scattering from the 4^+, 2^- and $(3^-,1^-)$ states are seen in figures 4.3(c), (d) and (e) to exhibit varying degrees of diffractive structure. The oscillations of the 2^- distributions are the most pronounced and are comparable in amplitude to those of the 2^+ distributions. The shape of the 2^- distributions shows also a more systematic trend with energy than the 4^+ or $(3^-,1^-)$ distributions although the cross section over the forward hemisphere is quite energy dependent. The positional variation of the maxima and minima of the 4^+ and 2^- distributions is indicated as a function of energy in figures 4.4(c) and (d). Because of the damped nature of the low energy 4^+ distributions, figure 4.4(c) includes only the higher energy distributions. An equivalent plot for the $(3^-,1^-)$ distributions is omitted because of the irregularity of shape in the limited range of data obtained. The pronounced irregularity of figure 4.4(c), denoted by *g* occurs at an energy corresponding to that of the minimum in the integrated cross section for scattering from the 4^+ shown in figure 4.6. Again it is seen that plots of the type shown in figure 4.4 may strongly reflect energy dependence of the differential and integrated cross section.

Ivașcu et al (Iv 67) measured angular distributions of elastic and inelastic alpha scattering from ^{20}Ne at incident energies of 13·1, 14·5 and 15·2 MeV. A comparison of Ivascu's results and the present results nominally at the same energy of 14·5 MeV shows as seen in figure 4.5, discrepancies which are most pronounced for the 4^+, 2^- and $(3^-,1^-)$ distributions. Further examination of the present excitation functions and the trend in distribution shapes with energy indicate that Ivascu's results have actually been obtained at an energy ≈100 kev above the 14·50 MeV ±0·03 MeV incident energy of the present measurements and the two sets of data can be considered as quite consistent and complimentary. The 13·2 and 15·2 MeV results of Ivascu have been incorporated in the plots of figure 4.4.

At angles beyond the range both of pronounced coulomb scattering and the forward angle peak of the 2^+ distributions the differential cross section for scattering from the 0^+, 2^+ and 4^+ states are of comparable magnitude

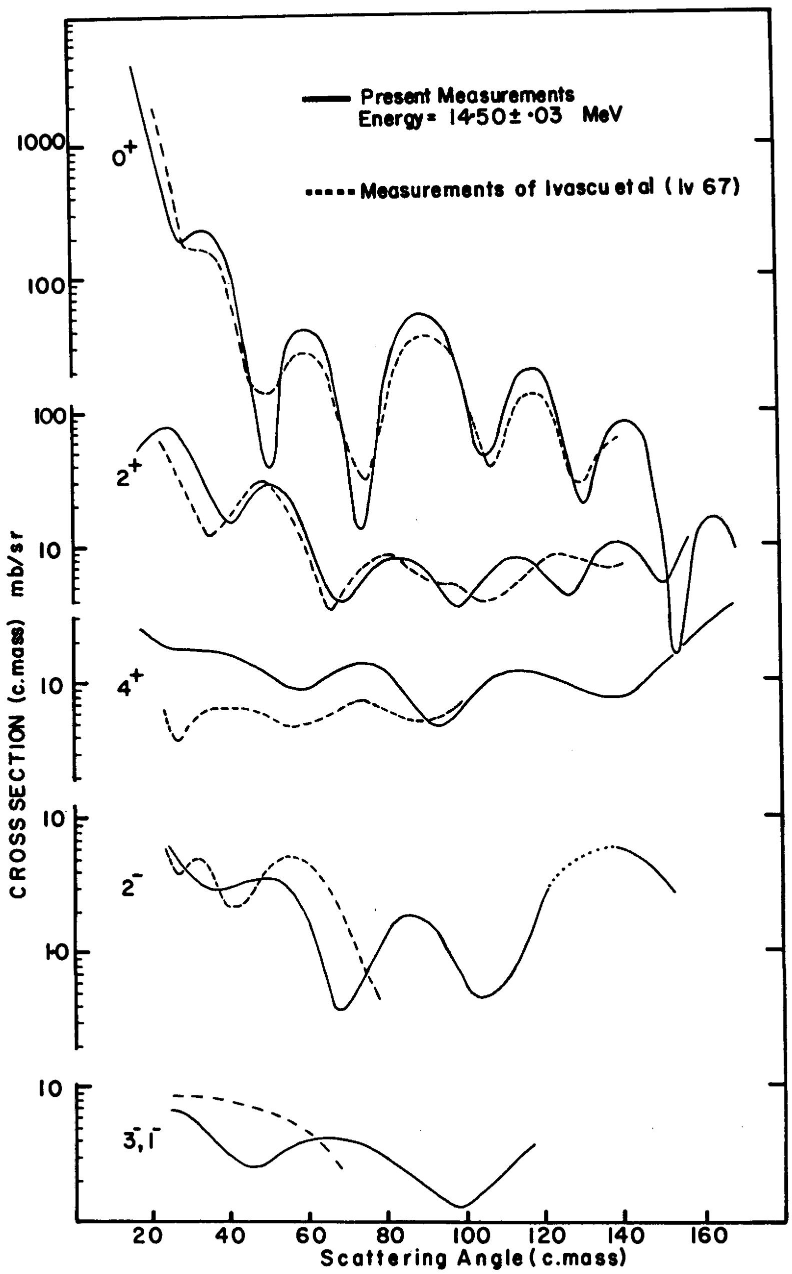

FIGURE 4.5 Comparison of present measurements with those of Ivascu et al (Iv 67)

and oscillate around a value of ≈10 mb/sr. The differential cross sections of the 2^- distributions are centred around a value of ≈2 mb/sr while those of the $(3^-,1^-)$ distributions combined are intermediate between 2 and 10 mb/sr. The relative magnitudes of cross section for scattering from the various states are quantitatively indicated by the integrated cross sections shown in figure 4.6. Applications of the trapezoidal sum rule to the expression

$$2\pi \int_{\Theta_1}^{\Theta_2} \sin\Theta \frac{d\sigma(\Theta)}{d\omega} d\Theta$$

yielded the integral of the cross section in the angular range Θ_1 to Θ_2. The largest angular range common over all energies determined the values Θ_1 and Θ_2 for each state and although the ranges were not identical the relative magnitudes of the integrated cross section for scattering from each state are indicative of the description above. The error bars ascribed to be the integrated cross sections of figure 4.6 represent an extreme estimate made in order to include deficiencies in trapezoidal summing and were obtained by applying the above integral to the differential cross section plus error.

The integrated cross sections for scattering from each state, shown in figure 4.6, exhibit structure corresponding in energy and to a degree in amplitude to that shown by the excitation functions of differential cross section in

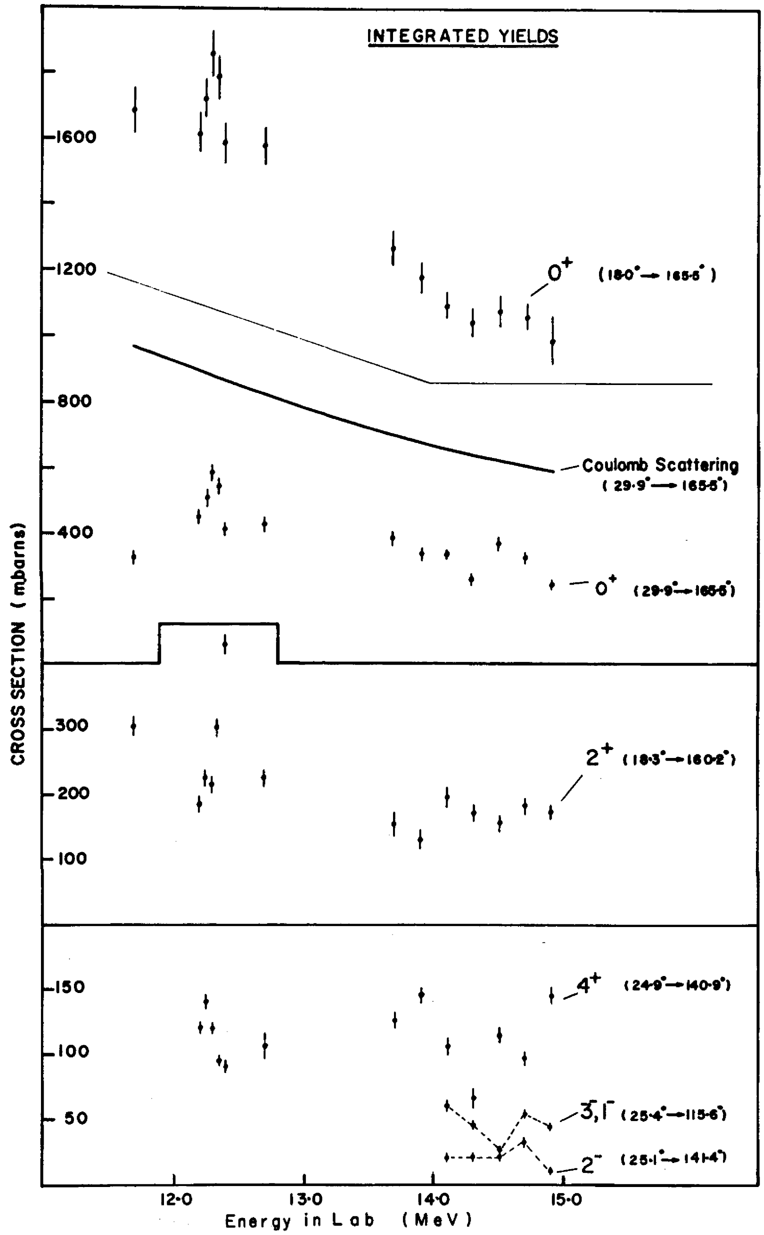

Figure 4.6 Angle Integrated Cross Sections

figures 4.1(a) to (d). The integrated cross section for elastic scattering at 12·31 MeV is seen to be even more enhanced by the inclusion of the three forward most angles in the angular range of integration and this highlights the strong energy dependence of the elastic scattering about this energy as at forward angles the energy dependence would be expected to be minimal. Between the states there does not appear to be, in either the integrated or differential cross sections, any marked correlation in the energy dependence of structure; the pronounced peak in the 2^+ integrated yield at ≈12·4 MeV occurs at an energy ≈100 kev above that of the similar structure in the elastic scattering integrated yield.

The structure of the excitation functions for all states measured in the present studies ranges in width from ≈100 to 500 kev. This type of structure characterizes alpha scattering in the energy range 10 to 25 MeV on light mass nuclei. Takeda et al (Ta^1 67) have measured excitation functions and angular distributions for alpha scattering from ^{20}Ne over the energy range 20 to 24 MeV. The well-defined structure, of width and spacing of ≈500 kev, in their elastic scattering excitation function at 175·75° (Lab) shows that the broad structure of the present measurements persists at these higher energies; the excitation function for scattering from the 2^+ state, also at 175·75° (Lab), shows structure uncorrelated with that of the elastic scattering and which is also broader and less pronounced. So et al (So 66) described excitation function measurements of elastic alpha scattering on ^{24}Mg in the energy range 8 to 19 MeV in terms of resonance structure of ≈1 MeV width as well as fine structure of ≈80 kev width. Watson et al (Wa 66) discussed excitation functions of alpha scattering from the ground and first three excited states of ^{26}Mg for incident energies from 8 to 12 MeV in terms of large structure of width from 100 to 300 kev.

4.4 Comparison of Present Measurements with those at Higher Energies

Angular distributions of elastic and inelastic alpha scattering from ^{20}Ne have been measured at a number of energies above those of the measurements of Ivascu (Iv 67) and the present studies; these energies are listed in table 4.5 together with the appropriate reference.

Table 4.5

Energy (MeV)	18·02	20 - 24	22·0	27·3	42·0	50·9
Reference	Se 58	Ta[1] 67[(a)]	Ei[1] 62	Ko 65	Bl 64	Sp 65

(a) includes an excitation function at 175·75° (Lab) and an elastic scattering angular distribution at 21·6 MeV.

The higher energy angular distributions show diffractive type oscillations which with the exception of the 2^- scattering are more regular and well-defined than seen in the present results. The phase relationships of the oscillations in the scattering from various states at these higher energies can be interpreted in terms of the phase rules of Blair (Bl 65). The phase rules derived from a diffraction model description of direct reaction scattering with strongly absorbed projectiles state that :

(i) even (odd) parity single step inelastic excitations will have angular distributions whose oscillations are out of (in) phase with those of the elastic scattering; and

(ii) two step inelastic excitation reverses the phase of oscillation relative to that of a single step excitation.

As was pointed out by the various authors cited in table 4.5 the 0^+ and 2^+ distributions of all these higher energy measurements are out of phase for the first two or three oscillations and are indicative of direct elastic and inelastic scattering with the inelastic proceeding by a single step transfer of two units of angular momentum. Springer (Sp 65) pointed out that the 2^+ scattering at 50·9 MeV shows a phase close to that expected for single excitation although an improvement in fitting the data to the theory was obtained by addition of a two step excitation contribution.

In the present measurements the phase relationships observed at the higher energies for the 0^+ and 2^+ distributions persist to a certain extent. At the energies of 14·09 to

14.70 MeV the angular ranges defined by the first two minima in the 0^+ distributions approximately correspond to those defined by the first two maxima of the 2^+ distributions. These details are seen in figure 4.7(a); the sets of angular distributions at each energy are plotted together in figures 4.7(a) and (b).

The 4^+ distribution at 42·0 MeV and 50·9 MeV shows a well-defined diffraction pattern which is out of phase with the 2^+ distribution and Springer interpreted the 50·9 MeV data in terms of a dominant contribution from a two step direct excitation. At lower energies the 4^+ distribution becomes less well related in phase to the 0^+ and 2^+ distributions and for the present measurements shows no systematic phase relationship.

The present measurements and those at 22 and 28 MeV for the 2^- distributions have well-defined diffraction patterns; the structure however is a little dampened at 42 MeV and finally vanishes at 50·9 MeV. Accompanying this loss of the diffractive nature of the 2^- distribution is a decrease in cross section over the energy range defined by the present measurements and those of Springer at 50·9 MeV. The 2^- and 0^+ distributions at 28 and 22 MeV are in phase while at the present energies of measurement no such systematic is seen.

The distributions from the $(3^-,1^-)$ states were resolved at 50·9 MeV with the cross section for scattering

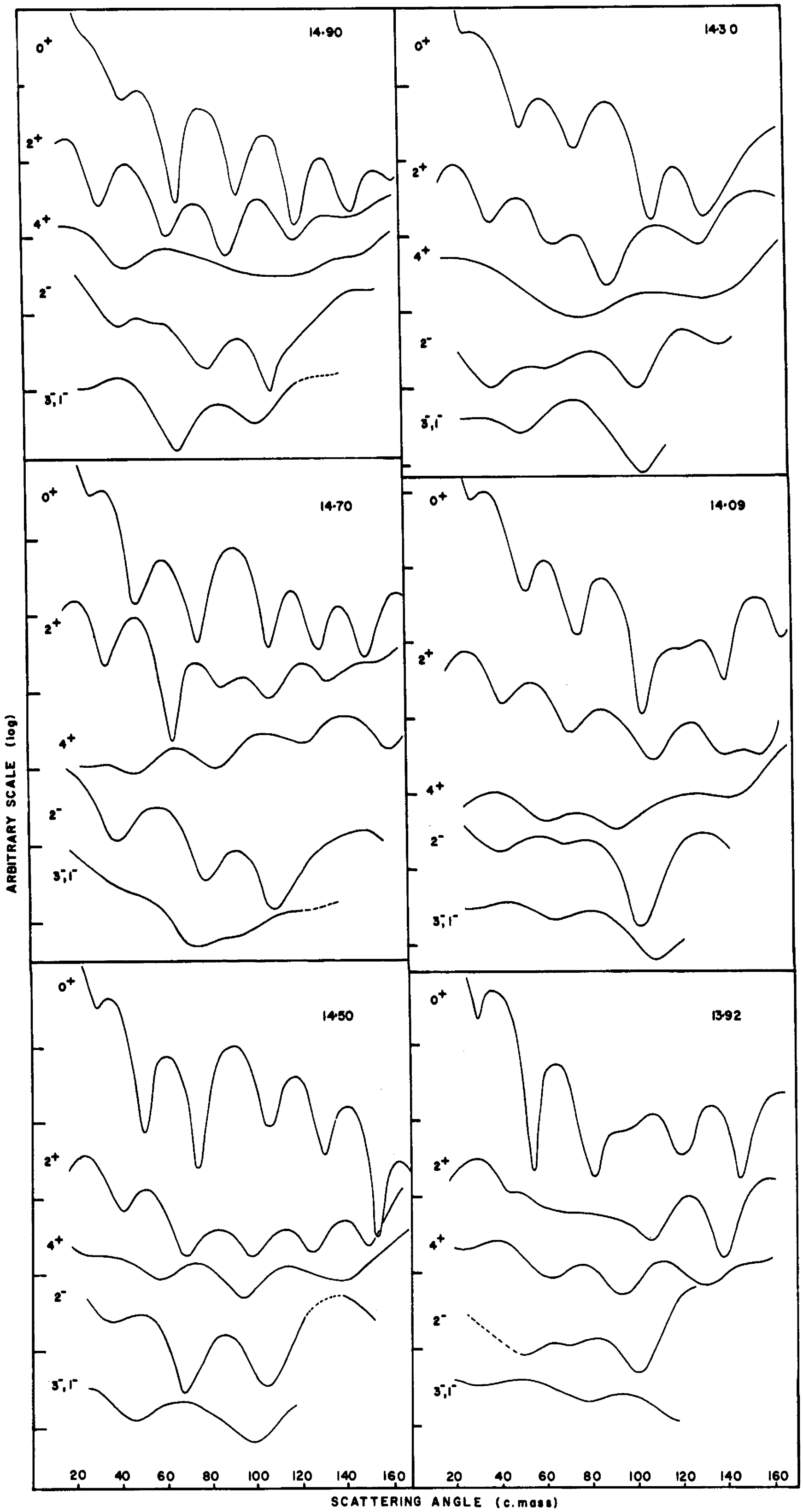

FIGURE 4.7(a) Solid Line Representations of Measured Angular Distributions on Arbitrary Scale

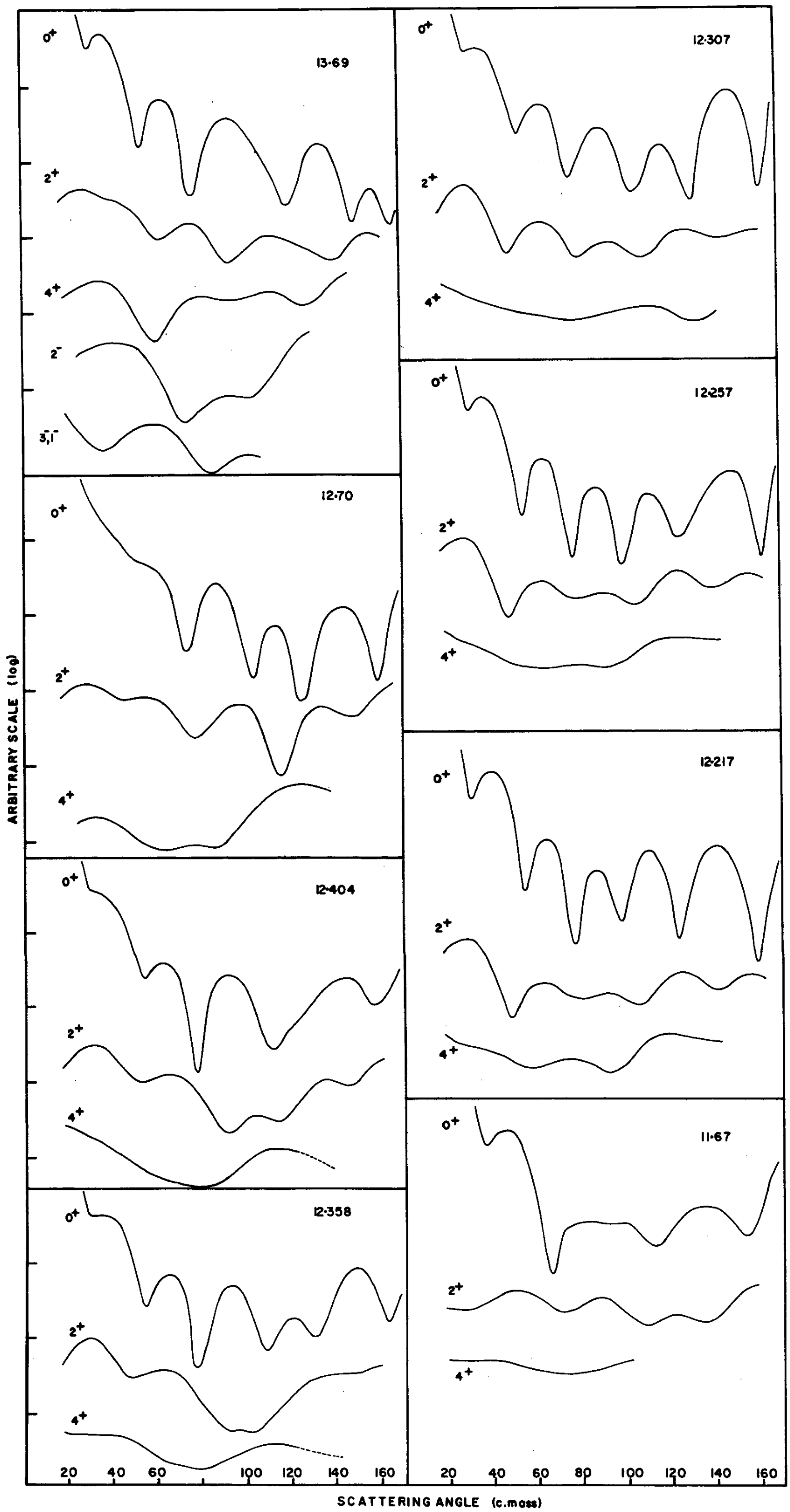

FIGURE 4.7(b) Solid Line Representations of Measured Angular Distributions on Arbitrary Scale

from the 3^- state enhanced by a factor of ten over that of the 1^- state. Springer interpreted the 3^- distribution (in phase with the 0^+) in terms of a single step excitation and that of the 1^- (out of phase with the 0^+) in terms of a two step excitation. The unresolved distributions of the $(3^-,1^-)$ scatterings are in phase with that of the 0^+ at 28 MeV while at 22 MeV and the energies of the present measurements there is no relationship apparent.

In comparison with the decrease in cross section of the 2^- scattering over the range of energies discussed the 0^+, 2^+, $(3^-,1^-)$ and to a lesser extent the 4^+ scattering show approximately the same magnitude of differential cross section over corresponding maxima at forward angles.

The period of oscillation in the diffractive patterns of the 0^+ and 2^+ distributions, for which in general it is seen to be relatively well-defined, systematically decreases from ≈ 26-30° at 14·90 MeV to ≈ 12-13° at 50·9 MeV. This dependence is approximately in accord with the phenomenological description of Blair. The differential cross section at angle Θ for elastic scattering in this description is proportional to the square of the first order Bessel function, i.e. $J_1{}^2(kR\Theta)$, where k is the wave number of the incident and scattered wave, and R is a model dependent parameterization of the nuclear radius. Taking Blair's value of $R \approx 6$ fermi, from the 42 MeV data analysis, the periodicities of the angular distributions corresponding to 14·9 and 50·9 MeV are predicted to be $\approx 12^{\circ}$ and $\approx 22^{\circ}$ respectively.

In the present measurements it is noted the periodicity of the scattering from the various states increases with the excitation energy of the state. Although this effect is not considered in the diffraction models, in which the adiabatic approximation is implicit, it seems consistent with a diffraction model interpretation in which the wave number k for each scattering state is explicitly used to determine the periodicity of a function of the form $J_1{}^2(kR\theta)$. The lack of any phase relationship for the 4^+, 2^- and $(3^-,1^-)$ distributions with the 0^+ distributions is then not unexpected in the present measurements as for example at 14·0 MeV incident energy the ratio (k incident/k scattered) for scattering from the 4^+ state is $\approx 1 \cdot 25$; the same ratio for scattering from the 2^+ state, for which some systematic phase relationship with the 0^+ distribution was observed, shows less mismatch and is $\approx 1 \cdot 08$.

CHAPTER 5
Optical Model Analysis of Elastic Scattering

The angular distributions of elastic scattering of the present measurements have been analyzed in terms of the nuclear optical model. This description of the elastic scattering is in qualitative agreement with the data at energies less influenced by the pronounced structure seen in the excitation functions and is indicative of an average optical potential.

5.1 Applicability of Optical Model Analysis

A description of direct elastic scattering is given by the nuclear optical model. The basic assumption of the model is the simulation of the interaction of the incident particle with the target nucleus by a one body complex potential. As such it can be expected that the model is capable of describing the energy averaged behaviour of scattering and that it is insensitive to detailed structure such as compound resonance excitations. A valid comparison of the predictions of the model with experiment requires of the measurements that the effect of interference between shape elastic and compound elastic has been averaged over and that the averaged compound elastic scattering is negligible. Both these conditions would be simultaneously satisfied in scattering where the energy of the compound system is such that many resonances contribute to the scattering amplitude at a particular energy. Brown (Br 64) and McCarthy (Mc 65) have discussed the justification of the optical model in the above terms.

In the present studies the excitations of the compound ^{24}Mg system of $\approx$20 MeV correspond, as noted in chapter one, to the region where $\langle\Gamma\rangle/\langle D\rangle \gg 1$. However as has been shown by the comprehensive measurements of the Florida accelerator group (Da 66, Al 68) and as indicated in the present measurements the differential cross sections for elastic alpha scattering on light nuclei at energies <20 MeV are characterized by energy dependence more pronounced than that compatible with predictions of the optical model. On the other hand such measurements yield angular distributions of a diffractive nature which are indicative of the direct elastic scattering of alpha particles as is described by the optical model. From the discussion of section 4.4 it can be remarked that the periodicity and cross section magnitude of the elastic scattering angular distributions of the present measurements appear related to the higher energy measurements for which an optical model analysis would be rather more justified.

The model suggested by Robson, as discussed by Davis (Da 66) and Aldridge et al (Al 68), incorporates the typical energy dependence of alpha scattering on light nuclei in terms of a modified optical potential. Robson proposed, in generalizing the optical model, a mean optical potential and a fluctuating potential which describes the effect of intermediate structure and compound resonances. In terms of this suggestion the mean potential will be reflected in the average value of potential strengths obtained from the optical model parameters fitting data over a range of energies sufficiently large to encompass observed structure.

In describing elastic scattering via the optical model the imaginary potential is interpreted as representing the effect of all non-elastic processes and it is implicit in the model that none of these processes is dominant or comparable to the elastic scattering in cross section. However scattering from nuclei which are deformed or deformable is characterized by direct inelastic scattering comparable in cross section to that of the elastic scattering and a rigorous theoretical description requires an explicit treatment of these dominant processes (Br 60, Br 64). In the discussion of section 4.3 it was noted that the elastic, 2^+ and 4^+ differential cross sections of the present measurements were of comparable magnitude at angles where the elastic is not dominated by the coulomb scattering. Thus as is considered in detail in chapter six an explicit treatment, employing a deformed potential rather than an implicit treatment employing a spherical potential, to incorporate the inelastic scattering appears warranted and more consistent with the formulation of the optical model and the rotational nature ascribed to the low lying levels of ^{20}Ne. Consequently the present optical model analysis attempts to parameterize the cross section energy dependence and the effects of strong coupling to inelastic channels. As suggested in section 6.7 the present energy dependence appears to be determined to a small degree by the presence of strong coupling.

The 28 and 18 MeV elastic scattering data from measurements of alpha scattering on ^{20}Ne, referred to in section 4.4, have been analyzed in terms of the optical model in two comparative studies of the applicability of the model to a wide range of target nuclei. Lucas et al (Lu 66) in describing the analysis of the 18 MeV data concluded the applicability was marginal although noting the agreement was of comparable quality to that of the 28 MeV studies. Satchler (Sa 65) described the fits to the 28 MeV data of scattering from medium and heavy weight nuclei as good and from the lighter nuclei such as ^{20}Ne as qualitative. Hodgson has pointed out that the greater level density in heavier nuclei usually enhances the success of the model (Ho 63).

In summary then the assumptions made in attempting an optical model analysis of the present elastic scattering data are that :

(i) the direct or shape elastic amplitude represents a significant contribution to the total elastic scattering amplitude; and

(ii) within the parameterization arising from both the need to describe energy dependent data and the implicit treatment of the inelastic scattering, systematics of the direct elastic scattering amplitude will be evident.

It is noteworthy that Aldridge et al (Al 68), in analyzing their very detailed measurements of elastic scattering of alpha particles on ^{32}S at incident energies from 10 to 17·5 MeV, found in the optical model analysis of the typically energy dependent scattering, parameters which are energy dependent but which indicate on average a smooth trend as is implied by the model.

5.2 Form of the Optical Potential Employed

In describing the elastic scattering of the present measurements in terms of the scattering from a spherical optical potential the widely used Saxon-Woods radial form factor has been assumed both for the real and imaginary components of the potential. The potential employed is given by :

$$U(r) = -(V+iW) \frac{1}{1+e^{(r-R_0)/a}} + V_c(r) \qquad (5\text{-}1)$$

where the radial forms of the real and imaginary potentials of depth V and W respectively are described in terms of the same radius parameter R_0, parameterized as $R_0 = r_0 A^{1/3}$ (A is the atomic number of the target) and the same diffuseness parameter a. $V_c(r)$ represents the coulomb potential for a uniform charge distribution within the coulomb radius $R_c = r_c A^{1/3}$. The mathematical formalism of the model and the methods of numerical solution of the radial differential equations arising from insertion of expression (5-1) in the Schroedinger wave equation are discussed in detail by Hodgson (Ho 63) and Melkanoff (Me 65).

The radial wave function $u_\ell(r)$ for each partial wave is obtained by numerical integration of the equation :

$$\left[\frac{d^2}{dr^2} + k^2 - \frac{\ell(\ell+1)}{r^2} - \frac{2m}{\hbar^2} U(r) \right] u_\ell(r) = 0 \qquad (5\text{-}2)$$

where (i) $U(r)$ is given by expression (5-1);

(ii) m is the reduced mass; and

(iii) k is the wave number.

The assymptotic form for $u_\ell(r)$ is :

$$u_\ell(r) \sim F_\ell(r) + \frac{1}{2i} (S_\ell - 1) \left[G_\ell(r) + i\, F_\ell(r) \right] \qquad (5\text{-}3)$$

where $F_\ell(r)$ and $G_\ell(r)$ are respectively the regular and irregular coulomb functions and S_ℓ is a scattering matrix element. The differential cross section is given in terms of the modulus squared of the scattering amplitude $A(\theta)$:

$$A(\theta) = f_c(\theta) + \frac{1}{2ik} \sum_{\ell=0}^{\infty} e^{2i\sigma_\ell} (2\ell+1) (S_\ell - 1) P_\ell(\cos\theta) \qquad (5\text{-}4)$$

where (i) $f_c(\theta)$ is the coulomb scattering amplitude; and

(ii) σ_ℓ is the coulomb phase shift.

The above detail, which is as given by Hodgson (Ho 63), is included to clarify subsequent references. The nuclear phase δ_ℓ and the reflection coefficients η_ℓ are related to the complex scattering matrix elements S_ℓ by :

$$S_\ell = \eta_\ell\, e^{2i\delta_\ell} \qquad (5\text{-}5)$$

η_ℓ for the ℓ^{th} partial wave is the ratio of the amplitude of the outgoing radial wave to the amplitude of the incoming radial wave.

A potential of the form (5-1), referred to in the literature as a four parameter potential, may be generalized to six parameters with independent geometrical parameters for the real and imaginary potentials. Broek et al (Br 65), in analyzing 43 MeV alpha elastic scattering over a wide angular range on ^{58}Ni, were able to describe the data more successfully by use of a six parameter model. Fulmer et al (Fu 68) observed similar improvement using a six parameter potential to describe 21 MeV elastic alpha scattering on targets of A=58-64. However, in the present analysis the more constrained four parameter model seemed appropriate as it was considered that the inherent energy dependence of the data would absorb and thus nullify the increased parameterization, masking any physical significance in the parameters. Lucas et al (Lu 66) in analyzing the wide angle elastic alpha scattering on ^{20}Ne at 18 MeV commented that the improvement in fit with six parameters was not commensurate with the increased number of parameters. Satchler (Sa 65) used a four parameter potential to describe the related 28 MeV data although this, it was commented, was appropriate in view of limited forward angle range of the data.

In the analysis of So et al (So 66) of the 8 to 19 MeV alpha elastic scattering on ^{24}Mg equivalent fits were obtained employing an imaginary potential with either the volume absorption radial form of equation (5-1) or the surface absorption radial form which is the derivative of the volume form. The same equivalence was found in the present analysis and a volume absorption term was used throughout.

5.3 Procedure of Analysis

The comparison of the predictions of the optical model with experiment was performed with the automatic search code JIB 3 written by F.G. Perey (see appendix V). In the code the criterion for determining the parameter values giving an optimum fit was the minimization of the quantity :

$$\chi^2 = \frac{1}{N} \sum_{i=1}^{N} \left(\frac{\sigma_{exp}(\Theta_i) - \sigma_{th}(\Theta_i)}{\Delta \sigma_{exp}(\Theta_i)} \right)^2 \qquad (5\text{-}6)$$

where (i) $\sigma_{exp}(\Theta_i)$ and $\sigma_{th}(\Theta_i)$ are the experimental and theoretical values of the differential cross section at the centre of mass scattering angle Θ_i;

(ii) $\Delta \sigma_{exp}(\Theta_i)$ is the relative error ascribed to the experimental value $\sigma_{exp}(\Theta_i)$; and

(iii) N is the number of data points in the given angular distribution.

In the process of minimization, the n dimensional χ^2 surface, defined by the n parameters used in the fit may be subject to undue distortion from contributions to χ^2 arising from data points which although experimentally well determined are rather poorly described by the optical model. To circumvent a minimization representative of an attempt to fit a few data points a balanced weighting procedure equating all relative percentage uncertainties of <4% to 4%, as is mentioned in section 3.5, was adopted. The usual practice is to equate all errors to 5% or 10% thus allowing comparison of the quality of fits; this was not feasible in the present analysis as the relatively large uncertainties arising from some finite geometry corrections at minima in the angular distributions could not be disregarded. A detailed description of the code was not available but it probably employs the method of minimization that is discussed by Melkanoff (Me 65) under the heading of the Oak Ridge and Oxford method.

The initial fitting was designed to provide an overall picture of the applicability of the analysis and to determine the presence or otherwise of the discrete ambiguities in the potential well depths associated with the scattering of composite particles such as alpha particles (Dr 63). The value of V was gridded from 20 to 230 MeV in steps of 5 MeV; the values r_0=1·8 and r_c=1·33 fermi which were found to be appropriate in preliminary analysis similar to that subsequently considered in section 5.5(i) and which were consistent with the closely related analyses of So et al (So 66) and Lucas et al (Lu 66) were held fixed and for each value of V a search was made varying W and a. The above values of r_0 and r_c were used for all procedures to be described in this section; the fits were very insensitive to the value of r_c as was indicated by a comparison of fits for r_c=1·33 and 1·80 fermi. The preliminary analysis had indicated that fits to the full angular range of data of several of the angular distributions were poor and for the purposes of this initial procedure some wide angle data were neglected. This procedure was applied to ten of the elastic scattering distributions of the present measurements including only one representative of the five measured from 12·217 to 12·404 namely that at the central energy of 12·307 MeV.

The results of this 2-parameter minimization of χ^2 are plotted in figure 5.1 and the angular range of data fitted is indicated for each distribution. Discrete minima as a function of V are evident and, for energies other than that of 12·70 MeV, are spaced at ≈20 MeV for shallow V with an increase to ≈40 MeV for deeper V. A relative comparison of χ^2 for each energy is not very meaningful because of the disparity of the relative errors.

Designating the above procedure as (i) and the derived sets of parameters yielding the discrete minima as

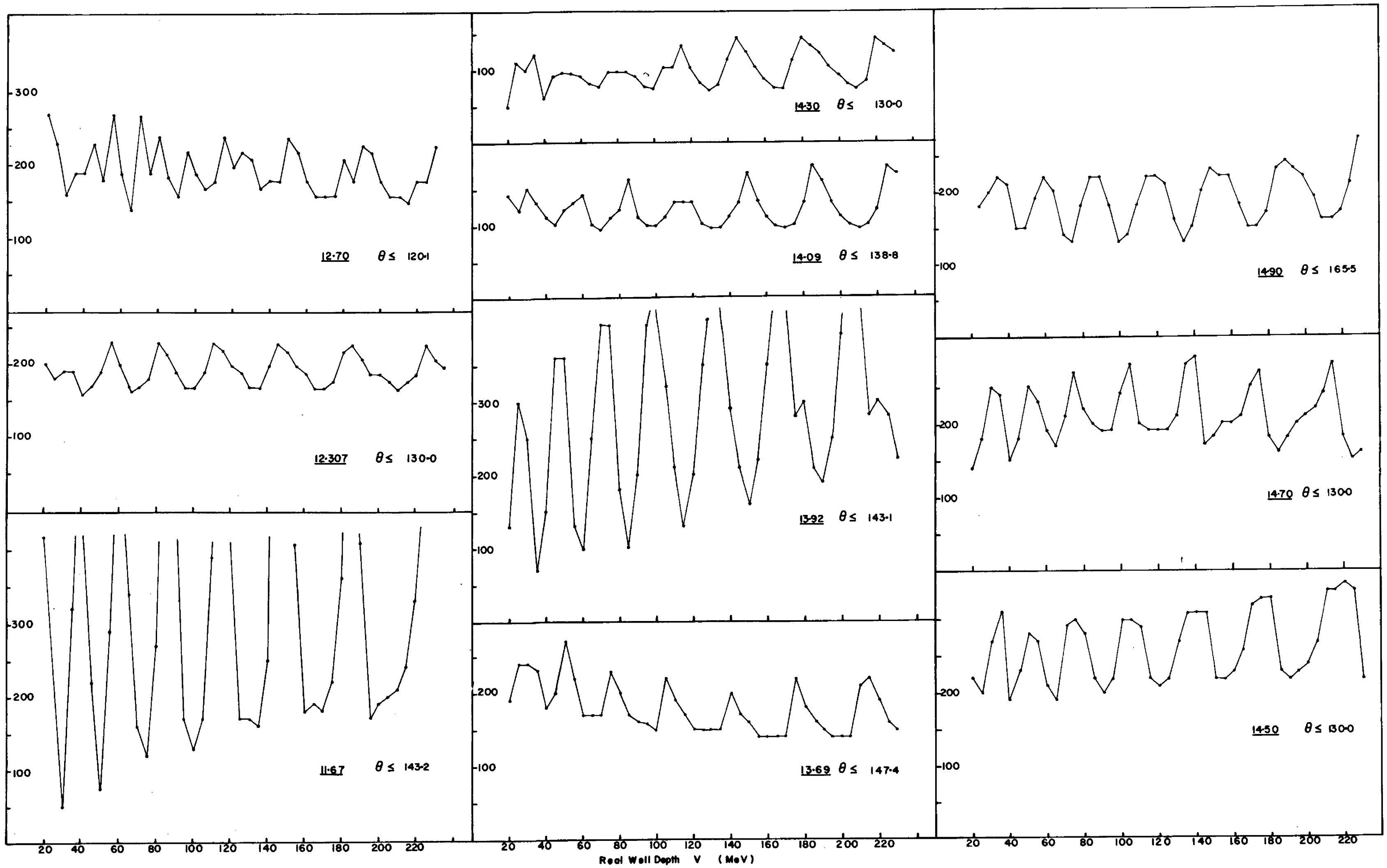

FIGURE 5.1 Plot of χ^2 as a function of the real well depth; the angular ranges of fitting are shown

$\{W,a\}_{(i)}$, subsequent fitting procedures are descirbed in the following and referred to as (ii), (iii), (iv) and (v).

(ii) With the sets of parameters $\{W,a\}_{(i)}$ as starting values 3-parameter minimizations were performed, over the same angular ranges of data as used in (i), by varying V, W and a with r_0=1·8 fermi. In addition, the parameters $\{W,a\}_{(i)}$ for the 12·307 MeV distribution were used as starting values in the same procedure applied to limited angular ranges of data for the other four distributions from 12·217 to 12·404 MeV. The values of V corresponding to the new χ^2 minima are plotted as a function of the alpha particle bombarding energy in figure 5.2 and the angular range of fitting is also indicated. The improvement in fits, in comparison to those of procedure (i) as was indicated by a slight decrease in χ^2, in most cases was slight.

(iii) The sets of parameters from procedure (ii) yielding χ^2 minima for each distribution at a value of V≈100 MeV were used as starting values in 3-parameter minimizations, each of which was applied to the full angular range of data, and for which V, W and a were varied with r_0=1·8 fermi. The best fit parameters thus obtained are referred to as $\{V,W,a\}_{(iii)}$ and are tabulated in table 5.1(a). An appraisal of the fits from procedures (ii) and (iii), over the angular ranges defined by the limited ranges of (ii), indicated that the quality of fits showed only slight

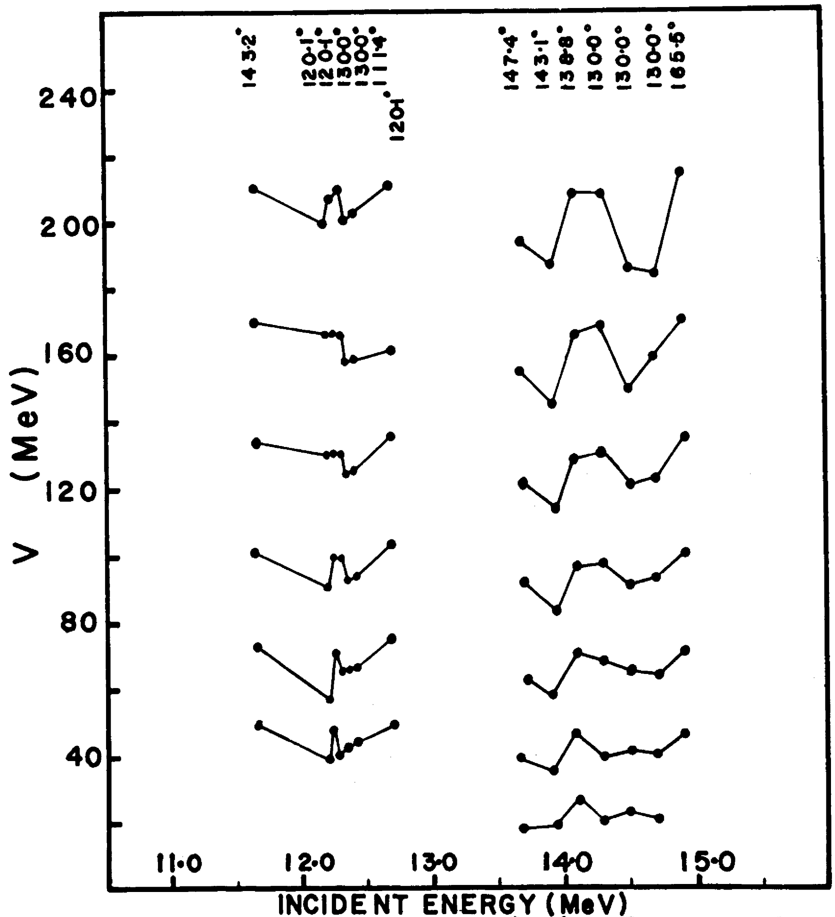

FIGURE 5.2 Optimum V of the 3-parameter minimizations applied to the angular ranges shown

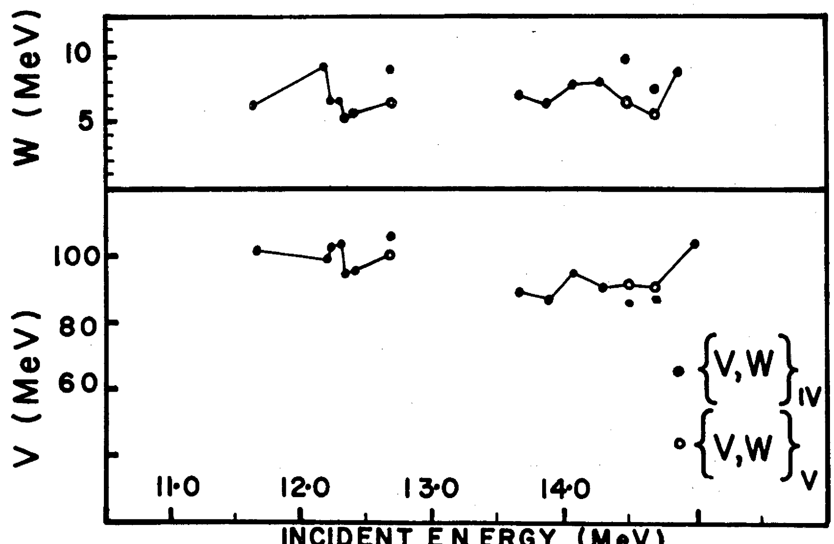

FIGURE 5.3 Optimum V of the 2-parameter minimizations corresponding to the parameters of table 5.1(b)

	TABLE 5.1(a)				TABLE 5.1(b)		
E MeV	r_0=1·8 fermi				r_0=1·8 fermi, a=0·53 fermi		
	V MeV	W MeV	a fermi	χ^2	V MeV	W MeV	χ^2
11·67	101·7	6·1	0·54	150	101·3	6·1	150
12·217	88·2	7·5	0·61	230	98·8	9·1	260
12·257	99·7	6·5	0·60	150	102·1	6·5	170
12·307	99·9	6·5	0·58	240	102·9	6·5	250
12·358	91·3	5·1	0·60	200	94·9	5·2	220
12·404	94·1	5·7	0·56	120	95·5	5·6	120
12·70	104·7	8·8	0·58	240	106·2 101·2*	9·0 6·3	250
13·69	90·7	6·9	0·49	140	88·1	7·0	150
13·92	84·4	6·2	0·59	110	86·7	6·2	140
14·09	97·6	8·0	0·51	150	95·6	7·7	150
14·30	100·6	12·9	0·38	83	91·6	8·0	100
14·50	91·7	9·4	0·46	240	85·8 90·9*	9·8 6·4	250
14·70	92·5	7·4	0·47	210	87·8 89·7*	7·4 5·5	220
14·90	101·9	8·4	0·60	130	104·0	8·7	130

* Denotes $\{V,W\}_{(v)}$ set;

see following.

deterioration upon the inclusion of the wider angle data.

(iv) An average value for the diffuseness of a=0·53 fermi was estimated from the sets $\{V,W,a\}_{(iii)}$ corresponding to seven energies for which the data was adjudged the best fitted. The values of a derived in the related analysis of So et al (So 66) and Lucas et al (Lu 66), were a=0·49 (averaged over nine energies) and a=0·55 fermi respectively. Taking then r_0=1·8 fermi, a=0·53 fermi and the values of V and W from $\{V,W,a\}_{(iii)}$ as starting parameters a 2-parameter χ^2 minimization varying V and W was applied to each distribution over the full angular range of data. The values of V and W obtained in this 2-parameter search are designated as $\{V,W\}_{(iv)}$ and are plotted in figure 5.3 as a function of the incident alpha energy and tabulated in table 5.1(b). The fits with the parameters $\{V,W\}_{(iv)}$, a=0·53 fermi and r_0=1·8 fermi for each energy are shown in figure 5.4. Again only slight deterioration in fit accompanied the additional constraint; the χ^2 values of tables 5.1(a) and 5.1(b) quantitatively indicate this.

(v) The quality of fits in figure 5.4 varies quite markedly as would be expected. The predictions of the model are in qualitative agreement with the data at 11·67, 12·404, 13·69, 13·92, 14·09, 14·30 and 14·90 MeV. The remaining fits are poor and this, to a certain extent, represents the inapplicability of the χ^2 criterion for data for which the optical model description appears less

<u>FIGURE 5.4</u>

Optical model fits (solid lines) to observed elastic alpha scattering on ^{20}Ne (dots) employing the parameters of table 5.1 (b); the dashed lines correspond to parameters $\{V,W\}_{(v)}$

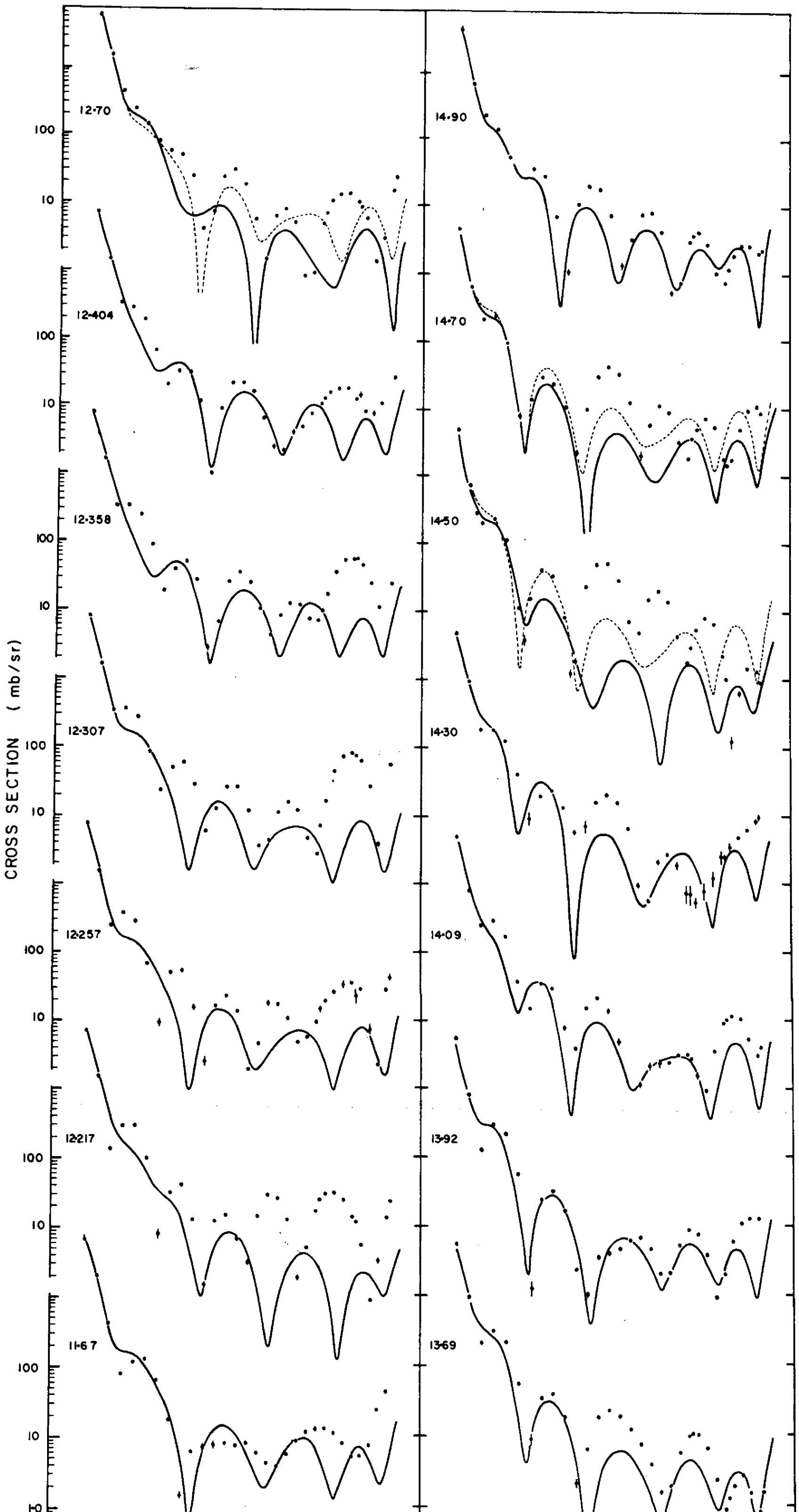

CROSS SECTION (mb/sr)
SCATTERING ANGLE
12·70
12·404
12·358
12·307
12·257
12·217
11·67
14·90
14·70
14·50
14·30
14·09
13·92
13·69
100
10
1·0
20
40
60
80
100
120
140
160

appropriate; this is best illustrated by the poor fit at 14·50 MeV where the contribution to χ^2 from the minima at 151·6^o has dominated the minimization procedure because of the small cross section and consequent small value of $\Delta\,\sigma_{exp}$ (Θi), in equation (5-6). Thompson et al (Th 67) noted that such a problem may arise and pointed out that in the minima many nuclear processes may be interfering, thus producing little scattering and a situation which would not be expected to be well described by the optical model. In an attempt to overcome this problem the poorly described 12·70, 14·50 and 14·70 MeV data were again fitted in a 2-parameter minimization varying V and W, using as starting values $\{V,W\}_{(iv)}$ with r_0=1·8 fermi and a=0·53 fermi and with 400% errors assigned to the data points of the backward angle minima. The resultant fits although out of phase at backward angles showed better agreement with the cross section magnitudes and improved agreement in shape in the forward hemisphere. The implied assumptions that the foremost agreement of the model and data will be apparent at forward angles and that the forward angle shapes for the 14·50 and 14·70 MeV data should be more satisfactorily described than is indicated in figure 5.4 for the parameters $\{V,W\}_{(iv)}$ appear valid. However a simpler and perhaps less subjective method is to fit only the forward angle data ($\Theta \leq 100^o$) and predict the full angular distributions with the derived parameters. As the two methods produced equivalent results the latter has been used to describe the data at 12·70, 14·50 and 14·70 MeV. These three additional fits are included in figure 5.4 and the parameters specified as $\{V,W\}_{(v)}$ are included in table 5.1(b) and plotted in figure 5.3. Attempts to improve the forward angle description of the other poorly described data at the energies 12·217 to 12·357 MeV did not yield significant improvement over the fits already obtained in fitting the full angular range.

5.4 Discussion of the Analysis

The χ^2 minima obtained in the initial grid search of procedure (i) illustrate the well known ambiguity in the real well depth, an effect which is rather pronounced in describing the scattering of complex projectiles such as alpha particles (Sc 65). It is not surprising that this systematic persists even for poorly fitted data as the fits show the characteristic diffractive structure. The source of such ambiguities has been described by Drisko et al (Dr 63) in terms of the equivalence of the scattering matrix elements corresponding to the various potentials; it was found that successive acceptable potentials corresponded to an additional half-wavelength in the radial wave functions for almost all contributing partial waves and that assymptotically the radial wave functions for corresponding partial waves of each potential were equivalent in phase and magnitude. Thompson et al (Th 67) in describing the elastic scattering of 10·8 MeV alpha particles on ^{24}Mg illustrated both the assymptotic equivalence of the radial wave functions corresponding to the discrete ambiguities in the well depth and the addition of an extra half-wavelength within the potential well for each successive increase in V.

The near equivalence of the scattering matrix elements for each discrete increment in V obtained in the analysis of the 14·90 MeV data is indicated in table 5.2. For the purposes of this table the values of V and W from the discrete sets of parameters for the 14·90 MeV data as obtained in procedure (ii) were used as starting values, with r_0=1·8 fermi and a=0·53 fermi, in a 2-parameter search that was applied to the full angular range of the 14·90 MeV data and in which V and W were varied.

The values of table 5.2 indicate a trend within the range of V shown but the equivalence of the potentials can be seen to be an equivalence of the S_ℓ of equation (5-5). A minimum in χ^2 for the parameters of the above table corresponds to V=100 MeV but as discussed in section 5.5(i) this is a function of r_0. The choice of V=100 MeV for obtaining the final fits shown in figure 5.4 was made on the basis of the systematics which are discussed in section 5.5(i) and which were apparent in preliminary analysis.

The derived potential strengths show, as seen in figures 5.2 and 5.3, fluctuations in both the ranges of energies presently considered and indicate the anticipated parameterization of the cross section energy dependence. The analysis of Aldridge et al (Al 68) of the elastic alpha

TABLE 5.2*

	V 51·7	W 6·2	V 76·3	W 7·6	V 104·0	W 8·7	V 135·4	W 9·3	V 170·7	W 11·0	V 210·0	W 12·4
ℓ	η_ℓ	δ_ℓ	η_ℓ	δ_ℓ	η_ℓ	δ_ℓ	η_ℓ	δ_ℓ	η_ℓ	δ_ℓ	η_ℓ	δ_ℓ
0	·19	-21	·19	-19	·18	-24	·19	-29	·18	-33	·17	-37
1	·14	85	·14	101	·14	98	·15	93	·15	90	·14	86
2	·21	46	·20	45	·19	40	·19	34	·19	29	·17	25
3	·13	91	·14	11	·15	5	·15	- 1	·15	- 6	·14	-10
4	·23	133	·21	129	·20	123	·20	116	·20	111	·18	106
5	·20	114	·19	108	·18	99	·17	90	·17	83	·16	88
6	·26	12	·23	7	·23	3	·23	- 3	·23	- 8	·22	-12
7	·53	- 2	·45	- 7	·38	-13	·33	-19	·29	-24	·26	-29
8	·69	10	·61	12	·56	12	·53	12	·50	12	·47	11
9	·96	3	·92	4	·87	4	·81	4	·74	4	·68	3
10	·99	1	·98	2	·98	2	·97	3	·96	3	·94	4
χ^2	180		150		130		130		150		160	

* V and W are in MeV; and δ_ℓ are given in degrees.

scattering on ^{32}S clearly defined fluctuations in V about a constant real well depth $\bar{V}$ and in W about a linearly increasing imaginary well depth $\bar{W}$. The present data is too limited to define such average trends although in the two ranges of measurement the fluctuations shown in figure 5.3 can be regarded as centred around constant values. The average real and imaginary strengths describing the presently observed scattering as derived from table 5.1(b) are :

$$\bar{V} = 96 \quad (\pm 6) \quad \text{MeV}$$

and $$\bar{W} = 6{\cdot}7 \quad (\pm 1{\cdot}3) \text{ MeV}$$

where the bracketed values indicate the mean square deviation over the fourteen sets of parameters and where, in taking the averages, the parameters $\{V,W\}_{(v)}$ were considered for the energies of 12·70, 14·50 and 14·70 MeV. A comparable discrete potential in the analysis of Aldridge et al (Al 68) was $\bar{V}$=103 MeV with $\bar{W}$ increasing from 4 to 6·7 MeV over the equivalent alpha energy range of 12 to 15 MeV.

The energies for which the optical model predictions are in reasonable qualitative agreement with the data are those which appear less influenced by energy dependent structure. The two energies of 13·92 and 14·90 MeV for which the qualitative fits are perhaps the most satisfactory correspond to minima on either side of the broad structure seen in the excitation function for elastic scattering at 91·4° (c.mass) in figure 4.1(c). Movement away from each of these energies towards the broad adjacent structure is accompanied by deterioration in fit.

In summarizing this discussion it is considered that:

(i) the qualitative applicability of the optical model in describing approximately half of the number of measured elastic scattering angular distributions is indicative of the presence of a significant contribution from direct scattering to the total elastic scattering amplitude; and

(ii) although showing sharp energy dependence the parameters V and W indicate average values such as would be demanded by an optical model description of direct scattering which is unperturbed by resonance effects.

5.5 Systematics in Discrete Ambiguities in V

(i) In view of the fixed value of r_0=1·8 fermi used in the analysis described hitherto, the effect of varying r_0 is indicated in the present discussion.

A two-dimensional grid was defined by V=20 to 240 MeV (ΔV=5 MeV) and r_0=1·7, 1·8 and 1·9 fermi and for each grid point a 2-parameter search varying W and a was applied to the 14·90 MeV data for $\theta \leq 111^\circ$. A subsequent 3-parameter search varying V,W and a defined the χ^2 minima thus indicated more exactly. The results of this procedure are indicated in figure 5.5 where χ^2 as a function of V for each value of r_0 is plotted; the quality of the fits at the minima is equivalent to that subsequently shown in figure 5.6 for $\theta \leq 111^{\circ}$. A systematic shift towards higher V accompanies the decrease in r_0 at each minima; this is in close accord with the well known $Vr_0{}^n$ valley ambiguity which has been discussed by Hodgson (Ho[1]66). The value of n=1·5 satisfies the invariance condition to within 2% for each discrete valley in the V-r_0-χ^2 surface. The W and a associated with each minima are not plotted but were seen to be determined by r_0 and to be functions of increasing V, with W increasing and a decreasing.

The extent to which the value of r_0 determines the quality of the fit is indicated by the envelope defined by the χ^2 minima. With decreasing r_0 the minimum of the envelope moves towards large V and for each r_0 there are equivalent fits. The choice of r_0=1·8 fermi for the analysis discussed in section 5.3 appears to remove an ambiguity rather than impose a constraint. In the analysis, by Aldridge et al (Al 68) of elastic alpha scattering on ^{32}S, a bias for V≈100 MeV was considered as possibly an effect of fixed geometrical parameters of r_0=1·64 fermi and a=0·56 fermi.

The present analysis exhibits a bias for V which is a function of r_0 and, as is indicated in figure 5.5, r_0=1·8 fermi determines the preference for V≈100 MeV. It is thus suggested that the related bias in the analysis of Aldridge et al is similarly a reflection of the fixed radius

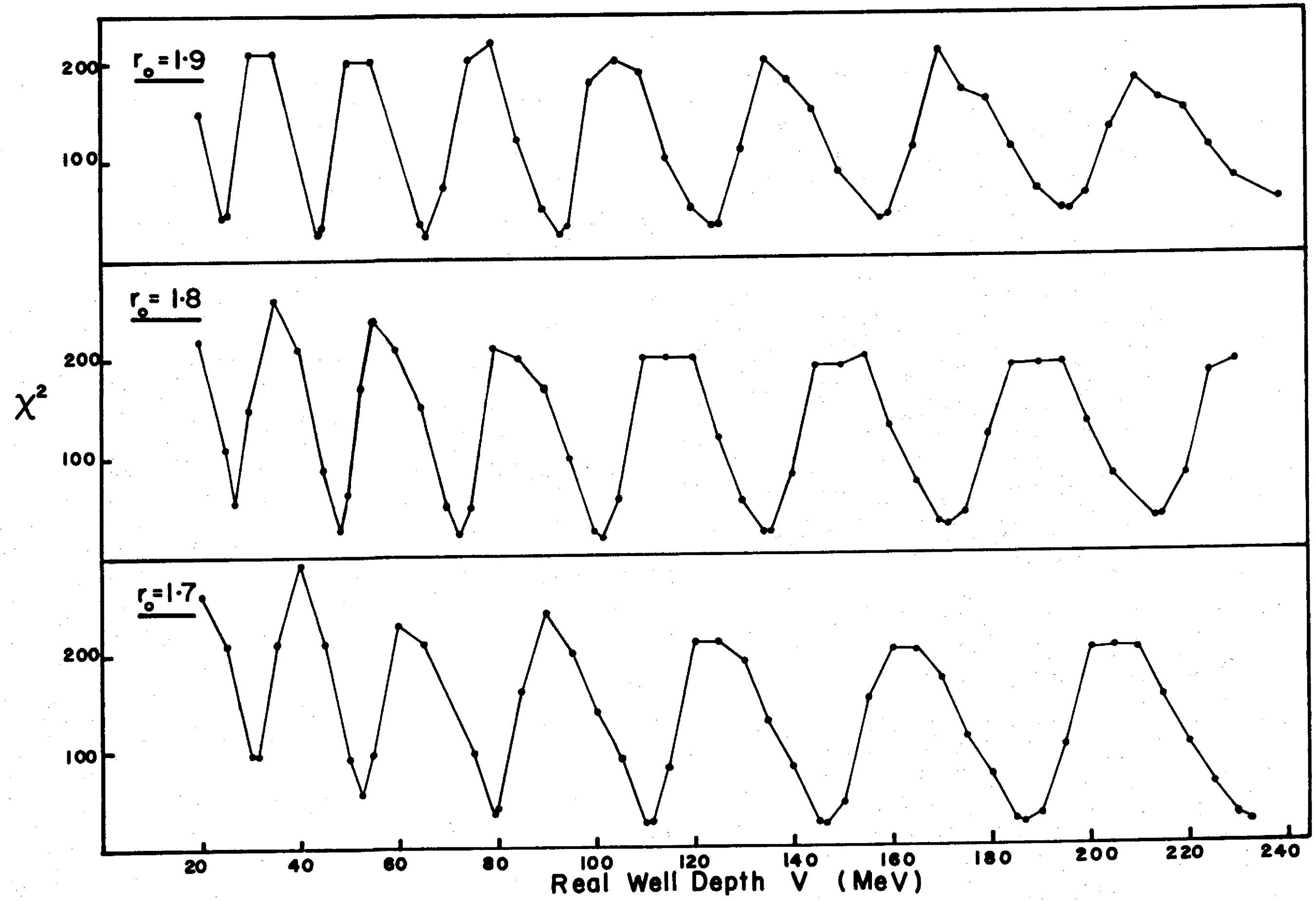

FIGURE 5.5 Plot of χ^2 minima for the 14·90 MeV data ($\theta \leq 111^{\circ}$) as a function of V for fixed values of r_0

parameter.

(ii) The derived optical model parameters corresponding to the discrete ambiguities can indicate the importance of the surface potential in defining the scattering. Igo (Ig 59) proposed that the scattering of strongly absorbed particles such as alpha particles is sensitive only to the tail of the potential, and the Woods-Saxon radial form factor in the region $r \approx R_0$ rewritten as :

$$U(r) \sim -(V+iW)\ e^{R_0/a}\ e^{-r/a} \qquad (5\text{-}7)$$

implies the invariance conditions :

$$V\ e^{R_0/a} = \text{Const} = C_1 \qquad (5\text{-}8)$$

$$W\ e^{R_0/a} = \text{Const} = C_2 \qquad (5\text{-}9)$$

These invariance conditions imply a continuous ambiguity but, as Drisko et al (Dr 63) have pointed out, in order to satisfy the requirements of matching of the external and internal wave functions the need for a discrete spectrum of potentials is consequently superimposed.

The importance of the surface potential in defining the scattering is thus indicated by the degree to which the invariance conditions are satisfied. In considering the applicability or otherwise of these details to the present analysis, in particular to the data at 14·90 MeV, further optical model fitting was performed. With a = constant the invariance conditions reduce to :

(i) $\log V \propto r_0$

(ii) $\log W \propto r_0$

and so with a = constant, 3-parameter searches varying V,W and r_0 were applied to the 14·90 MeV elastic scattering data. This procedure was applied to the data for three fixed values of a=0·45, 0·50 and 0·55 fermi and for each of these over angular ranges defined by $\theta \leq 111^{\circ}$, 143° and 165°. A diagramatic representation of the results is shown in figure 5.7; V and W are plotted against r_0 on a semi-logarithmic scale for each value of a and each angular range. Corresponding values of χ^2 are plotted as functions of r_0 on a linear scale. The quality of fits accompanying each angular range is indicated in figure 5.6 for V≈95 MeV.

An approximate linear relationship is indicated in figure 5.7 for log V and log W as functions of r_0. With the inclusion of wider angles and with decreasing a the relationship deteriorates. The approximate nature of the dependence indicated graphically, is more apparent in table 5.3 where for $\theta \leq 111^{\circ}$ and for each value of a the C_1 and C_2 of equations (5-8) and (5-9) are given.

A variation of C_1 and C_2 over the range of discrete a values is expected in view of the $e^{-r/a}$ dependence of equation (5-7); the source of a factor of ≈4 difference with each successive variation of a is however not obvious to the author. This rather pronounced sensitivity to a explains the lack of even approximate invariance in the parameters derived

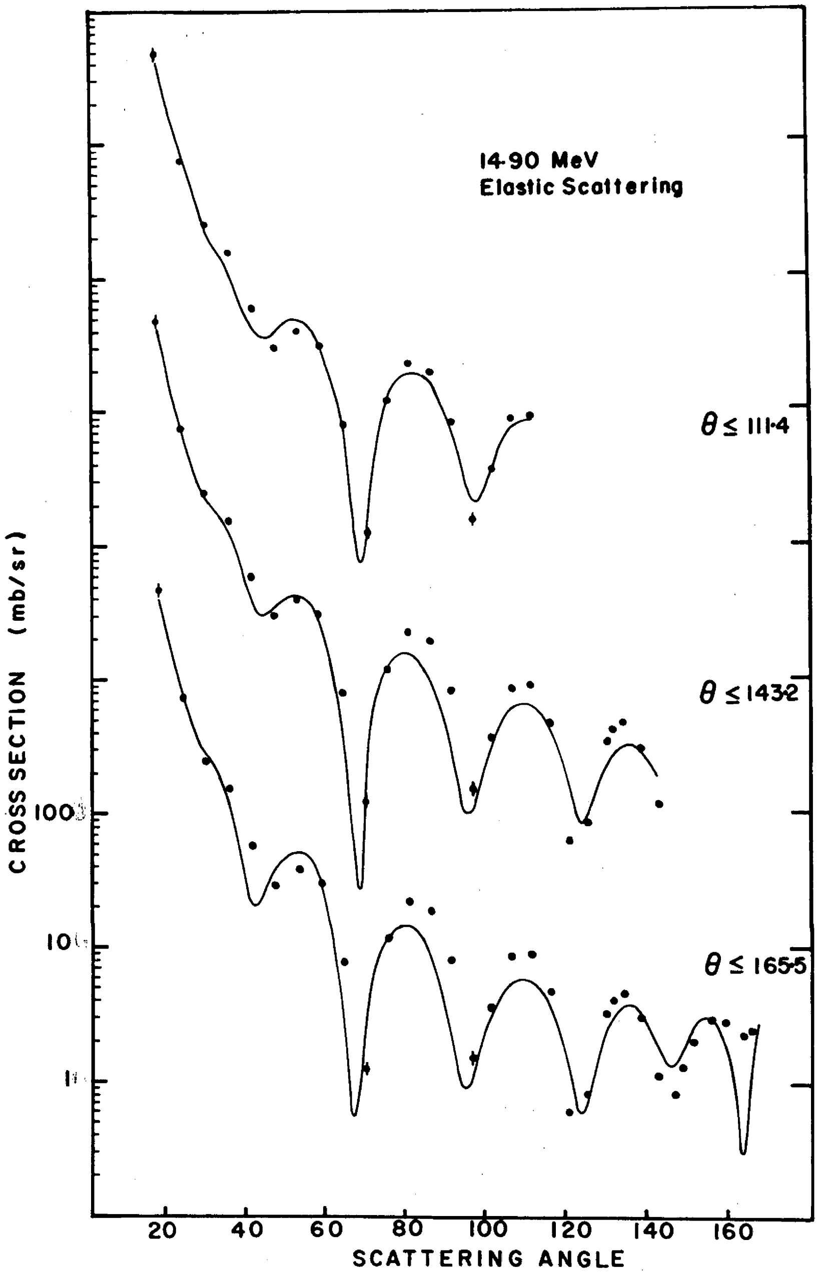

FIGURE 5.6 Optical model fits (solid lines) to the three angular ranges of 14·90 MeV elastic alpha scattering on ^{20}Ne (dots)

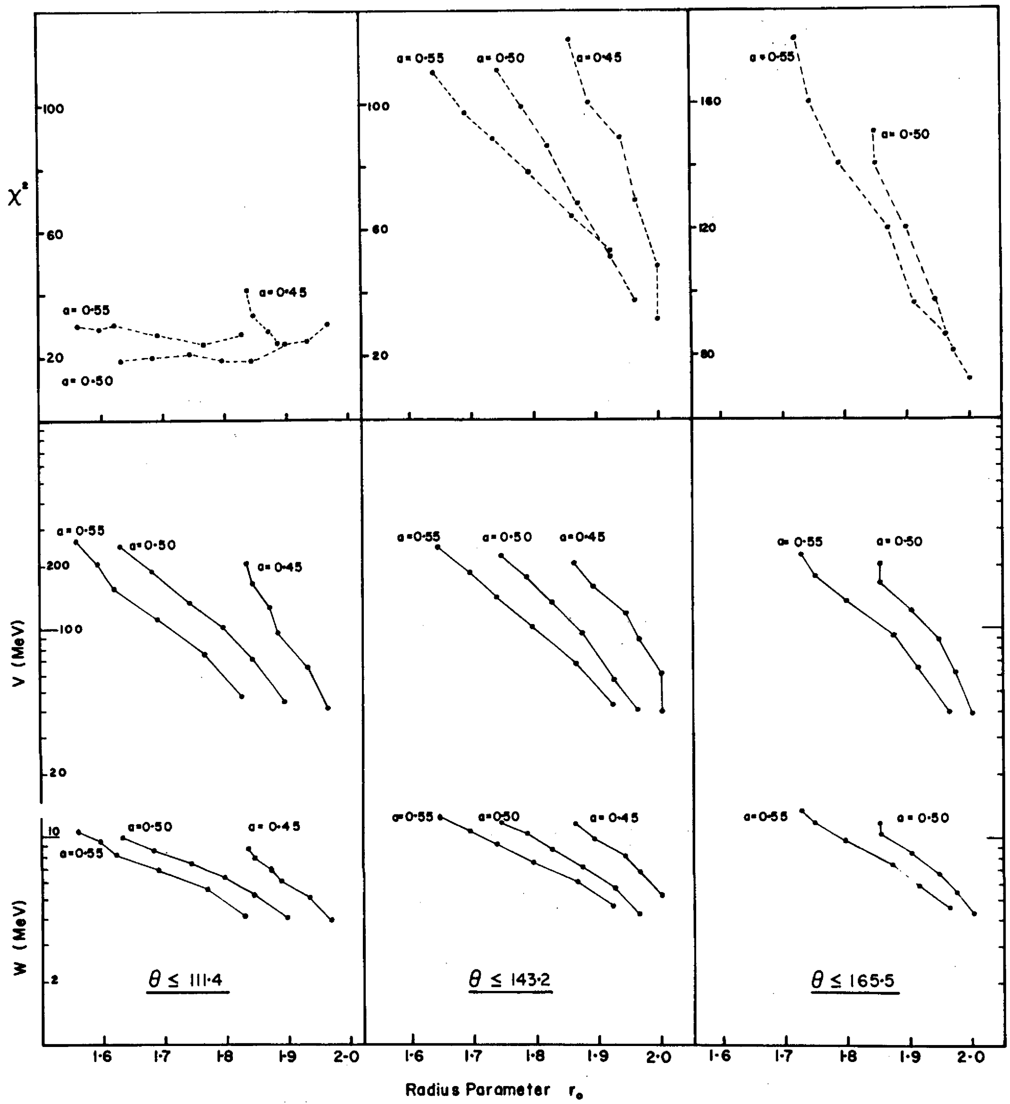

FIGURE 5.7 Plot of V,W and χ^2 as a function of r_0 obtained for fixed values of a in fitting three angular ranges of the 14·90 MeV elastic scattering

TABLE 5.3

a=0·55 fermi		a=0·50 fermi		a=0·45 fermi	
C_1 $\times 10^{-5}$	C_2 $\times 10^{-4}$	C_1 $\times 10^{-5}$	C_2 $\times 10^{-4}$	C_1 $\times 10^{-5}$	C_2 $\times 10^{-4}$
3·9	3·6	13·3	12·2	59·8	57·3
4·6	3·5	15·5	11·6	76·2	59·3
4·7	2·9	17·5	10·9	82·3	52·3
4·7	2·4	18·1	9·5	101·1	55·2
5·4	2·5	17·7	8·0	126·4	61·0
5·8	2·4	17·3	7·0	133·5	57·0

in some preliminary 4-parameter searches in which, in addition, a was allowed to vary freely. It seems then in anticipating a = constant that the invariance conditions of Igo are approximately satisfied and that the surface potential is dominant in defining the scattering.

It is seen in figure 5.7 that the inclusion of wider angles in the fitting procedure introduces a pronounced bias towards smaller V and larger r_0 for optimum fit; this bias is also apparent within each ambiguity as is indicated by the left to right shift of the V,W plots as a function of increasing angular range. It would seem that a preference for low V is a function of the light mass of the target; McFadden et al (Mc 66) found in 4-parameter optical model analysis of 24 MeV alpha scattering on a wide range of targets that the χ^2 minimum for scattering from light nuclei, e.g. ^{24}Mg, corresponded to the lowest discrete V.

CHAPTER 6

Extended Optical Model Analysis of Elastic and Inelastic Scattering

The extension of the optical model to include an explicit treatment of inelastic scattering is considered in this chapter. Comparisons of the predictions of the model with the 0^+-2^+-4^+ scattering at six of the energies of the present measurements are made.

6.1 Formulation of the Extended Optical Model

The generalization of the optical model to provide explicit treatment of inelastic scattering, described as the extended optical model, was discussed in detail in the review paper of Tamura (Ta 65) and the lecture series of Glendenning (Gl 67). This approach is of particular relevance for describing scattering from strongly deformed or deformable nuclei, the low lying states of which correspond to simple types of excitation interpreted in terms of collective behaviour. Deformed nuclei characteristically exhibit, among their low lying levels, rotational bands, each of which corresponds to the rotational spectrum of an intrinsic nuclear state. In scattering from such nuclei the rotational motion, corresponding to excitation via rotation of the deformed ground state nucleus, can be strongly coupled to the motion of the scattered particle and a simple direct process of inelastic excitation is thus possible (Ch 58). Excitation of vibrational bands of a deformable nucleus can be similarly described but will not be considered in the present discussion.

The extension of the optical model is to assume the shape of the potential follows that of the nucleus; this requires the inclusion of non-spherical terms in representing the potential of a deformed nucleus and permits then an explicit treatment of inelastic scattering with excitation of collective states. The ensuing discussion aims to illustrate details of the framework within which some extended optical model calculations have been performed. The computer code used for these calculations was written by T. Tamura and the subsequent mathematical formalism closely follows his review article (Ta 65).

In the rotational model of Bohr and Mottleson (Bo 53) it is assumed that the nucleus has permanent deformation with cylindrical symmetry and the nuclear surface can be described as :

$$R(\theta',\phi') = R_0\left[1 + \sum_{\ell}\beta_\ell Y_{\ell o}(\theta',\phi')\right] \qquad (6\text{-}1)$$

where (i) the summation is restricted to even ℓ values for a plane reflectionally invariant shape, i.e. $R(\theta',\phi') = R(\pi - \theta',\phi' + \pi)$;

(ii) R_0 is the radius of the undeformed nuclear surface;

(iii) β_ℓ is a measure of the ℓ^{th} order deformation; and

(iv) $Y_{\ell o}(\theta',\phi')$ are spherical harmonics referred to the body fixed axes.

With expression (6-1) defining the radial dependence of the optical potential, equation (5-1) is rewritten and defines the non-spherical potential :

$$U(r,\theta',\phi') = -(V+iW)\frac{1}{1+e^{\frac{r-R(\theta',\phi')}{a}}} + V_c(r,\theta',\phi') \tag{6-2}$$

An expansion of both nuclear and coulomb terms of equation (6-2) up to second order in $\left[\sum_\ell \beta_\ell Y_{\ell o}(\theta',\phi')\right]$, with $Y_{\ell o}(\theta',\phi')$ subsequently replaced by the space fixed axes term $\sum_m D^\ell_{mo}(\theta_i)Y_{\ell m}(\theta,\phi)$ yields :

$$\begin{aligned} U(r,\theta,\phi) = & \left[-(V+iW)\frac{1}{1+e'} + V_{c_0}(r)\right] \\ & + \left[-(V+iW)\frac{R_0}{a}\,\frac{e'}{(1+e')^2} + V_{c_1}(r)\right] \cdot \sum_{\ell m}\beta_\ell D^\ell_{mo}(\theta_i)Y_{\ell m}(\theta,\phi) \\ & + \left[(V+iW)\frac{R_0{}^2}{2a^2}\cdot\frac{e'(1-e')}{(1+e')^3} + V_{c_2}(r)\right] \\ & \cdot \sum_{\ell_1\ell_2\ell m}\left[\frac{\hat{\ell}_1\;\hat{\ell}_2}{4\pi\;\hat{\ell}}\right]^{\frac{1}{2}}(\ell_1\ell_2 oo|\ell o)^2\,\beta_{\ell_1}\beta_{\ell_2}D^\ell_{mo}(\theta_i)Y_{\ell m}(\theta,\phi) \end{aligned} \tag{6-3}$$

where (i) (θ,ϕ) refer to space fixed axes;

(ii) $D^\ell_{mo}(\theta_i)$ is the rotation matrix of the transformation from body to space fixed axes through Euler angles θ_i ;

(iii) $e` = \frac{1}{1+e^{\frac{r-R_0}{a}}}$

(iv) $\hat{\ell} = (2\ell+1)$; $(\ell_1\ell_2 oo|\ell o)$ is a Clebsch-Gordan coefficient; and

(v) $V_{c_0}(r)$, $V_{c_1}(r)$ and $V_{c_2}(r)$ are coulomb potential terms given in detail by Tamura in equations 12, 13.1 and 13.2 of (Ta 65).

In expression (6-3) the first term corresponds to the spherical optical potential, as in equation (5-1), while the additional non-spherical terms correspond to interaction potentials which give rise to excitations from one rotational state to another. Substitution of $U(r,\Theta,\phi)$ in the Schroedinger wave equation yields then, as shown in detail by Tamura, a series of differential equations in which the radial wave functions for a number of partial waves describing scattering from each rotational state are coupled. In considering scattering of a spin zero projectile and the excitation of states which belong to a ground state rotational band of spin sequence $0^+-2^+-4^+...$, the ℓ^{th} term of either of the deformed interaction potentials in expression (6-3) corresponds to direct excitation of a state of spin ℓ; the same state can also be excited by a multiple step excitation, for example via two successive interactions proportional to the ℓ_1 and ℓ_2 components of the second term of equation (6-3) and such that $\underset{\sim}{\ell}_1+\underset{\sim}{\ell}_2=\underset{\sim}{\ell}$.

The number of coupled equations that occurs is a function of the number and spin of the states explicitly considered. In the channel defined by the n^{th} explicitly considered state, of spin I_n and parity π_n, there will be a range of partial waves whose angular momentum ℓ_n satisfy the conditions :

$$\begin{aligned} \underset{\sim}{J} &= \underset{\sim}{\ell}_n + \underset{\sim}{I}_n \\ \Pi &= \pi_n(-)^{\ell_n} \end{aligned} \tag{6-4}$$

where J and Π specify the spin and parity of the total system.

In particular for spin zero on spin zero scattering and corresponding to each I_n there will be (I_n+1) partial waves satisfying expressions (6-4). Thus for each J^Π, $\sum_n(I_n+1)$ partial waves are permissible and a set of $\sum_n(I_n+1)$ coupled second order differential equations therefore ensues. (For a value of $I_n<J$ the number of partial waves satisfying (6-4) is actually less than (I_n+1)). In contrast to the single numerical integration associated with the radial wave function of equation (5-3) it is now necessary to perform simultaneous integration of the radial wave functions of $\sum_n(I_n+1)$ partial waves for each J^Π in order to extract the scattering matrix elements. The numerical method employed in solving the coupled equations is described by Tamura (Ta 67).

It is not surprising that until the advent of fast computers, scattering by a potential of the form of equation (6-3) was treated only to first order in the coupling interaction of $U(r,\theta,\phi)$ implying then zero coupling in the ground state channel. This method corresponds to the distorted wave Born approximation (DWBA) which is normally considered for the interaction expanded to first order in the deformation, i.e. up to the second term of equation (6-3) (Au 62). To facilitate a comparison of DWBA and coupled channel calculations, some transitions appropriate to a potential of the form of equation (6-3) are illustrated in figure 6.1 for a 0^+-2^+-4^+ rotational band with intrinsic deformation described by the $\ell=2$ and 4 terms of equation (6-1). The representation in the figure is similar to that of Blair (Bl 65); the single and dashed lines represent interactions which are proportional to the deformation in first order and the double lines represent interactions proportional to the deformation in second order. The three segments of the figure define interactions proportional respectively to :

(i) $\sum_m \beta_\ell D^\ell_{mo}(\Theta_i) Y_{\ell m}(\theta,\phi)$ for $\ell=2$ or 4 ;

(ii) Successive application of either of the two terms in (i); the dashed lines represent an alternative between $\ell=2$ and $\ell=4$ terms;

(iii) $\sum_{\ell_1\ell_2 m} \left(\frac{\hat{\ell}_1\ \hat{\ell}_2}{4\pi\ \hat{\ell}}\right)^{\frac{1}{2}} (\ell_1\ell_2 oo|\ell o)^2 \beta_{\ell_1}\beta_{\ell_2} D^\ell_{mo}(\Theta_i)$

for $\underset{\sim}{\ell_1} + \underset{\sim}{\ell_2} = 0,2$ or 4

where ℓ_1 and ℓ_2 may be either 2 or 4.

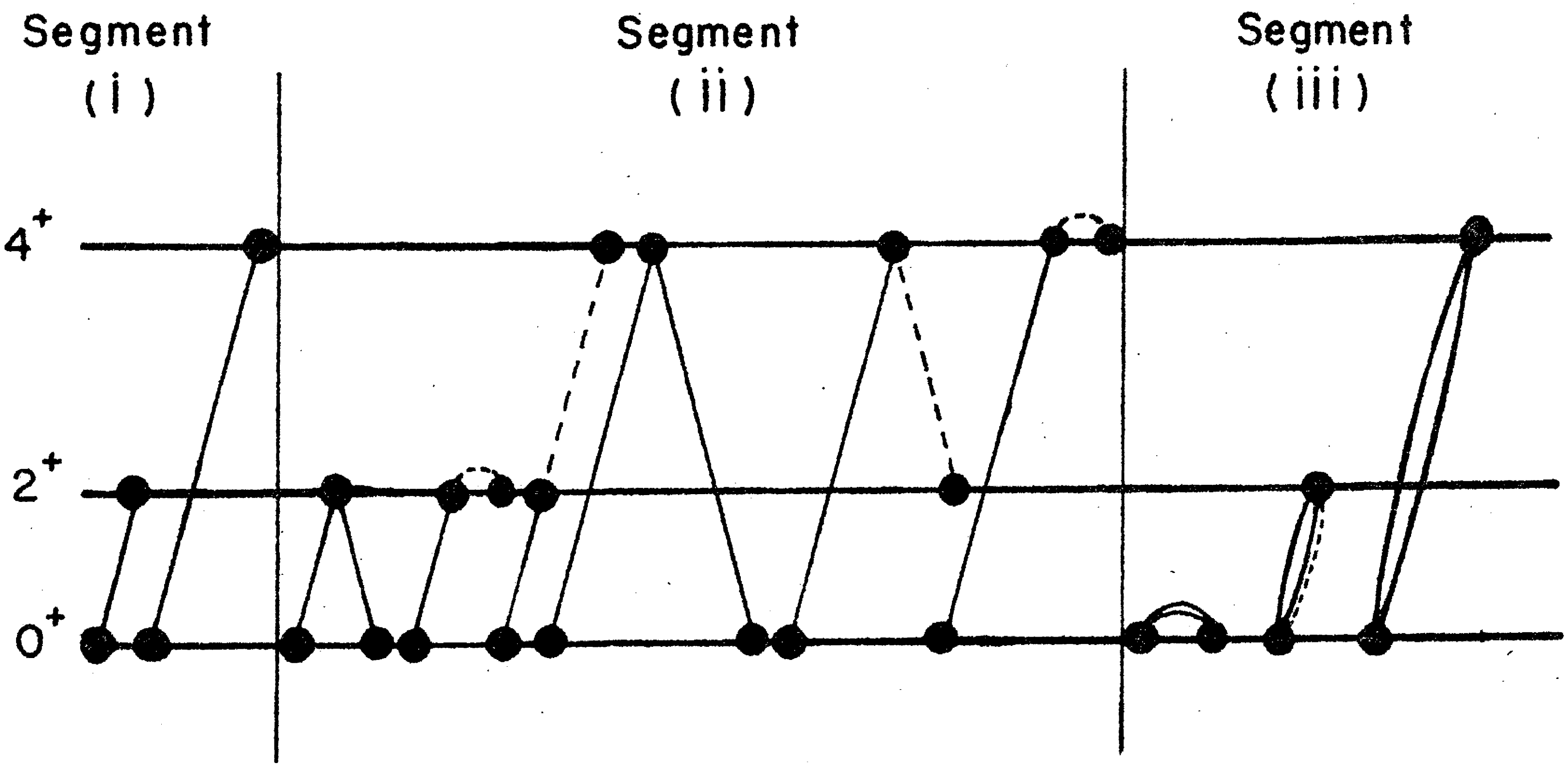

FIGURE 6.1 Schematic representation of interactions described by a potential of the form of equation (6-3) - sec page 83.

The strengths of the single step transitions of segment (i) which are proportional to β_2 and β_4 determine the strengths of multiple transitions (two-step) of segment (ii), proportional to β_2^2, β_4^2 and $\beta_2\beta_4$, and the strengths of the second order single step transitions of segment (iii), also proportional to β_2^2, β_4^2 and $\beta_2\beta_4$. As the first order DWBA neglects the effects of the interactions of segments (ii) and (iii) it is seen that it should only be appropriate for describing scattering from nuclei with small deformation.

Buck et al (Bu 63), in considering the two-state coupled channel calculations of the scattering of 14 MeV protons from both ^{20}Ne and ^{48}Ti, found that the total inelastic 2^+ scattering cross section did not increase with the β_2^2 dependence implicit in DWBA but increased more slowly with an approximate linear dependence on β_2 for values of $\beta_2 > 0{\cdot}2$; these authors employed the same potential parameters in both the DWBA and coupled channels calculations. Perey et al (Pe 63) however showed that the DWBA can give equivalent fits and estimates of quadrupole deformations providing the optical potentials employed to generate the distorted waves are those which describe the observed elastic scattering, i.e. that occurring in the presence of strong coupling. This result could be expected to be less appropriate with increasing deformation and stronger coupling to higher excited states via interactions other than those in segment (i) of figure 6.1. Perey et al showed the equivalence between the two methods for $\beta_2 \lesssim 0 \cdot 4$ but this was only for a two state calculation and it is not obvious that this equivalence still holds if the coupling of additional states, which is more realistic, is considered. To provide then a more rigorous description of the scattering it is preferable to consider a coupled channel calculation and thereby take accurate account of the interactions of segments (ii) and (iii) of figure 6.1. To describe the higher order interactions of segments (ii) and (iii) in the framework of DWBA it is necessary to consider the second order distorted wave theory which is however as complicated if not more so than a coupled channel calculation (Au 65).

A coupled channel calculation employing a potential of the form of equation (6-3) to describe the scattering appropriate to figure 6.1 would incorporate any multiplicity of the steps within segments (ii) and (iii). With many strongly deformed nuclei the power series expansion of the potential as in equation (6-3) becomes inappropriate even within the coupled channels framework. This arises because for example a multiple three step process can be described although a direct process via an interaction which is expressed to third order in the deformation is neglected; Blair (Bl 65) illustrates this difficulty in a diagram similar to that of figure 6.1. An alternative expansion of the potential $U(r,\theta,\phi)$ which is more satisfactory than that of expression (6-3) is that referred to as the Legendre expansion. The equivalent expansion as used by Tamura (Ta 65) is :

$$U(r,\theta',\phi') = \sum_{\ell} v^{\ell}(r) Y_{\ell o}(\theta',\phi') \qquad (6\text{-}5)$$

which in the space fixed axes becomes :

$$U(r,\theta,\phi) = \sum_{\ell m} v^{\ell}(r) D^{\ell}_{mo}(\theta_i) Y_{\ell m}(\theta,\phi) \qquad (6\text{-}6)$$

The orthonormality condition of the spherical harmonics yields :

$$v^{\ell}(r) = 4\pi \int_{o}^{1} \frac{-(V+iW)Y_{\ell o}(\theta',\phi')d(\cos\theta')}{1+e^{\left[\frac{r-R_0\left[1+\sum_{\ell'}\beta_{\ell'}Y_{\ell' o}(\theta',\phi')\right]}{a}\right]}} \qquad (6\text{-}7)$$

In describing proton elastic and inelastic scattering Tamura illustrated that the results of the power series and Legendre expansions have diverged for $\beta_2 \approx 0{\cdot}3$ and suggested that the latter expansion becomes the more appropriate for deformations in excess of this value. The advantage of employing the Legendre expansion of the nuclear interaction is that each $v^{\ell}(r)$ contains contributions from terms arising in the power series expansion considered to infinite order. Tamura has not applied the Legendre expansion to the coulomb potential $V_c(r,\theta',\phi')$ of expression (6-2) since it was considered to be adequately described by the power series expansion (Ta 65).

In expression (6-6) $v^{o}(r)$ corresponds to the spherical optical potential although it is not equivalent to that of the first term of equation (6-3) as it includes the elastic scattering processes such as in segment (iii) of figure 6.1. The term $v^{\ell}(r)$ corresponds to a single direct excitation with transfer of ℓ units of angular momenta while successive application of $v^{\ell}(r)$ is implicit in the channel coupling. It is to be noted that a calculation of elastic scattering even in the absence of coupling to excited states is affected by the deformations β_{ℓ}' of equation (6-7).

It is with reference to the above discussion that the description of the present analysis is given in section 6.4.

6.2 Nature of Target Nucleus ^{20}Ne

The target of the present measurements ^{20}Ne, together with other nuclei in the 2s-1d shell, e.g. ^{24}Mg, ^{25}Mg and ^{25}Al, have been shown by the Chalk River group to have well developed rotational band spectra (Go 60, Li 61, Li 65). An indication of the rotational excitations in ^{20}Ne is shown in figure 6.2 which is as given by Gove (Go 65); the energy level spectrum is seen to display bands defined in analogy to the energy levels of a rigid rotator by the expression (Pa 65) :

$$E_I(K) = E(K) + \frac{\hbar^2}{2\xi} I(I+1) \qquad (6\text{-}8)$$

where (i) I is the spin of the state of energy of excitation $E_I(K)$;

(ii) E(K) is a constant for each band

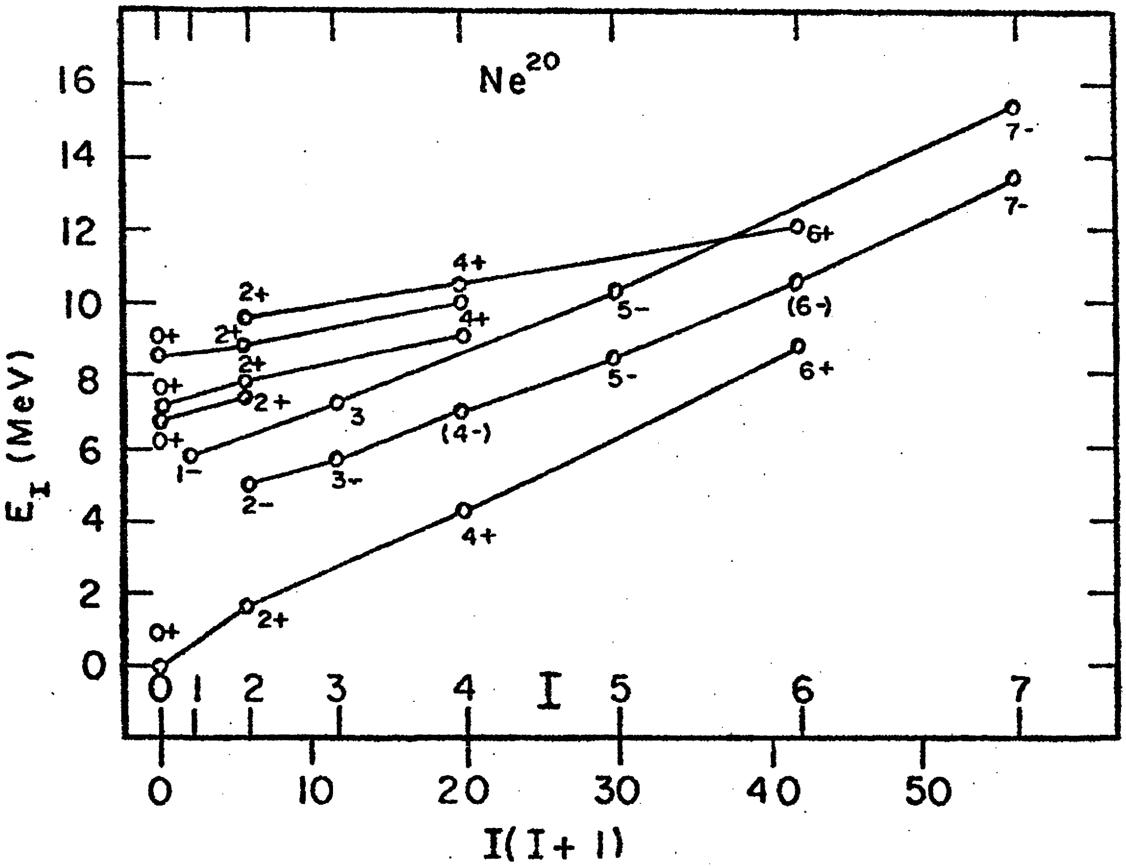

FIGURE 6.2 Rotational band structure ascribed to excitations in ^{20}Ne (Go 65).

and is dependent on the intrinsic excitation and defined by the K quantum number which is the projection of the angular momentum I on the nuclear symmetry axis; and

(iii) ξ represents the effective moment of inertia about the axis of rotation which is perpendicular to the symmetry axis.

The various rotational bands are specified by the K quantum number; the 0^+-2^+-4^+ states considered in the present measurements are described as members of the K=0 ground state rotational band, the 2^- and 3^- states as members of the K=2 negative parity octupole vibrational band and the 1^- state as a member of the K=0 negative parity octupole vibrational band (Li 65).

A further indication of the collective nature of the excitations in ^{20}Ne is the enhancement over the single particle estimate of the electric quadrupole (E2) gamma ray transition strengths; this was illustrated, in figures shown by Litherland (Li 65), by the peaking of the E2 transition strength as a function of mass number at and just beyond ^{20}Ne. The E2 transition strengths between members of the ground state rotational band provide a measure of the intrinsic quadrupole moment of the ground state. The reduced transition probability $B(E2, 0^+ \rightarrow 2^+)$, i.e. the transition strength with the transition energy dependence removed, is related to the intrinsic quadrupole moment Q_0 by the expression as quoted by Gove (Go 60) :

$$B(E2,0^+\to2^+) = \frac{5}{16\pi} Q_0{}^2e^2 \qquad (6\text{-}9)$$

where e is the electronic charge. Following the discussion of Stelson et al (St 65), if the nucleus is considered as a uniformly charged spheroid, the surface of which is defined by the relation :

$$R = R_0\left[1+\beta_2Y_{20}(\theta',\phi')\right] \qquad (6\text{-}10)$$

then $$Q_0 = \frac{3}{\sqrt{5\pi}} ZR_0{}^2\beta_2 \qquad (6\text{-}11)$$

where (i) Z is the atomic number of the nucleus; and

(ii) R_0 is the spherical nuclear charge radius taken as $1\cdot2A^{1/3}$ fermi.

Stelson et al (St 65) have tabulated the values of $B(E2,0^+\to2^+)$ and the corresponding value of β_2 derived from equations (6-9) and 6-11) for a range of nuclei and cited a deformation parameter of β_2=0·87±·08 for ^{20}Ne. It has been realized that this value was based on measurements which are now superseded; a more reliable determination of $B(E2,0^+\to2^+)$ has been obtained from the lifetime measurements of Evans et al (Ev 65) and it yields via equations (6-9) and (6-11) a value of β_2=0·67±·03. As pointed out by Gove (Go 60) neither the reduced transition probability nor the lifetime measurement determines the sign of the quadrupole moment, i.e. whether the deformation of the nucleus is prolate or oblate. However the plot of Q_0 as a function of atomic mass number, shown by Gove, includes data for the spectroscopic quadrupole moment of odd A nuclei and clearly indicates that ^{20}Ne is of prolate deformation, i.e. β_2 is positive. For a more general definition of the nuclear surface :

$$R = R_0\left[1 + \beta_2 Y_{20}(\theta', \phi') + \beta_4 Y_{40}(\theta', \phi')\right] \qquad (6\text{-}12)$$

as subsequently ascribed to ^{20}Ne in the coupled channels analysis of the present measurements, Stelson et al give the relation accurate to second order for β_2, β_4 and β_{st} :

$$\beta_{st} = \beta_2(1 + 0{\cdot}36\beta_2 + 0{\cdot}96\beta_4) + 0{\cdot}33\beta_2{}^2 \qquad (6\text{-}13)$$

where β_{st} is the quantity which should be compared to the β_2 values tabulated by Stelson et al (St 65). The value of β_2 discussed here is a measure of the deformation of the uniform charge distribution of radius $R_0 = 1{\cdot}2A^{1/3}$ fermi; the related parameter considered in section 6.1 is a measure of the deformation of the nuclear optical potential. An agreement to within at least 50% between these two estimates of β_2 is indicated by the analysis of Rost (Ro 63) and Buck (Bu 63) and a lower limit of the quadrupole deformation of the optical potential appropriate for ^{20}Ne of $\beta_2 > 0{\cdot}3$ is regarded as reasonable. Thus in view of the collective nature of the excitations in ^{20}Ne together with the attendant strong deformation it is considered that a coupled channels calculation with the Legendre expansion of the interaction potential is particularly appropriate for describing the direct scattering contribution in the present elastic and inelastic alpha scattering measurements.

6.3 Additional Comments on Applicability of Coupled Channel Analysis

As already discussed with reference to the spherical optical potential analysis of chapter five, the energy dependence of the present measurements appears more pronounced than that expected from direct scattering processes. In attempting then to describe the present scattering measurements in terms of the coupled channels formalism, it is assumed that direct processes contribute significantly to both elastic and inelastic scattering. This approach is consistent with and supported by the analysis of chapter five where there is evidence for an underlying average optical potential corresponding to an energy independent contribution to the elastic scattering. The remarks of sections 4.4 and 5.1 concerning the relation of the present measurements to those at higher energies where direct processes would be dominant are based on systematics pointed out for both the elastic and inelastic, principally that of 2^+, scattering. Thus it seems consistent to extend the approach of chapter five to a coupled channels analysis assuming then that the direct processes of both elastic and inelastic scattering will be evident. The cross sections for scattering from the 2^+ and 4^+ states, as noted in section

4.3, are comparable to that of the elastic scattering and as such support the description of the scattering from these states in terms of collective excitations.

6.4 Procedure of Analysis

The analysis was performed using the coupled channels code written by T. Tamura (see appendix V). This code, based on the formulation given in the review article by Tamura (Ta 65), is very fully described in the report ORNL-4152 (unpublished).

The scattering considered explicitly was that from the 0^+, 2^+ and 4^+ states. In principle the 2^- and 3^- states considered as members of a 2^- octupole vibrational band and the 1^- state considered as a member of the negative parity octupole vibrational band could also have been explicitly considered. However such a six state coupling calculation would be impractical with regard to computation time. The rotational coupling to the ground state was considered the most important in view of the strong ground state deformation indicated in section 6.2, and the practical demands of available computation time confined the major part of the analysis to the three state 0^+-2^+-4^+ coupling. As was noted in section 4.3 scattering from the 2^-, 3^- and 1^- states is somewhat less than that from the 2^+ and 4^+ states and as such could be considered as less strongly coupled to the elastic scattering than that from the 2^+ and 4^+ states; Mitchell et al (Mi 64) have pointed out however that a small cross section is not sufficient condition for assuming weak coupling.

Options available in using the code to describe rotational excitation include :

(i) terms with ℓ=0, 2 and 4 in the Legendre expansion of expression (6-6);

(ii) specification of the nuclear surface in terms of β_2 and β_4 deformations;

(iii) complex, in addition to real, coupling, i.e. deforming both real and imaginary potentials as is given in expression (6-7);

(iv) coulomb excitation corresponding to excitation of collective states via the interactions denoted by $V_{c_1}(r)$ and $V_{c_2}(r)$ of equation (6-3); and

(v) six or four parameter optical potential with volume or surface absorption.

Both complex coupling and coulomb excitation required an increase in computation time of approximately a factor of two and so were omitted from the majority of calculations; some consideration of these effects is discussed in section 6.5. The usual form of calculation is summarized in table 6.1 and is subsequently referred to as the standard calculation; this calculation required a computation time on the IBM 360/50 of eleven minutes.

Table 6.1

Standard Calculation	
States Coupled	$0^+ - 2^+ - 4^+$
Interaction Terms in Legendre Expansion (6-6)	ℓ = 0, 2 and 4
Form of Coupling	Deformation of real nuclear potential only
Deformation	Quadrupole and Hexadecapole i.e. $\beta_2 \neq 0$; $\beta_4 \neq 0$

As the automatic search method of minimizing χ^2, as employed in chapter five, was impractical for calculations requiring eleven minutes per computation, the comparison of the experimental and theoretical angular distributions was performed by visual evaluation of each of the computer plotted outputs.

The analysis was applied to the data at the energies of 13·69, 13·92, 14·09 and 14·90 MeV on the basis of the relatively good optical model description of the elastic scattering obtained at these energies as was discussed in chapter five. In addition the analysis was also applied to the 14·70 and 12·217 MeV data; of the lower energies the 12·217 MeV data were considered the most appropriate as the 2^+ angular distribution showed a well defined forward angle maximum and the data were the least influenced by the pronounced structure seen in the integrated 0^+ and 2^+ yields of figure 4.6.

A four parameter optical potential was employed throughout this analysis. The partial wave expansion was taken up to $\ell=14$ as the contributions from higher ℓ values were found at 14·90 MeV to be of no significance; this truncation is consistent with the reflection coefficients and phases of table 5.2 where it is seen that :

$$\eta_\ell e^{2i\delta_\ell} \approx 1 \text{ for } \ell \geq 10$$

Initial exploratory analysis employing the standard calculation, discribed in table 6.1 was applied to the 14·90 MeV data. A range of real well depths of V=50 to 220 MeV, for values of $1{\cdot}7 \leq r_0 \leq 1{\cdot}9$ and $0{\cdot}40 \leq a \leq 0{\cdot}55$ was considered. A positive value of β_2 was appropriate for ^{20}Ne as is discussed in section 6.2 and the range of values considered was $0{\cdot}45 \leq \beta_2 \leq 0{\cdot}60$ (see section 6.6). The effect of a hexadecapole deformation, i.e. $\beta_4 \neq 0$ was also considered; negative values of β_4 were found to be most unsatisfactory and values of β_4 were subsequently restricted to positive values $\leq 0{\cdot}35$. A substantial decrease in the imaginary well depth, by a factor of 2 to 3, as compared to that derived in the spherical potential analysis was necessary to approximate the observed scattering. In addition there was little or no correlation of the preferred values of V with those corresponding to the χ^2 minima of figure 5.5. Such behaviour is expected as :

(i) the strongly excited 2^+ and 4^+ states are now treated explicitly and are not associated with the imaginary potential; and

(ii) the coupling in the ground state rotational band is so strong that the spherical potential analysis could be regarded as a parameterization of the elastic scattering in the presence of strong coupling and thus does not give a particularly significant estimate of V.

Tamura (Ta[1] 65) in analyzing 28 MeV alpha elastic and inelastic scattering on ^{24}Mg noted the need for a decrease in W of ≈40% in comparing a coupled channel calculation to that employing a spherical potential. It was also pointed out in this paper that a difficulty in analyzing scattering involving rotational excitations is the interrelation of the coupling scheme and the optical potentials. Thus in the present analysis, where the same problem was evident, no attempt was made to approximate the parameters of the three state coupling calculation by those of either a two state calculation or those of the elastic scattering analysis of chapter five. The effect of including an additional state in the coupling scheme is considered in section 6.5.

Thompson et al (Th 67) have indicated that the ambiguity in the depth of the real potential employed to describe elastic scattering may be resolved by a coupled channels calculation; their analysis shows a preference for V≈160 MeV in describing 10·8 MeV alpha scattering on ^{24}Mg from the ground and first excited state. In view, however, of the marked success of the coupled channels calculation of:

(i) Hendrie et al (He 68) in describing 50 MeV alpha scattering on rare earth nuclei (V≈66 MeV); and of

(ii) Tamura (Ta^1 65) in describing 28 MeV alpha scattering on ^{24}Mg (V≈54·4 MeV)

it would seem that the ambiguity in the real well depth is not resolved in this form of analysis. Consequently in the present analysis there was no attempt to study a real well depth ambiguity and the calculations were restricted to a range of V≈80 to 100 MeV, a region for which the initial exploratory analysis showed a marginal preference.

6.5 Results of Coupled Channels Analysis

The results presented in this section represent the best simultaneous fits to the 0^+-2^+-4^+ scattering, as determined by visual evaluation, for the data at the energies of 12·217, 13·69, 13·92, 14·09, 14·70 and 14·90 MeV. A procedure of varying one or two parameters at each successive calculation was based on the sensitivity, which became apparent, of the distribution shapes to various parameters;

for example :

(i) increasing V, β_2 or β_4 moved the 0^+ diffraction patterns to smaller angles and increased the 2^+ and 4^+ cross sections; and

(ii) increasing β_4 also produced a clockwise rotation of the 4^+ distribution.

The geometrical parameters, on the basis of the analysis applied to the 14·90 and 14·70 MeV data were subsequently held fixed at values of r_0=1·82 fermi and a=0·45 fermi; the coulomb radius was fixed throughout the analysis at r_c=1·33 fermi. In contrast to the analysis of chapter five the volume and surface absorption term did not appear to be equivalent; a surface absorption term gave slightly improved agreement with observation and was employed in the analysis described. Denoting the volume absorption form factor; given in equation (6-2), as $f(r,\theta',\phi')$ the surface absorption form factor is of the form $4a \frac{d}{dr} f(r,\theta',\phi')$; the $4a$ gives this factor a maximum value of unity, as in the volume term.

The best fits derived, employing the standard calculation, are shown in figures 6.3(a) and (b) and the corresponding parameters are given in table 6.2.

The calculations of elastic scattering in general severely underestimate the observed cross sections at the central angles of the distributions. The calculations of the inelastic distributions are somewhat more satisfactory

Table 6.2

Incident Energy (MeV)	r_0=1·82 fermi; a=0·45 fermi; r_c=1·33 fermi			
	V(MeV)	Ws(MeV)	β_2	β_4
12·217	88·0	3·0	0·55	0·20
13·69	82·0	2·5	0·57	0·20
13·92	84·0	2·5	0·56	0·20
14·09	79·0	2·0	0·55	0·15
14·70	82·0	2·5	0·55	0·15
14·90	81·5	2·5	0·55	0·20

FIGURE 6.3(a)

Comparison of calculations of 0^+-2^+-4^+ scattering (solid line), employing the parameters of table 6.2, with the observed alpha scattering on ^{20}Ne (dots)

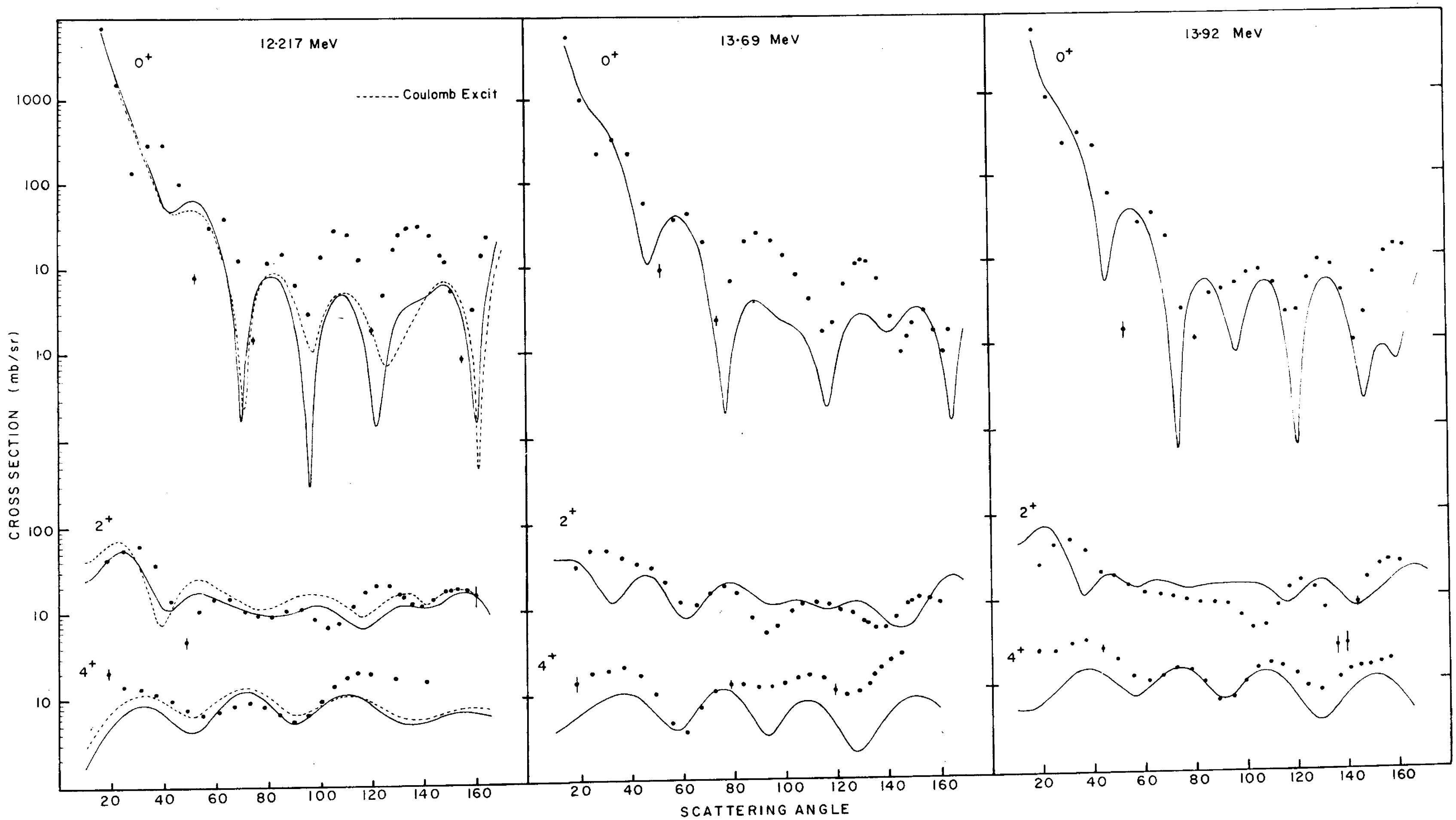

12·217 MeV
13·69 MeV
13·92 MeV
------ Coulomb Excit
0^+
2^+
4^+
CROSS SECTION (mb/sr)
1000
100
10
1·0
SCATTERING ANGLE
20 40 60 80 100 120 140 160

FIGURE 6.3(b)

Comparison of calculations of 0^+-2^+-4^+ scattering (solid line), employing the parameters of table 6.2, with the observed alpha scattering on ^{20}Ne (dots)

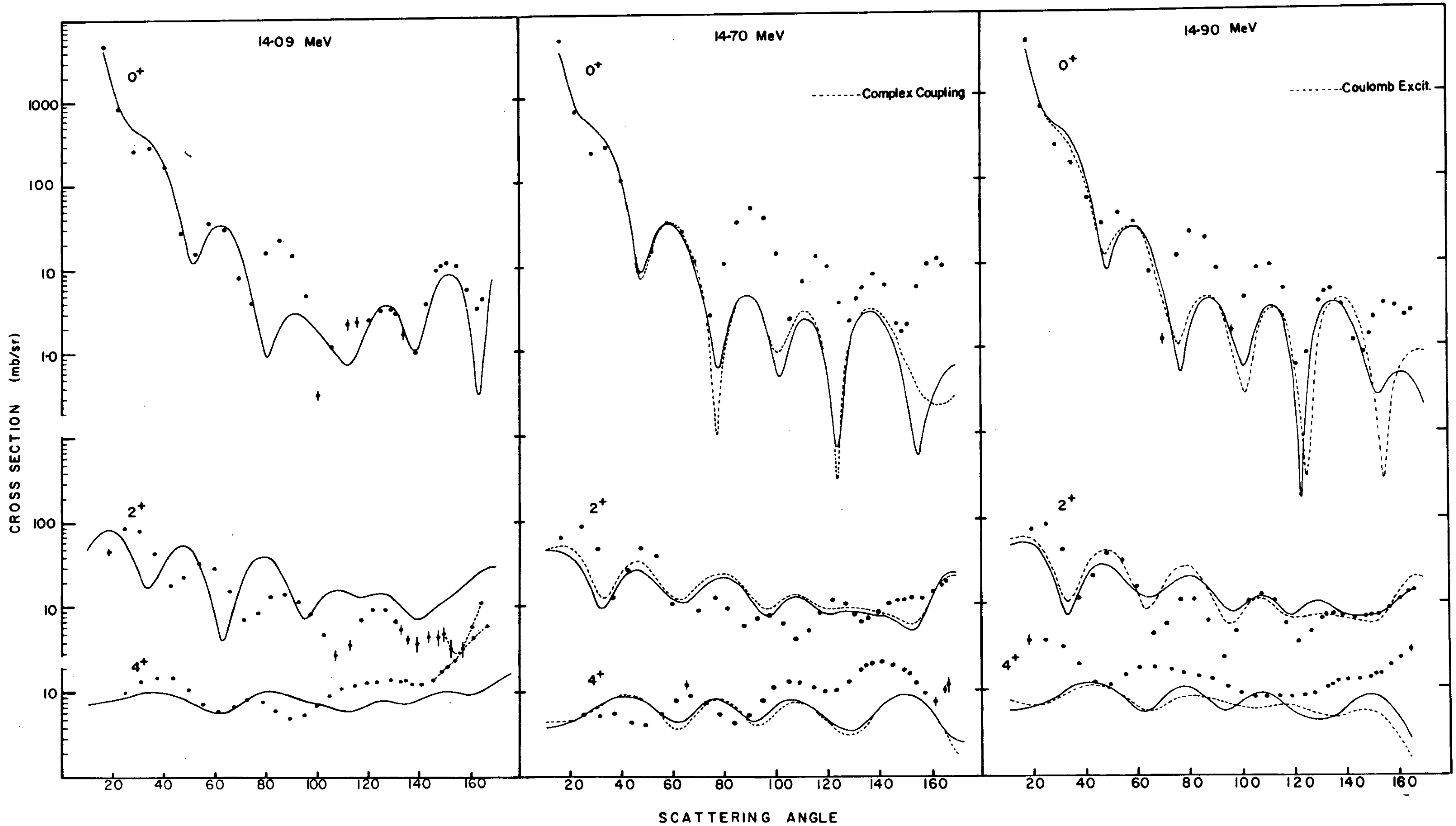

14·09 MeV
14·70 MeV
14·90 MeV
Complex Coupling
Coulomb Excit.
0+
2+
4+
CROSS SECTION (mb/sr)
1000
100
10
1·0
SCATTERING ANGLE
20
40
60
80
100
120
140
160

in that the magnitudes of cross section are approximately reproduced together with some agreement in shape in both the 2^+ and 4^+ distributions. Improvement in the description of the elastic scattering would have necessitated deterioration in the description of the inelastic distributions.

The effect of varying the deformation parameters is shown in figure 6.4 where the calculation corresponding to the 13·92 MeV parameters of table 6.2 are compared to calculations employing values of :

(i) $\beta_2 = 0{\cdot}56 \pm 0{\cdot}06$ and $\beta_4 = 0{\cdot}2$; and

(ii) $\beta_2 = 0{\cdot}56$ and $\beta_4 = 0{\cdot}2 \pm 0{\cdot}1$.

The shapes are seen to be particularly sensitive to the value of β_2 and to a lesser extent to β_4. The nature of the fit of figure 6.3(a) for the 13·92 MeV data is approximate enough to illustrate definition of β_2 to within the limits shown, i.e. $\beta_2{=}0{\cdot}56{\pm}{\cdot}06$; the determination of β_4 is somewhat more subjective but it is also considered to be defined to within the shown limits, i.e. $\beta_4{=}0{\cdot}20{\pm}{\cdot}10$. The 13·92 MeV data were taken for this illustration as they were perhaps the most satisfactorily described.

Higher order effects of complex coupling, coulomb excitation and the coupling of an additional state were considered as a possible means of providing a more appropriate description of the scattering. The effects of complex coupling and coulomb excitation although both producing

FIGURE 6.4

Comparison of the 0^+-2^+-4^+ calculations of the 13·92 MeV scattering employing the parameters of table 6.2 (solid line) with calculations (dashed line) in which β_2 and β_4 were varied by ±0·06 and ±0·10 respectively. The observed 13·92 MeV scattering is indicated by dots

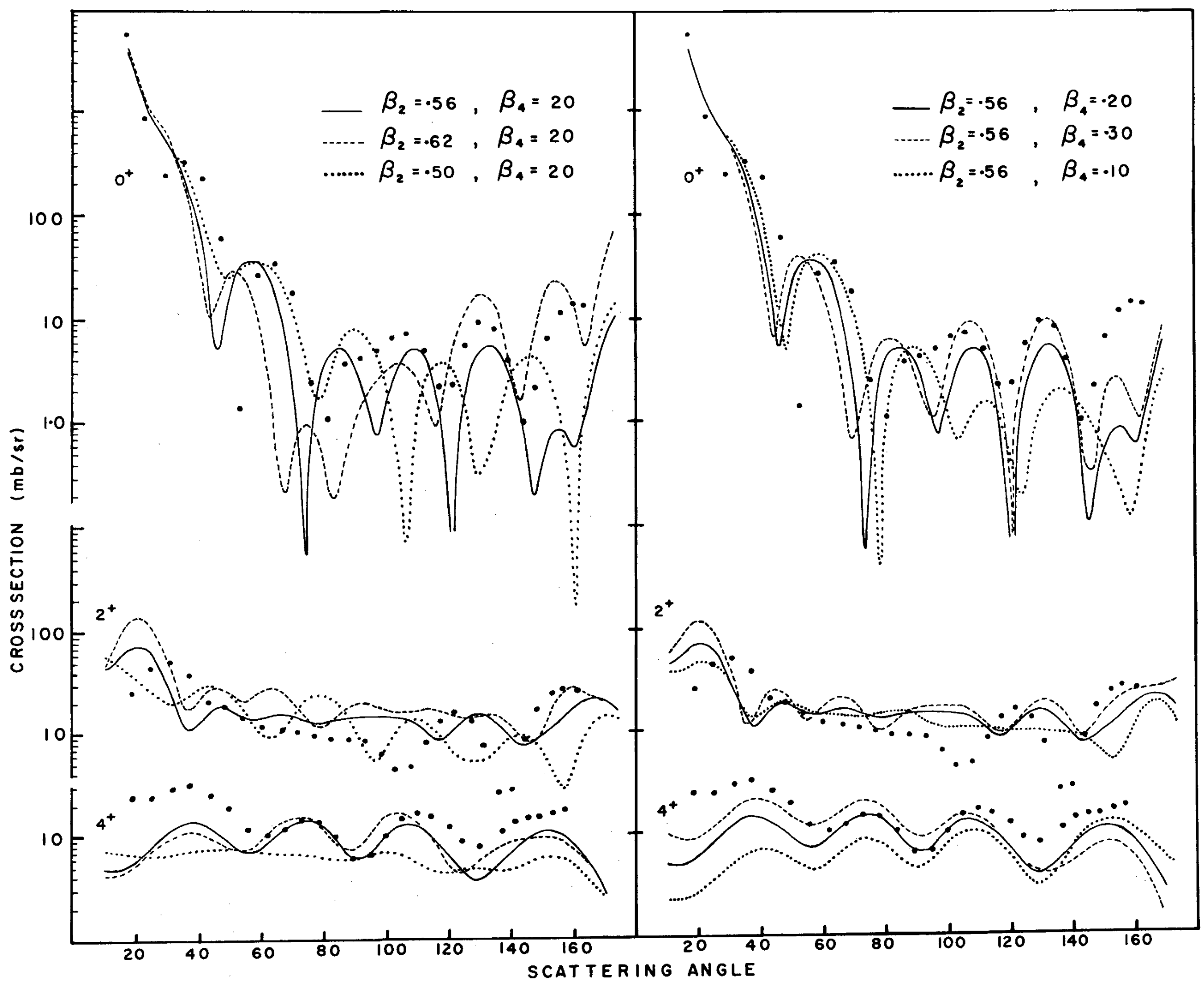

β_2 =·56 , β_4 = 20
β_2 =·62 , β_4 = 20
β_2 =·50 , β_4 = 20
β_2 =·56 , β_4 =·20
β_2 =·56 , β_4 =·30
β_2 =·56 , β_4 =·10
0+
2+
4+
100
10
1·0
CROSS SECTION (mb/sr)
20 40 60 80 100 120 140 160
SCATTERING ANGLE

variations in the inelastic cross sections of up to 25% were not significant with regard to the present analysis in view of the quality of obtained fits. The result of calculations, with the 14·90 and 12·217 MeV parameters of table 6.2, incorporating coulomb excitation are included in the plots of figures 6.3(a) and (b). A calculation employing complex coupling and the 14·70 MeV parameters of table 6.2 is also included in figure 6.3(b).

Additional coupling of the 6^+ state, at an excitation of 8·79 MeV in ^{20}Ne and regarded as a member of the ground state rotational band (see figure 6.2), could be considered in the scheme of the standard calculation without increased parameterization and the effects of this additional coupling were considered. The best fits obtained in a rather limited search about parameter values of table 6.2 are shown in figure 6.5. The 2^+ scattering appears a little more satisfactorily described although in the case of the 14·90 MeV data this occurred at the expense of loss of agreement in phase between the calculated and observed elastic scattering; the phase of the diffraction pattern of the 4^+ distribution relative to that of the 0^+-2^+-4^+ calculation is seen to be quite sensitive to the additional coupling. The parameters corresponding to the four state calculations of figure 6.5 are given in table 6.3. It is seen by comparison with the parameters of table 6.2 that the additional coupling necessitated mainly a reduction in V and β_2. In view of the

FIGURE 6.5

Comparison of 0^+-2^+-4^+-6^+ calculations (solid line) employing the parameters of table 6.3, with the observed 0^+-2^+-4^+ scattering (dots)

$0^+ - 2^+ - 4^+ - 6^+$ Calculations

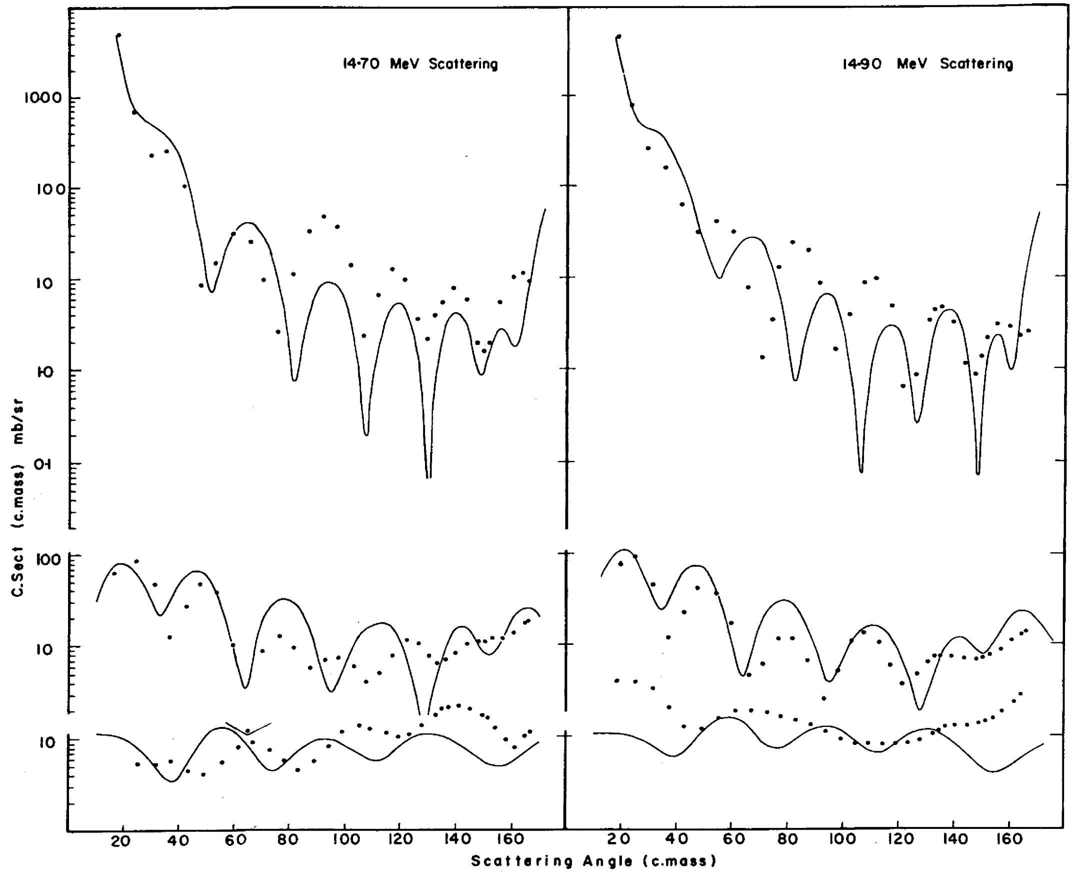

quality of the fits and the limited attempts to find optimum parameters these new estimates of the deformations in table 6.3 cannot be considered as particularly significant; however the comparison of tables 6.3 and 6.2 serves to illustrate that the potential and coupling parameters are dependent on the coupling scheme being considered.

Table 6.3

Incident Energy (MeV)	r_0=1·82 fermi; a=0·45 fermi; r_c=1·33 fermi			
	V(MeV)	Ws(MeV)	β_2	β_4
14·70	76·0	2·0	·50	·20
14·90	75·0	2·0	·50	·15

The effect of employing a six parameter potential in the standard calculation was also considered and found, as with the complex coupling and coulomb excitation, to be insignificant as far as the present fits were concerned.

6.6 Discussion of the Coupled Channels Analysis

The agreement between theory and observation, although poor, is perhaps as close as could be expected in view of the energy dependence inherent in both elastic and inelastic scattering. The mean of the values of the deformations of table 6.2, β_2=0·55 and β_4=0·18, appear from the comparison made in figure 6.4 to be defined to within ≈10% and 100% respectively. It would however be unreasonable in view of the poor quality of the fits to suggest that these values represent an accurate determination of the ground state deformation of the ^{20}Ne nucleus.

The comparison of calculated and observed scattering shown in figures 6.3(a) and (b) indicates that possibly the most satisfactory result of the analysis is the approximate description of the 4^+ scattering as for example at 12·217 and 13·92 MeV . The magnitudes of the 2^+ cross sections are approximately reproduced while at 12·217, 13·92 and 14·90 MeV the shapes of the calculated 2^+ distributions are comparable although not exactly in phase with the observed angular distributions. The elastic scattering cross section magnitude with the exception of that at 13·92 and to a lesser extent at 14·09 MeV is the most unsuccessfully described although this may reflect attempts in the fitting calculations to reproduce the phase of the observed distributions in preference to the cross section magnitude.

Although the discussions of sections 6.1 to 6.3 indicate that a coupled channels analysis can be regarded as more appropriate than the analysis in terms of a spherical optical potential, the calculations of the former are typically in poorer qualitative agreement with the observed scattering than those of the latter which were considered in chapter five (cf. figures 5.4 and 6.3). This no doubt reflects the constraints imposed by the need to describe an additional two angular distributions but it is also attributed to the fact that an automatic search code as used in the less constrained spherical potential analysis is particularly powerful and at the same time exhaustive. It was however not possible to be exhaustive in considering the ranges of variation of parameters in the present calculations. To some extent the deficiencies of the fits derived in the present coupled channels analysis may represent a null result in that the ranges of parameters considered may have been inappropriate. This remark is particularly pertinent for the range of β_2 values considered; the range of $0{\cdot}45 \leq \beta_2 \leq 0{\cdot}60$ was chosen from a comparison of :

(i) analysis of 28 MeV alpha scattering via DWBA yielding $\beta_2 = 0{\cdot}51$ (Sa 65);

(ii) the values of β_2 for ^{20}Ne and ^{24}Mg of $0{\cdot}87 \pm {\cdot}08$ and $0{\cdot}64 \pm {\cdot}05$ respectively tabulated by Stelson et al (St 65); and

(iii) the value of $\beta_2 = 0{\cdot}34$ derived for ^{24}Mg in a coupled channels analysis of 28 MeV alpha scattering on ^{24}Mg (Ta[1] 65).

It is noted that the DWBA analysis of the same 28 MeV alpha scattering on ^{24}Mg yielded $\beta_2 = 0{\cdot}34$ (Sa 65), a value equivalent to that determined in the coupled channel calculation noted above. As far as is known to the author there have been no published coupled channels calculations of alpha scattering on ^{20}Ne. The DWBA analysis of Satchler thus represented the best available estimate of the appropriate optical potential deformation. A DWBA analysis of the 18 MeV alpha scattering on ^{20}Ne yielded β_2 values of 0·29, 0·38 and 0·44; the value of 0·29 gave a rather poor fit and the quoted final result was $\beta_2 \approx 0{\cdot}4$ (Lu 66). This estimate of 0·4 was considered less reliable than that by Satchler because of the lower energy of scattering. Austern (Au 65) has pointed out that the relative importance of channel coupling in determining elastic scattering decreases with increasing energy and that the DWBA estimate of single step excitation correspondingly becomes more valid. It would also be expected that with increasing energy the perturbations of the elastic scattering arising from compound nucleus interactions would diminish and thereby further enhance the validity of the DWBA (Mo 65).

The three estimates of β_2 determined by Lucas et al corresponded to discrete ambiguities in the real well depth of $V \approx 25$ MeV ($\beta_2 = 0{\cdot}44$), $V \approx 52$ MeV ($\beta_2 = 0{\cdot}38$) and $V \approx 82$ MeV ($\beta_2 = 0{\cdot}29$); as in other DWBA analyses of inelastic alpha scattering on several nuclei ($A \leq 40$) these authors found the best fit was obtained for $V \approx 25$ MeV, i.e. the shallowest of the ambiguities. The DWBA analysis of Satchler (Sa 65), yielding β_2 values of 0·51 and 0·34 for ^{20}Ne and ^{24}Mg respectively, considered only a real well depth of $V \approx 55$ MeV. As no study of a possible bias for shallow V in a coupled channels analysis was known to the author the best estimates from DWBA analysis, regardless of the real well depth and taken as $\beta_2 = 0{\cdot}51$ with lesser weight attached to the $0{\cdot}44$ estimates, were considered as the most appropriate indications of β_2 for the present analysis. The extension of the range of considered β_2 values to $<0{\cdot}6$ was a consequence of the trend indicated in the analysis for $\beta_2 = 0{\cdot}5$.

It has been subsequently realized that the above value of the charge deformation of $\beta_2 = 0{\cdot}87$ for ^{20}Ne was based on now superseded measurements and as noted in section 6.3 a more appropriate value is $0{\cdot}67$. Thus the charge deformations, as defined by Stelson et al, are comparable for ^{20}Ne and ^{24}Mg and not in the ratio of $\approx 1{\cdot}35$ which would have been more consistent with the results (i) and (iii) above.

Blair stated that a deformation length $\delta_\ell = \beta_\ell R$, where R is the radius parameter associated with the dimensionless parameter β_ℓ, is a more appropriate quantity for comparison of deformations derived from models with differing dependence on the nuclear radius (Bl 65). The deformation lengths for ^{20}Ne, determined in Fraunhofer diffraction analysis of 42 MeV alpha scattering on ^{20}Ne (Bl 64), were $\delta_2 = 1{\cdot}77$ and $\delta_4 = 0{\cdot}6$ which with a strong absorption radius of ≈ 6 fermi yielded $\beta_2 \approx 0{\cdot}3$ and $\beta_4 \approx 0{\cdot}1$; similar analysis for similar data yielded values of $\delta_2 = 1{\cdot}66 \pm {\cdot}04$ and $\beta_2 \approx 0{\cdot}27$ for ^{24}Mg (Na 68).

In accordance with Blair's postulate it is seen to be more appropriate to compare the diffraction model deformation length for ^{20}Ne of δ_2=1·77 fermi with the deformation length of ≈2·2 fermi as defined by β_2=0·67 and the charge radius of $1{\cdot}2A^{1/3}$ fermi; the diffraction model estimate of β_2≈0·3 is quite dissimilar to the charge deformation value of β_2≈0·67. The diffraction model analysis for ^{20}Ne yields a non zero δ_4 which, if taken into account via an equation of the form of (6-13), results in closer agreement with the deformation length δ_2≈2·2 fermi. It is noted that the analysis of Springer of 50 MeV alpha scattering on ^{20}Ne, via a parameterized phase shift extension of the diffraction model, yielded δ_2=1·72 and δ_4=0·36 (Sp 65).

Regardless of the value of β_2 that might be extracted from the above-mentioned diffraction analysis the similarity in deformation lengths δ_2 for ^{20}Ne and ^{24}Mg is consistent with the similarity of charge deformation, as defined by Stelson et al (St 65), and noted above, for these two nuclei. Consequently it might be expected that β_2 of the present coupled channel calculations would be comparable to the result of the coupled channel calculation for ^{24}Mg of β_2=0·34 (Ta[1] 65).

Although the above discussion suggests that the present analysis might be improved by consideration of a value of β_2≈0·35, a negation of Satchler's DWBA analysis, it is again noted that the larger value of β_2=0·55 of table 6.2 approximately reproduces the magnitudes of the present inelastic scattering cross sections. The average of the presently derived β_2 and β_4 estimates of table 6.2 yields via equation (6-13) a value of $\beta_{st} \approx 0{\cdot}75$ which is seen to be in reasonable agreement with the charge deformation $\beta_2 \approx 0{\cdot}67$. The present analysis is thus in keeping with a comparison of the dimensionless deformation parameters rather than a comparison of the deformation lengths as suggested by Blair. The comparative study of β_2 and β_4 values shown in figure 6.4 indicates that the presently derived β_2 value is appropriate; however a firm conclusion is not considered justified in view of the quality of the fits and in the absence of a study of calculations for the above proposed lower values of $\beta_2 \approx 0{\cdot}35$ since the preferred value of β_2 may reflect the definition of remaining parameters in particular V and r_0 with which β_2 shares some ambiguity.

The quality of the present fits was not satisfactory enough to indicate the importance of the higher order effects of complex coupling, coulomb excitation, additional coupling or the need for a six parameter optical potential. In neglecting the 6^+ state coupling it might be expected that the 0^+-2^+-4^+ calculations would overestimate the 4^+ scattering cross section by approximately a factor of two (Ta[1]65) and that in principle the 4^+ scattering of the present 0^+-2^+-4^+ calculations would be the least well described. By way of contrast the fits shown in figure 6.3(a) and (b) indicate that the 4^+ scattering is perhaps the most satisfactorily described; such a result may reflect an effect in the 0^+-2^+-4^+

calculations of detailed searching whereby some implicit parameterization of the additional coupling, such as occurs in DWBA, has been included.

It is considered that the coupled channels analysis, constrained to yield an overall fit to the 0^+-2^+-4^+ scattering, rather than the spherical potential analysis of the 0^+ scattering has provided the more reliable estimate of the correctness of describing the observed scattering in terms of direct interaction processes. The approximate agreement between observation and calculation of the inelastic scattering suggests that the inelastic excitation proceeds to a large extent via a direct collective excitation. If the inelastic scattering is significantly influenced by direct interaction the same is true of the strongly coupled elastic scattering; however the greater discrepancies between theory and observation in the case of the elastic scattering suggest the influence of non-direct resonant processes is stronger in the elastic channel than in the inelastic. The qualitative success of approximately half of the fits of the less constrained spherical potential analysis, seen in figure 5.4, may represent very effective parameterization rather than parameters of physical significance; the relatively good fit to the 14·90 MeV elastic scattering of figure 5.4 is in marked contrast to the poorer overall fit to the 14·90 MeV 0^+-2^+-4^+ data of figure 6.3(b). The present analysis warns that success in describing the elastic scattering via a spherical optical potential does not ensure comparable success in the more appropriate coupled channels analysis.

6.7 Energy Dependence Implicit in Strong Coupling

Additional calculations have been performed to study the energy dependence of scattering as predicted by the strong coupling calculations.

Okai et al (Ok 62) have indicated that channel coupling in scattering can result in resonance behaviour in both elastic and inelastic cross sections. The two state coupled channels calculation of Mitchell et al (Mi 64) for 10 to 20 MeV alpha scattering on ^{12}C were suggestive of such behaviour and it was remarked that some of the resonant structure that had been experimentally observed was possibly a result of strong coupling.

For the calculations the parameters of table 6.2, derived in the standard calculation applied to the 0^+-2^+-4^+ scattering, have been averaged to yield the parameters of table 6.4.

Table 6.4

V(MeV)	Ws(MeV)	r_0(fermi)	a(fermi)	β_2	β_4
83·0	2·5	1·82	0·45	0·55	0·18

With the parameters of table 6.4, calculations of the

0^+-2^+-4^+ scattering, via the standard calculation, were performed for incident alpha energies of 12·0 to 15·0 MeV at 0·5 MeV intervals. By way of comparison the average set of parameters derived in the spherical potential description of elastic scattering included here in table 6.5, was employed to calculate the elastic scattering at the same energies. The results of these calculations are plotted in figure 6.6.

Table 6.5*

V(MeV)	W (MeV)	r_0(fermi)	a(fermi)
96·0	6·7	1·80	0·53

* Taken from analysis described in chapter five.

The most striking result, shown in figure 6.6, is the channel coupling prediction of the energy dependence of the shape of the elastic scattering angular distributions. As a function of increasing energy the 100° central maximum separates into two well-defined maxima, the two backward angle maxima at 12·0 MeV merge and finally an additional back angle maximum appears at 15·0 MeV. The elastic scattering as predicted by the spherical potential is seen to show similar but much less pronounced behaviour; the 120° maximum at 12·0 MeV slowly separates into two as a function of increasing energy.

FIGURE 6.6

Deformed and spherical optical potential calculations of alpha scattering on ^{20}Ne at energies of 12 to 15 MeV; the two sets of parameters employed, listed in tables 6.4 and 6.5 respectively, are average values presently determined

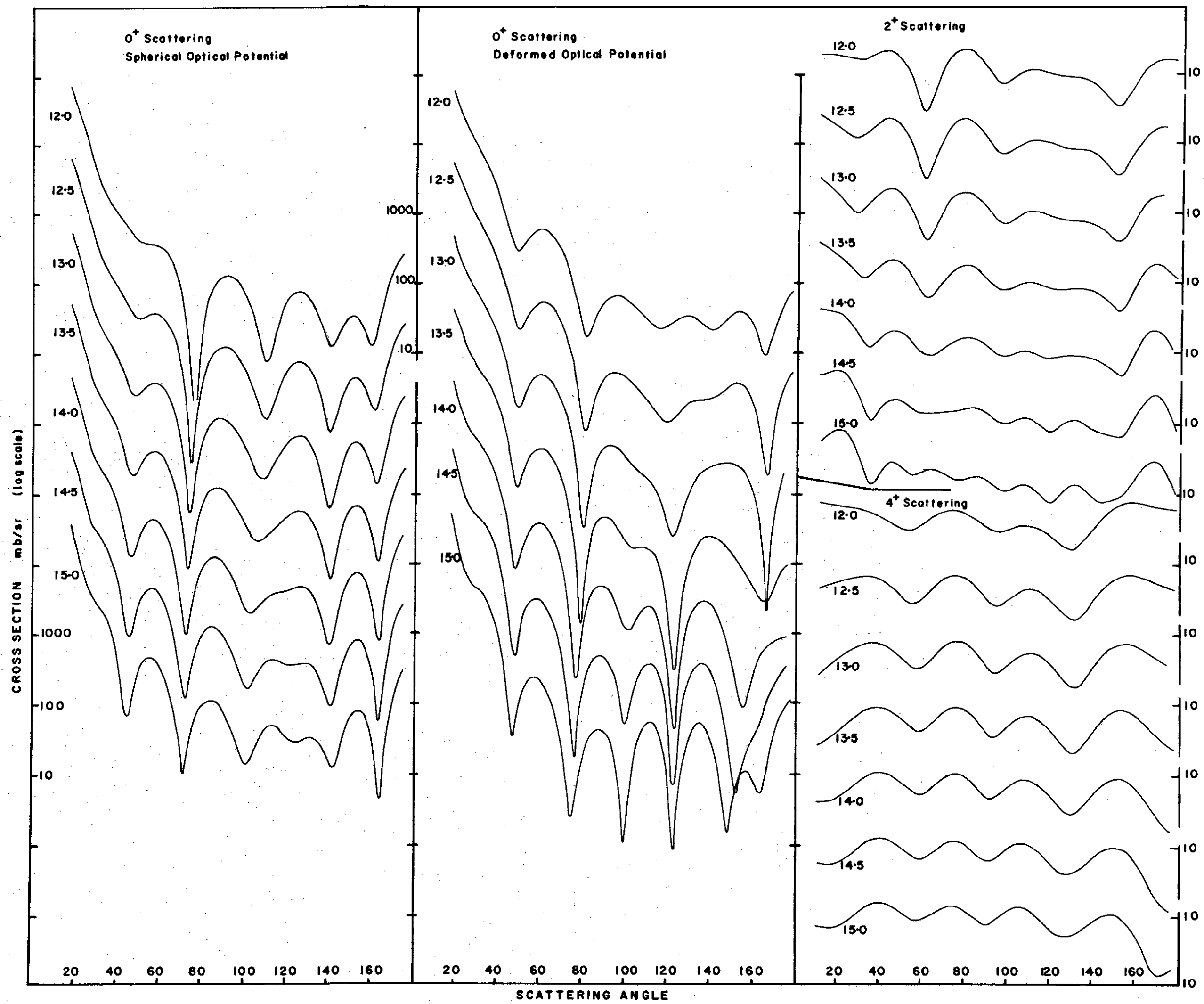

0+ Scattering
Spherical Optical Potential
0+ Scattering
Deformed Optical Potential
2+ Scattering
4+ Scattering
12·0
12·5
13·0
13·5
14·0
14·5
15·0
1000
100
10
CROSS SECTION mb/sr (log scale)
SCATTERING ANGLE
20
40
60
80
100
120
140
160

The coupled channel calculations of the 2^+ scattering show energy dependence in the shape of the angular distributions although to a lesser extent to that of the corresponding 0^+ scattering; the second maximum of the 12·0 MeV distribution separates into two with the increase in energy to 15·0 MeV. The predicted 4^+ angular distributions are rather insensitive to energy.

In the present measurements the elastic and inelastic scattering energy dependence is far more complicated than that shown by the coupled channel calculations of figure 6.6. By appropriate choice of angle, excitation functions of the differential cross section for elastic scattering could be obtained which would show in this energy range cross section variation of up to a factor of ten. However the width of this variation is much larger than that of the observed structure and there is no evidence in the present calculations to indicate structure as shown for example in figure 4.1(c). On the other hand it is noteworthy that the movement of the diffraction maxima in the observed elastic and 2^+ scattering, as qualitatively discussed in section 4.3 and illustrated in figure 4.4, may to some extent arise from the effects of strong coupling.

6.8 Inelastic Scattering from 2^- and $(3^-,1^-)$ States

Although not considered in the coupled channels calculations the observed inelastic scattering from the 2^- and $(3^-,1^-)$ states warrants some qualitative remarks and the present discussion is thus directed. In principle the scattering from these states could be considered in terms of the coupled channels, as noted in section 6.4, but the description of the scattering from the members of the ground state rotational band was not well enough defined to warrant the requisite and more complicated calculations.

Of particular interest is the scattering from the 2^- state. Eidson et al (Ei 62) have pointed out that the excitation of unnatural parity states, i.e. $(-1)^J \neq \Pi$, via inelastic alpha scattering on a spinless target nucleus cannot occur in a single scattering interaction with a single transfer of angular momentum, i.e. a one step process. The mechanisms proposed for the excitation of these states include the formation of an intermediate system as in a compound nucleus interaction or a more complicated direct process such as multiple, two step excitation or exchange scattering.

A prediction by Satchler, quoted by Eidson et al (Ei 62), suggested that the cross section for excitation of the unnatural parity state via a knock out process would decrease for $E\alpha > 20$ MeV. Bingham (Bi 66) has measured six angular distributions, for incident energies in the range 16 to 27 MeV, of inelastic alpha scattering from the 3^+ (6·27 MeV) state of ^{28}Si and found a marked decrease in the integrated yield at $E\alpha = 22$ MeV. A similar comparison for the excitation of the 2^- state of ^{20}Ne would be of interest; the present measurements and those of Seidlitz et al (Se 58) at 18 MeV define the low energy range of $\leqslant 20$ MeV but unfortunately in the range 20 to 30 MeV there is only the data of Kokame et al (Ko 64) at 28 MeV which is restricted to angles of $\leq 80^{o}$. However the present measurements of the 2^{-} scattering considered in conjunction with the 18, 28, 42 and 50·9 MeV data clearly define a decrease in cross section with increasing energy as was indicated by the comparison of 18 and 28 MeV alpha scattering data in a plot of Kokame et al (Ko 64) for unnatural parity state excitation in ^{16}O, ^{20}Ne, ^{24}Mg and ^{28}Si. The inhibition of the 2^{-} scattering relative to that of the 0^{+} and 2^{+} scattering increases with increasing energy and appears indicative of the interaction mechanism peculiar to this particular excitation.

The only theoretical calculation, known to the author, of the excitation of an unnatural parity state via alpha scattering on a spin zero target is that of Tamura (Ta^{1}65) for 28 MeV alpha scattering on ^{24}Mg. This calculation, employing a coupled channels approach, explicitly considered the four lowest members of the K=0 ground state rotational band coupled by a vibration to the K=2 band which includes the 3^{+} state at 5·22 MeV. The agreement of the calculation with the observed scattering was particularly impressive and supports the description of such unnatural parity step excitation in terms of a multiple step excitation. A similar coupled channels calculation applied to the data for alpha scattering on ^{20}Ne, at the higher energies of 28 and 42 MeV, could perhaps yield information which would aid in describing the presently discussed measurements and particularly those of the 2^- scattering.

CHAPTER 7

Optical Model plus Resonance Analysis

Analysis of several of the angular distributions of elastic scattering in terms of the addition of a Breit-Wigner resonant amplitude to an optical model scattering amplitude has been considered as a means of describing the energy dependence of the scattering.

7.1 Optical Model plus Resonance Formulation

The two ranges of energies to which most of the measured angular distributions are confined encompass pronounced structure in the elastic scattering excitation functions (see section 4.2). Attempts consequently have been made to describe this energy dependence with emphasis placed on the five elastic scattering angular distributions spanning well defined structure at ≈12.3 MeV. This approach was prompted by the analysis of Kim (Ki 65), in which the pronounced energy dependence of approximately 20 MeV alpha scattering on ^{24}Mg was considered by including the contribution from an isolated resonance in addition to that from scattering of an appropriate optical potential.

A Breit-Wigner resonant amplitude, modified by shift and penetration factors, and an amplitude corresponding to an approximately energy independent background occur in the single level resonance description of elastic scattering in the R-matrix formalism (La 58). In the present analysis of elastic scattering a Breit-Wigner amplitude has been added to a background scattering amplitude generated by an optical potential. This description is however not consistent with the R-matrix formalism as the background phases are no longer real but complex corresponding to the complex potential required to simulate non-elastic processes. In performing this analysis it is assumed then that a scattering amplitude analagous to that of the R-matrix theory will be approximately valid and that pronounced deviation from an average optical potential scattering amplitude may be accordingly represented by the contribution from a single resonant amplitude.

Postulating then the possibility of a resonant amplitude contribution to the partial wave ℓ_r, the scattering matrix element S_ℓ of equation (5-4) for $\ell=\ell_r$ is written as (Wu 62) :

$$S_\ell\left(1 + \frac{i\,\Gamma_\alpha}{(E_r-E) - \frac{i\Gamma}{2}}\right) \qquad (7\text{-}1)$$

where (i) $S_\ell=\eta_\ell e^{2i\delta_\ell}$ as defined in equation (5-5) and for which the complex phase is implicit in the reflection coefficient η_ℓ i.e. $\eta_\ell<1$;

(ii) Γ_α is the partial width for decay or formation of the resonant state via the elastic scattering channel;

(iii) Γ is the full width of the resonant state; and

(iv) E_r is the resonant energy incorporating in addition the usual shift factor.

Inserting expression (7-1) into equation (5-4) yields :

$$A(\Theta) = f_c(\Theta) + \frac{1}{2ik} \sum_{\ell=o}^{\infty} (2\ell+1) e^{2i\sigma_\ell} P_\ell(\cos\Theta) \cdot \left\{1 - S_\ell\left(1 + \delta_{\ell\ell_r} \frac{i\,\Gamma_\alpha}{E_r - E - \frac{i\Gamma}{2}}\right)\right\} \qquad (7\text{-}2)$$

where the subscript r denotes terms appropriate to the resonating partial wave.

Expression (7-2) has been employed in the present analysis. A more general form of this amplitude, as used by Kim (Ki 65), ascribes to the resonant term a background phase differing from that of the potential term; Γ_α of the resonant term is multiplied by a factor $e^{i\phi}$ with ϕ becoming then an additional adjustable parameter. The analysis by Lowe et al (Lo 66) and Tamura et al (Ta 64) of elastic proton scattering on ^{12}C was performed with a complex numerator in the resonant term of equation (7-2); this is equivalent to the form used by Kim. Satchler suggested (Sa 60) that unless a pronounced fluctuation from the scattering as described by the optical potential represents the contribution from one abnormally strong level the phase of the resonant term, i.e. $e^{i\phi}$ should be treated as an adjustable parameter. A further assumption then of the present analysis of the five angular distributions at ≈12·3 MeV is that the contribution from one particularly strong resonance is dominating the scattering. This approach is considered appropriate in view of the sharp and prominent peak in the elastic scattering excitation function at ≈12·3 MeV in both the differential cross section, shown in figure 4.2(c), and the integrated cross section, shown in figure 4.6. It is to be noted that the S_ℓ of expression (7-2) satisfies the unitarity condition of $|S_\ell|\leq 1$, i.e. flux is not created in the scattering interaction. The modification incorporating, in expression (7-2), the term $e^{i\phi}$ in the resonant amplitude necessitates an independent check of possible violation of unitarity; such a check was considered in the analysis of Tamura et al (Ta 64).

As considered in the discussions of chapters five and six, the spherical optical potential does not provide a particularly appropriate description of elastic scattering in the presence of strong inelastic scattering; the view adopted here, as in the analysis of chapter five, is that the spherical potential can however provide an effective parameterization of the direct potential scattering.

7.2 Optical Model plus Resonance Description of Elastic Scattering at ≈12·3 MeV

The resonant amplitude of equation (7-2) was incorporated by the author in the optical model code of Perey which was used in the analysis of chapter five. The code already contained a non-linear least-squares fitting subroutine but as a description was not available a known fitting subroutine, FITTEM (Ha 68), was appended to the code. With these modifications and the specification of one particular resonating partial wave automatic searching on the optical model parameters and the resonance parameters to minimize the quantity χ^2 of equation (5-6) was possible.

Initial fitting was applied 'on resonance' to the central energy angular distribution at 12·307 MeV. To determine the presence or otherwise of a resonating partial wave the value of ℓ_r was gridded from 0 to 9 and for each value an automatic search was made on the parameters V, W, r_0, a, Γ, Γ_α, and E_r. The starting values of the optical model parameters corresponded to the χ^2 minimum of V≈40 MeV in figure 5.1. The choice of parameters corresponding to this shallow discrete ambiguity was made on the basis that it would provide the most satisfactory description of the potential scattering; the preference for low V in minimizing χ^2 was seen in several of the plots of figure 5.1 and was particularly apparent in the analysis described in section 5.5 (ii). Throughout the analysis a four, rather than six parameter potential was employed in order to minimize the number of adjustable parameters and to maintain some consistency with procedures described in chapter five. The starting values of the resonance parameters corresponded to the approximate width and position of the peak in the excitation functions of figures 4.2(c) and 4.6; the partial width Γ_α was taken as $0{\cdot}9\mathrm{x}\Gamma$ for a value of Γ of 0·12 MeV and the resonance energy as 14 kev above the centre of mass energy of motion of 10·256 MeV (12·307 in Lab). This initial estimate of $\Gamma_\alpha \approx \Gamma$ was indicated in a preliminary analysis gridding ℓ_r and in which an ℓ_r=5 resonant amplitude seemed appropriate; the above starting value of E_r was taken from this preliminary analysis.

Using the starting values as described above and included in table 7.1, a grid of ℓ_r values from 0 to 9 with subsequent searching on the seven parameters yielded a pronounced preference for an ℓ_r=6 contribution with ℓ_r=5 also providing a reasonably adequate description. The parameters derived in this search procedure and the appropriate values of χ^2 are given in table 7.1 for ℓ_r=5 and 6; all other values of ℓ_r yielded very inadequate fits corresponding to large χ^2 values in general in excess of 200 with ℓ=7 yielding χ^2 of 160.

The fits corresponding to the two sets of parameters of table 7.1 are shown in figure 7.1 with and without the respective resonant amplitudes; the ℓ_r=5 result by

Table 7.1 *

	Γ_α	Γ	E_r	V	W	r_0	a	χ^2
	MeV					fermi		
Starting Parameters	·110	·120	10·270	40·25	3·93	1·90	·56	
$\ell_r = 5$	·114	·114	10·270	38·25	2·39	1·89	·54	110
$\ell_r = 6$	·117	·124	10·244	44·71	4·22	1·90	·46	61

* $r_c = 1·33$ fermi

FIGURE 7.1

Optical model plus resonance fits (solid line) to the 12·307 MeV elastic alpha scattering on ^{20}Ne (dots), as obtained with the parameters of table 7.1; the dashed lines correspond to the optical potential parameters of table 7.1

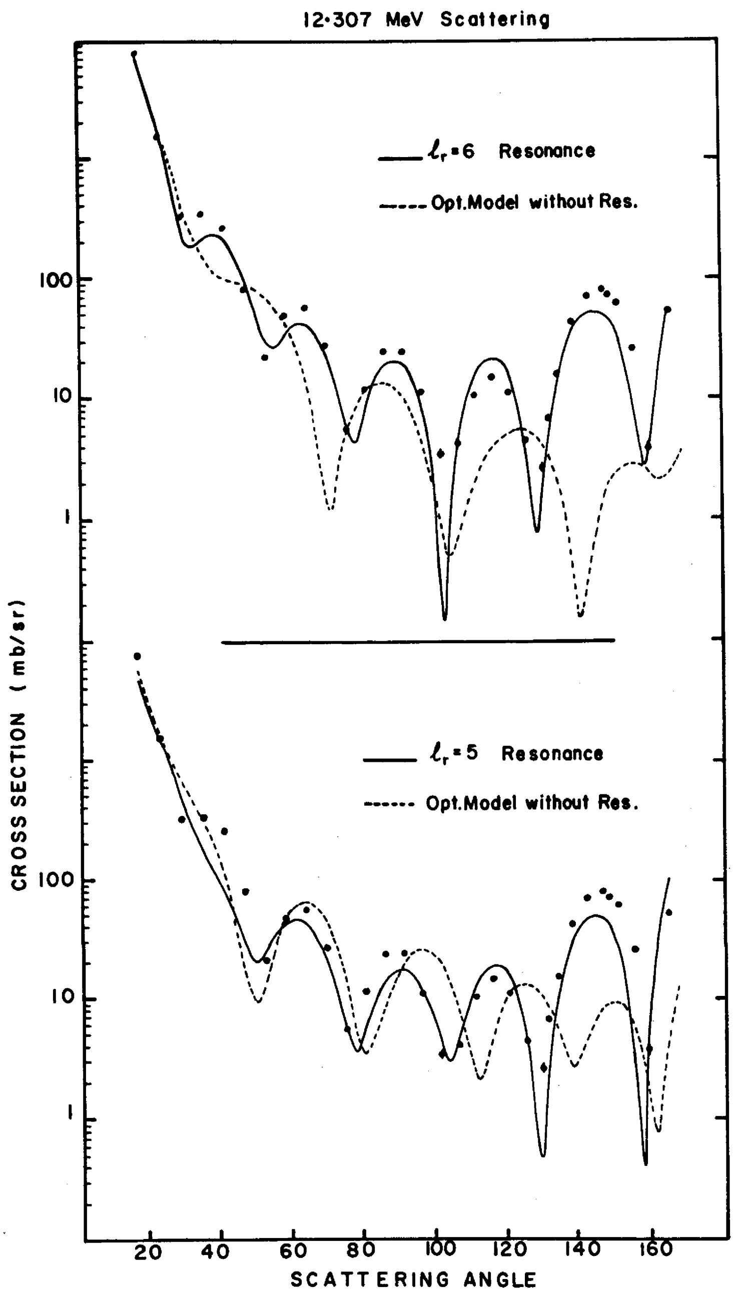

12·307 MeV Scattering
$\ell_r = 6$ Resonance
Opt.Model without Res.
$\ell_r = 5$ Resonance
Opt.Model without Res.
CROSS SECTION (mb/sr)
100
10
1
100
10
1
20
40
60
80
100
120
140
160
SCATTERING ANGLE

comparison with that for $\ell_r=6$ is seen to be in poorer agreement with the observed scattering at very forward angles.

An additional check on the possible ambiguity in the determination of an appropriate ℓ_r value was made by another application of an $\ell_r=0$ to 9 grid-and-search to the 12·307 MeV data; the starting parameters were those indicated in table 7.1 with the exception that successive values of Γ_α of 0·01, 0·5 and 0·8 were taken. The results of this procedure indicated that the χ^2 minima of table 7.1 were the most preferable both in terms of Γ_α and the specification of $\ell_r=5$ or 6; for ℓ_r other than these two values there was one χ^2 value of 160 while all others were in excess of 190 and correspondingly yielded very inadequate fits.

On the basis of the above results the grid-and-search procedure was applied to the elastic scattering distributions at 12·217, 12·257, 12·358 and 12·404 MeV with the grid taken for $\ell_r=4$ to 7 and with starting parameters corresponding to the $\ell_r=6$ set of table 7.1. The results of this procedure for the four distributions are given in table 7.2.

Some of the derived parameters of table 7.2, such as $\Gamma_\alpha>\Gamma$ and Γ_α and Γ of opposite sign, correspond to non-physical results; these χ^2 minima were accessible as the code contained no constraints on the sign or magnitude

Table 7.2

Incident Energy (MeV) Lab	C.Mass	Γ_α	Γ	E_r	V	W	r_0	a	χ^2	ℓ_r
		MeV					Fermi			
(Starting Values)		0·117	0·124	10·244	44·71	4·22	1·90	·46		
12·217	10·181	0·22	0·41	10·19	39·0	4·7	1·89	0·64	220	4
		0·14	-0·01	10·27	32·2	4·1	1·98	0·60	127	5
		0·11	0·14	10·19	40·7	3·4	1·88	0·57	111	6
		0·04	-0·05	10·25	53·9	15·9	1·91	0·61	224	7
12·257	10·214	0·05	-0·65	10·27	40·6	6·1	1·93	0·61	192	4
		0·22	0·12	10·25	41·3	3·5	1·91	0·72	97	5
		0·11	0·13	10·24	39·5	3·5	1·92	0·49	97	6
		0·11	0·12	10·26	52·2	7·4	1·92	0·69	175	7
12·357	10·298	-0·40	-0·50	10·25	39·3	3·6	1·89	0·69	210	4
		0·13	0·11	10·27	40·5	2·7	1·91	0·52	175	5
		0·11	0·12	10·25	39·8	4·8	1·91	0·47	110	6
		0·43	0·12	10·25	37·4	3·0	1·96	0·74	226	7
12·404	10·337	-0·09	-0·15	10·25	40·1	3·6	1·91	0·55	108	4
		0·25	0·12	10·25	41·7	3·5	1·91	0·56	129	5
		0·08	0·13	10·29	41·3	5·1	1·92	0·47	123	6
		-0·08	-0·19	10·21	37·4	4·6	1·94	0·61	135	7

of any of the parameters. A preference for $\ell_r=6$ is apparent from the non-physical parameters associated with most alternative ℓ_r values and more particularly from the associated χ^2 minima at each energy for $\ell_r=6$. The same $\ell_r=4$ to 7 grid procedure was reapplied to the above four distributions but with starting parameters corresponding to the $\ell_r=5$ set of table 7.1; an equivalent preference for $\ell_r=6$ was again apparent for the 12·217 and 12·404 MeV distributions while the preferred ℓ_r values for the 12·257 and 12·358 MeV distributions could only be restricted to either $\ell_r=5$ or 6. To some extent then the preference for $\ell_r=6$ in table 7.2 may have been predetermined by the starting parameters corresponding to the best $\ell_r=6$ fit at 12·307 MeV; however the results of table 7.2 are taken as complimentary to those of table 7.1 rather than as an independent indication of the appropriateness of an $\ell_r=5$ or 6 resonant amplitude at these energies.

With a value of $\ell_r=6$, indicated as the more appropriate assignment in table 7.1, an attempt was made to provide an overall description of the five distributions in terms of one set of parameters. The fits corresponding to the $\ell_r=6$ parameters of table 7.1 were found to be rather poor as might be expected from the range of deviations, mainly in V and E_r, of the best fit $\ell_r=6$ parameters of table 7.2 from the initial starting values. To find a more satisfactory description of the five distributions in terms of one set of parameters a grid search of resonant parameters for $\ell_r=6$ was performed for a fixed set of optical potential parameters. The required optical potential parameters were taken from an approximate average of the five sets associated with $\ell_r=6$ in tables 7.1 and 7.2 and the resonant parameters were considered for a grid of E_r values and combinations of Γ_α and Γ. The resulting fits were evaluated visually and the set of parameters ascertained as giving the best overall description of the five distributions is shown in table 7.3.

Table 7.3

	Γ_α	Γ	E_r	V	W	r_0	a
	MeV					fermi	
$\ell_r = 6$	0·12	0·13	10·23	41·0	4·0	1·90	0·46

The fits corresponding to the parameters of table 7.3 are shown in figure 7.2. In describing the five distributions in terms of one set of parameters it has been assumed that the resonant parameters are energy independent. Such an assumption is considered reasonable as the calculated penetration factors (see expression 7.3) for $\ell_r=6$ at channel radii of 5 and 6 fermi, the smaller value taken as a lower limit and corresponding to $r_0 \simeq 1{\cdot}9$, show a variation of <8% in the energy range 12·217 to 12·404 MeV; the penetration factors were calculated using

FIGURE 7.2

Optical model plus resonance fits (solid line) to elastic alpha scattering on ^{20}Ne at five energies (dots) in terms of the one set of parameters of table 7.3

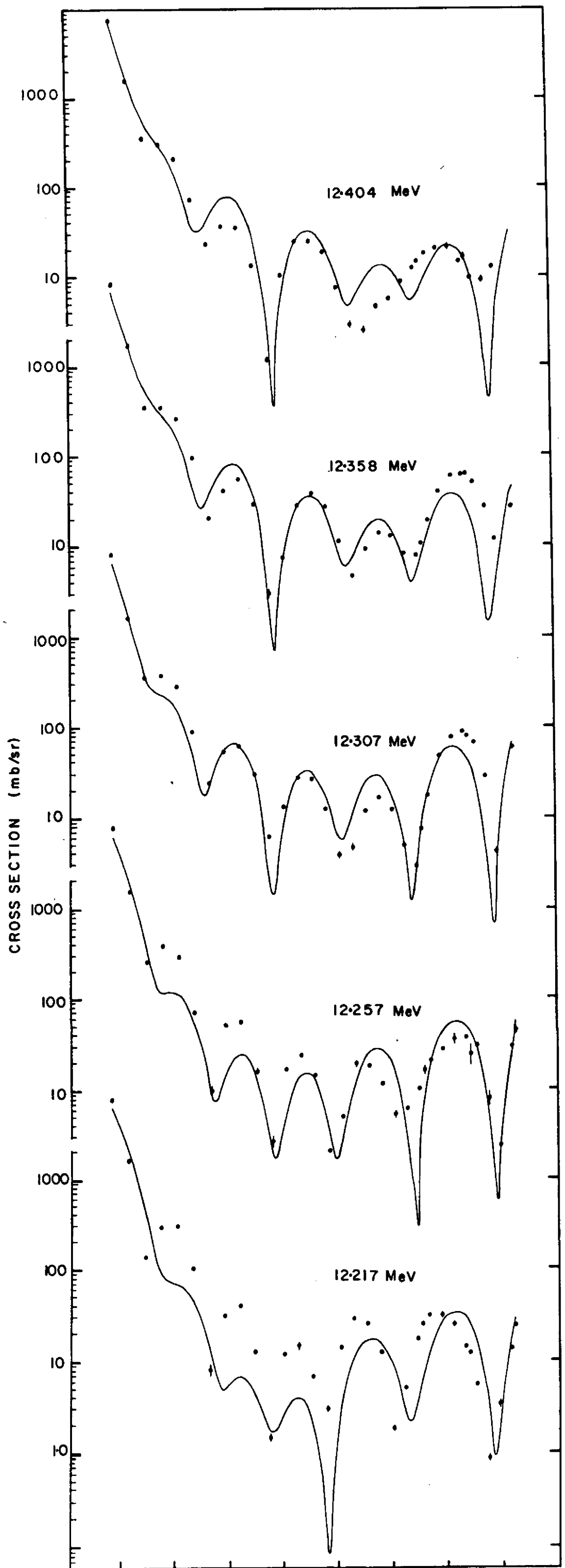
12·404 MeV
12·358 MeV
12·307 MeV
12·257 MeV
12·217 MeV
CROSS SECTION (mb/sr)
SCATTERING ANGLE
1000
100
10
1·0
20
40
60
80
100
120
140
160

the code HACOOL (Ha 66).

A comparison of χ^2 values obtained for the five distributions via :

(i) the optical model analysis considered in chapter five (Table 5.1(a));

(ii) the ℓ_r=5 and 6 parameters of table 7.1;

(iii) the ℓ_r=6 parameters of table 7.2; and

(iv) the ℓ_r=6 parameters of table 7.3

is made in table 7.4. According to the χ^2 criterion and as seen in figure 7.2, one fixed set of optical model and resonant parameters has provided a reasonably unified description of the three central energy distributions. The fits at 12·217 and 12·404 MeV are however poor; the comparison of the χ^2 values of (iv) and (i) above is of interest although not particularly valid as those of (i) correspond to differing optical potential parameters at each energy.

The fits in figure 7.2 at 12·217 and 12·257 MeV corresponding to centre of mass energies $<E_r$ of table 7.3, both show indications of destructive interference at forward angles, an effect which was more pronounced with increasing E_r; on the other hand at 12·358 and 12·404 MeV the cross section at forward angles is over-estimated and is indicative of constructive interference for energies $>E_r$. It is noted that an alternative overall description of the five distributions in terms of one set of parameters and for ℓ_r=5 had been considered in the preliminary analysis mentioned

Table 7.4

Energy (MeV)		χ^2				
		12·217	12·257	12·307	12·358	12·404
(i)	Optical Model Search : Table 5.1 (b)	260	170	250	220	120
(ii)	Optical Model plus Resonance Parameters for ℓ_r=5 and 6 at 12·307 MeV ; Table 7.1	1900 730	190 270	61 110	250 450	320 2100
(iii)	Optical Model plus Resonance Search for ℓ_r=6 at each energy : Table 7.2	111	97	61	110	123
(iv)	Optical Model plus Resonance Grid for ℓ_r=6 : Table 7.3	420	130	110	120	230

previously. Although the χ^2 values corresponding to the description adjudged visually as the most satisfactory, of 1400, 170, 110, 250 and 970 are quite inferior to corresponding $\ell_r=6$ values of table 7.4 (420, 130, 110, 120 and 230) the predicted cross sections were symmetric about the resonance energy.

It would appear from the above noted inadequacies in the fits at 12·217 and 12·404 MeV that the present model for scattering is too oversimplified to provide a unified description both on and off resonance. The results of the analysis as shown in tables 7.1 and 7.2 do indicate however that a description of the energy dependence in terms of one dominant resonance can be restricted to ℓ_r values of 5 or 6. The modification of the resonant amplitude by the phase factor $e^{i\phi}$, as considered in section 7.1, could perhaps provide a more unified description of all the distributions.

7.3 Interpretation of Optical Model plus Resonance Analysis

The analysis considered in this chapter has given a moderately successful description of data which as discussed in chapter five was not well fitted even at forward angles by the simpler optical model analysis. The justification for the addition of a Breit-Wigner resonant amplitude to an optical model amplitude is not rigorous but present indications of its appropriateness in defining an $\ell_r=5$ or 6 resonant amplitude are encouraging.

For spin zero on spin zero scattering a resonating partial wave ℓ_r, as discussed here, corresponds to the formation of a state in the compound system of spin $J=\ell_r$ and of natural parity. The present analysis suggests the existence of a 6^+ or 5^- state at an excitation of $\approx$19·5 MeV in ^{24}Mg; the partial width for decay or formation of this state via ^{20}Ne in its ground state and an alpha particle is indicated in table 7.1 to be almost the full width of decay of $\approx$120 kev.

The resonant structure under consideration corresponds to an excitation energy in ^{24}Mg of 19·57±·03 MeV which is approximately the energy of the excitation of the lowest of the states described as a ^{12}C-^{12}C quasimolecular resonance (Al 63). As noted in section 4.1 it was the possibility of some significance in this correspondence, initially indicated by the backward angle elastic scattering excitation functions, that motivated more detailed excitation functions and subsequent measurement of five angular distributions spanning the structure.

It is rather apparent from the spin assignment by Almqvist et al (Al 63) of 2^+ to the 19·58 MeV quasimolecular state and the proposed present assignment of 6^+ or 5^- to a resonance of corresponding width and excitation that the resonance effects seen in the $^{12}C+^{12}C$ and $^{20}Ne+\alpha$ scattering reflect the influence of different compound states. A further indication of the independence of the two resonant effects is apparent from the partial widths for decay of the 19·58 MeV (2^+) state to ^{20}Ne in its ground and excited states via alpha emission; Almqvist et al give :

$$\Gamma_{\alpha_0} < 1 \quad \text{kev}$$
$$\Gamma_{\alpha_1} = 18\cdot3 \text{ kev}$$
$$\Gamma_{\alpha_2} = 25\cdot5 \text{ kev}$$

These values indicate that the formation of the quasimolecular 2^+ state via alpha scattering on ^{20}Ne would be accompanied by resonance contributions to the 2^+ and 4^+ scattering enhanced by a factor of ≈20 over that in the elastic channel. It would not be expected that interference effects with potential scattering in each of the elastic and inelastic channels could obscure these differences in the partial widths and as such enhancement is not apparent in the integrated yields of figure 4.6, the above reference to two independent resonances appears valid.

The interpretation of the ^{12}C on ^{12}C scattering resonances in terms of quasimolecular states was based on the large reduced carbon widths apparent for these states (Al 63). By way of comparison the partial widths of table 7.1 reduced to a percentage of the single particle unit are of interest. The reduced width γ_α^2 for formation or decay of the proposed resonance via the elastic alpha scattering, regarding the alpha particle as a single entity, can be expressed as a percentage of single particle units by (Pr 62) :

$$\gamma_\alpha^2 = \frac{\Gamma_\alpha}{2P_\ell} \times \frac{100}{\hbar^2/2mR_0^2} \qquad (7\text{-}3)$$

where (i) P_ℓ is the penetration factor at radius R_0; and

(ii) m is the reduced mass of the ^{20}Ne and alpha masses.

With a value of R_0=5·15 fermi, corresponding to r_0=1·9 fermi, and Γ_α=120 kev expression (7-3) yields for the presently proposed resonance a value of :

(i) $\gamma_\alpha^2 \approx 18\%$ for the 6^+ assignment; and

(ii) $\gamma_\alpha^2 \approx 8\%$ for the 5^- assignment.

The penetration factors of expression (7-3) were evaluated using the code HACOOL (Ha 66).

The average reduced alpha widths determined at an equivalent radius for a range of nuclei ($A \leq 42$) and at excitations of ≈11 MeV were found to be typically <8% (Cl 60); the corresponding quantities for the two lower quasimolecular states were given as≈1%. The larger values then of 18% and to a lesser extent that of 8% are suggestive of a degree of alpha clustering in the resonant state. Such an interpretation is consistent with a description of the resonance energy dependence at ≈12·3 MeV in the elastic scattering as the influence of a single compound state which is distinguished from adjacent and possibly overlapping states such as the 2^+ quasimolecular state by a greater tendency to clustering of an alpha particle and ^{20}Ne in its ground state. Davis (Da 63) and Carter et al (Ca 64) have suggested that the resonance energy dependence of elastic alpha scattering on ^{12}C reflects the formation of alpha cluster states.

The probability for decay of the proposed resonance to channels other than the elastic channel is proportional to $(\Gamma-\Gamma_\alpha)$. If the estimate of $(\Gamma-\Gamma_\alpha)$ corresponding to the $\ell_r=6$ parameters of table 7.1 is assigned to the 2^+ scattering channel it is seen to be <10% of the width for decay to the elastic channel. The approximate equivalence in magnitude of the structure in the elastic and 2^+ integrated yields (figure 4.6) at ≈12·3 MeV relative to a background of scattering as defined by the trend from higher energy measurements is however not indicative of partial widths in the ratio of 10:1. If it is assumed that interference effects between resonant and direct scattering in each channel do not obscure a 10:1 difference in the resonance contributions the comment of section 4.3 that the structure in the 0^+ and 2^+ integrated yields at ≈12·3 MeV (figure 4.6) is uncorrelated appears to be supported.

In the excitation functions of differential cross section shown in figures 4.2(a), (b) and (c) there are the suggestions, in addition to that already discussed, of correlation of the energy dependence of the present measurements with quasimolecular excitations in ^{24}Mg. The elastic scattering excitation function at 91.4° (c.mass) displays resonance structure at 12·71 and 13·13 MeV ($\Delta E = \pm 30$ kev), energies which correspond to within 10 kev of the two quasi-molecular states at 19·91 (4^+) and 20·25 MeV. Little however can be said of such a correlation in the absence of angle integrated yields; the alpha width for formation of the 19·91 (4^+) state is comparable to that for the 19·58 (2^+) state, i.e. <1% of the full width and as such suggests that as in the resonance structure at ≈12·3 MeV the correlation is fortuitous and perhaps a further indication of multiplicity of available excitations in the compound system.

In summarizing this discussion it is considered that the present analysis indicates the presence of a 5^- or 6^+ state at an excitation of ≈19·5 MeV in ^{24}Mg. That such a resonance should be apparent in the present scattering is a reflection of its strong relation, possibly as a cluster state to the entrance channel. Since the analysis in terms of an optical model plus resonant amplitude has been found to show some success, it supports the approach of chapters five and six of anticipating an underlying direct interaction amplitude in the presently observed scattering.

CHAPTER 8

Conclusion

Experimentally the present studies have seen an expansion of the facilities of the laboratory in the use of negative helium ion injection into the tandem accelerator. The analyzed $^4He^{++}$ beams of 50 to 100 x 10^{-9} amps which became available as a matter of course were quite adequate for these scattering measurements.

The present results of elastic scattering add to the range of published results of alpha particle scattering on light nuclei at bombarding energies of <20 MeV; the in-elastic scattering, and particularly that from the 2^- state, complements a rather limited range of related measurements.

The spherical optical potential analysis of the angular distributions of elastic scattering has yielded a range of discrete potential well depths thereby exemplifying the well known potential ambiguity which does not appear to be resolved in elastic scattering analysis or indeed via a coupled channels calculation. The presently observed bias for a shallow real well depth in the four parameter fitting is interpreted as a function of the light mass of the target nucleus; a preference for a particular value of the real well depth was seen to be predetermined by the assignment of a fixed radius parameter. The indications of an average spherical potential and the qualitative description of approximately half of the number of measured elastic scattering distributions in terms of fluctuations in the potential strengths about these average values suggest that direct potential scattering significantly influences the elastic scattering. While allowing the potential strengths to vary it was possible to arrive at geometrical parameters similar to those employed in describing alpha particle scattering on near mass nuclei and at nearby energies; this is consistent with the usual application of the optical model in that at least the geometrical parameters are relatively insensitive to the mass of the target nucleus and energy of scattering.

The approximate description of the observed inelastic scattering via the coupled channels calculations suggests that direct collective excitation is important in defining the scattering from the 2^+ and 4^+ states. The poor description via the coupled channels calculations of the elastic scattering relative to that of the inelastic scattering indicates a greater complexity of interactions in the entrance channel although the source of complexity is not presently determined. It is considered that the improved quality of the fits to the elastic scattering via the spherical potential analysis reflects the ability to parameterize the scattering more readily than was possible in the coupled channels calculations in which any parameterization of the effect of non-direct scattering in a particular channel would be expected to be minimized.

The explicit treatment of the effects of non-direct scattering by the addition of a single Breit-Wigner amplitude to the optical model scattering amplitude appears to show some success in the description of scattering which is dominated by pronounced resonance behaviour. On interpreting the $\approx 12 \cdot 3$ MeV resonance structure of the elastic scattering as the influence of a single compound state in ^{24}Mg, the width of the state was seen to correspond to the width of adjacent quasimolecular states and the spin assignment of 5^- or 6^+ was possible. The ability to describe this energy dependent elastic scattering in terms of an optical model amplitude plus a Breit-Wigner amplitude is in agreement with the approach adopted throughout the present analysis of anticipating that direct scattering significantly influences scattering which is observed to show, in the resonance behaviour of the excitation functions, a more apparent influence of non-direct resonant processes.

Appendix I

Energy Loss Calculations

The stopping power in MeV/mgm/cm^2 of a wide range of materials for $^4He^{++}$ ions have been given by Williamson and Boujot (Wi 66).

(i) The formulation of Whaling (Wh 63) was used to obtain the stopping power of the compound mylar ($C_{10}H_8O_4$). The following expression was obtained :

$$\left(\frac{dE}{dX}\right)_{C_{10}H_8O_4} = \frac{10\ M_C\left(\frac{dE}{dX}\right)_C + 8\ M_H\left(\frac{dE}{dX}\right)_H + 4\ M_O\left(\frac{dE}{dX}\right)_O}{10\ M_C + 8\ M_H + 4\ M_O}$$

where subscripted M refers to the atomic mass of the respective elemental components. The values obtained from this expression agreed to within 5% of the values obtained from more generalized and less detailed tables of Barkas and Berger (Ba 64).

(ii) A linear least squares code of the author was used to fit the polynomial

$$\left(\frac{dE}{dX}\right)^{-1} = C_0 + C_1E + C_2E^2 + C_3E^3$$

for all materials acting as absorbers. The separate set of four coefficients were used for each energy loss calculation via numerical solution of the following equation :

$$\int_0^{E_a} \left(\frac{dE}{dX}\right)^{-1} dE \; + \; t \; = \; \int_0^{E_i} \left(\frac{dE}{dX}\right)^{-1} dE$$

where (a) E_i is the energy prior to the absorber;

(b) E_a is the energy after passage through the absorber; and

(c) t is the thickness of the absorber.

The solution to this equation was obtained upon iterative application of Newton's approximation. The code for these calculations was incorporated in the kinematics and data reduction codes of the author.

(iii) The mylar foil as used in the gas cell windows was aluminized on one side. For the purposes of the calculations, this was ignored and the mylar was ascribed the thickness of 0·567 mgm/cm^2 obtained by weighing a large area sample.

(iv) The stopping power of mylar for $^4He^{++}$ ions as well as the stopping power coefficients for $^4He^{++}$ in neon, mylar and nickel are tabulated below. The coefficients yield mgm/cm^2/MeV for E given in MeV.

(a)

ENERGY ($^4He^{++}$) MeV	dE/dX (MYLAR) $MeV/mgm/cm^2$	ENERGY MeV	dE/dX (MYLAR) $MeV/mgm/cm^2$
1	2·327	9	0·542
2	1·583	10	0·498
3	1·215	11	0·464
4	0·992	12	0·434
5	0·843	13	0·408
6	0·734	14	0·384
7	0·664	15	0·365
8	0·591		

(b)

COEFFICIENTS	C_0	C_1	C_2	C_3
Mylar	0·2293	0·2079	-0·0038	0·00007
Neon	0·3884	0·2281	-0·0038	0·00008
Nickel	1·1140	0·2371	-0·0011	-0·00001

APPENDIX II

Tabulation of ≈100 kev
Excitation Function Measurements
as listed in table 4.1

0(+) SCATTERING
C.MASS ANGLE= 47.41

ENERGY (LAB)	C.SECT MB/SR (C.MASS)	% ERROR REL
11.71	113.853	0.6
11.81	62.548	1.0
11.91	84.260	0.7
12.01	145.109	0.5
12.11	109.955	0.6
12.21	72.928	0.7
12.32	83.773	0.7
12.42	69.512	0.7
12.52	74.647	0.8
12.62	59.807	0.7
12.72	88.687	0.4
12.82	54.652	0.9
12.92	50.795	0.8
13.02	62.188	0.8
13.13	73.885	0.7
13.23	82.035	0.7
13.33	115.811	0.6
13.43	110.809	0.6
13.53	67.449	0.8
13.63	70.590	0.8
13.71	50.016	0.8
13.81	53.967	1.0
13.92	53.085	1.0
14.02	19.943	1.6
14.12	34.809	1.7
14.22	26.081	1.4
14.32	37.485	1.3
14.42	19.839	1.9
14.52	9.444	2.7
14.62	11.657	3.1
14.73	4.267	3.9
14.83	11.600	2.5
14.93	31.907	1.6
15.03	19.540	0.9
15.13	2.411	2.7
15.23	15.809	1.0

2(+) SCATTERING
LAB ANGLE= 40.00

ENERGY (LAB)	C.SECT MB/SR (LAB)	% ERROR REL
11.71	51.371	1.3
11.81	19.133	2.2
11.91	14.567	2.4
12.01	11.530	2.8
12.11	4.450	5.2
12.21	9.604	3.1
12.32	22.681	2.0
12.42	57.749	1.2
12.52	54.713	1.2
12.62	34.240	1.5
12.72	36.260	1.2
12.82	37.813	1.4
12.92	36.845	1.5
13.02	27.097	2.1
13.13	34.302	1.5
13.23	25.949	2.0
13.33	34.680	1.8
13.43	33.541	1.9
13.53	35.090	1.8
13.63	32.684	1.7
13.71	37.630	1.3
13.81	33.541	1.7
13.92	24.818	2.0
14.02	32.602	1.7
14.12	31.326	1.8
14.22	39.483	1.6
14.32	28.250	2.3
14.42	32.907	2.1
14.52	36.776	2.0
14.62	51.090	1.7
14.73	67.100	1.5
14.83	50.475	1.7
14.93	50.120	1.7
15.03	22.649	1.5
15.13	14.235	1.9
15.23	53.762	1.0

4(+) SCATTERING
LAB ANGLE= 40.00

ENERGY (LAB)	C.SECT MB/SR (LAB)	% ERROR REL
11.71	13.063	2.6
11.81	10.035	3.0
11.91	17.855	2.1
12.01	22.113	1.8
12.11	12.004	2.7
12.21	10.247	3.0
12.32	17.657	2.1
12.42	8.490	9.6
12.52	11.074	2.8
12.62	13.706	2.4
12.72	5.380	3.2
12.82	10.011	2.9
12.92	24.417	1.8
13.02	8.804	3.6
13.13	5.797	5.0
13.23	9.716	3.4
13.33	14.227	2.9
13.43	17.572	2.5
13.53	17.263	2.5
13.63	9.534	3.5
13.71	12.754	2.4
13.81	13.681	2.3
13.92	26.058	2.0
14.02	25.921	1.9
14.12	16.378	2.4
14.22	12.104	2.9
14.32	19.600	2.7
14.42	15.189	3.1
14.52	17.130	3.0
14.62	11.621	3.6
14.73	4.033	6.2
14.83	7.533	4.4
14.93	16.720	2.9
15.03	15.512	2.5
15.13	9.531	2.1
15.23	20.490	1.5

2(-) SCATTERING
LAB ANGLE= 40.00

ENERGY (LAB)	C.SECT MB/SR (LAB)	% ERROR REL
13.43	0.665	24.8
13.53	1.650	9.7
13.63	7.547	4.0
13.71	4.222	5.4
13.81	1.996	15.7
13.92	0.720	18.5
14.02	2.661	7.3
14.12	4.430	5.7
14.22	1.723	9.5
14.32	3.682	7.5
14.42	6.125	5.2
14.52	4.949	6.1
14.62	6.822	5.0
14.73	7.478	4.7
14.83	1.969	9.4
14.93	2.064	9.4
15.03	1.718	5.7
15.13	1.520	11.6
15.23	5.112	3.6

3(-),1(-) SCATTERING
LAB ANGLE= 40.00

ENERGY (LAB)	C.SECT MB/SR (LAB)	% ERROR REL
12.32	23.119	3.0
12.42	21.498	3.7
12.52	21.492	3.7
12.62	28.033	4.0
12.72	16.245	5.2
12.82	17.265	5.1
12.92	13.795	6.6
13.02	12.715	10.6
13.13	6.357	11.9
13.23	9.424	10.6
13.33	11.575	3.3
13.43	12.733	3.1
13.53	19.660	2.4
13.63	18.056	2.4
13.71	22.553	1.8
13.81	25.356	2.2
13.92	14.984	3.0
14.02	17.509	2.4
14.12	11.648	3.1
14.22	9.133	3.6
14.32	3.533	7.2
14.42	2.680	9.4
14.52	3.896	9.3
14.62	8.859	4.3
14.73	15.996	3.2
14.83	14.615	3.2
14.93	13.330	3.5
15.03	9.902	2.1
15.13	2.772	6.8
15.23	6.160	3.1

0(+) SCATTERING
C.MASS ANGLE= 91.40

ENERGY (LAB)	C.SECT MB/SR (C.MASS)	% ERROR REL
11.71	4.630	4.6
11.81	3.161	5.2
11.91	9.215	3.0
12.01	5.429	3.6
12.11	0.807	10.2
12.21	7.509	3.4
12.32	32.503	1.6
12.42	21.202	2.0
12.52	19.403	2.1
12.62	6.536	3.6
12.72	16.177	1.8
12.82	4.449	4.5
12.92	2.095	6.9
13.02	6.490	4.2
13.13	12.748	2.6
13.23	7.170	4.0
13.33	8.591	3.7
13.43	14.055	2.8
13.53	19.766	2.7
13.63	30.050	2.0
13.71	21.573	1.8
13.81	18.690	2.5
13.92	4.079	5.4
14.02	8.739	3.6
14.12	21.558	2.3
14.22	22.917	2.2
14.32	25.701	2.6
14.42	47.596	1.9
14.52	53.492	1.8
14.62	52.916	1.8
14.73	35.209	2.2
14.83	11.904	3.9
14.93	9.882	4.3
15.03	18.227	1.6
15.13	14.510	2.0
15.23	1.135	6.2

2(+) SCATTERING
LAB ANGLE= 80.00

ENERGY (LAB)	C.SECT MB/SR (LAB)	% ERROR REL
11.71	16.044	2.8
11.81	23.787	2.1
11.91	25.726	2.0
12.01	12.583	3.1
12.11	8.702	3.8
12.21	11.986	3.3
12.32	9.287	3.6
12.42	8.790	3.8
12.52	8.946	3.5
12.62	24.440	2.1
12.72	15.382	1.9
12.82	7.779	3.6
12.92	9.452	3.6
13.02	9.095	4.4
13.13	9.940	3.2
13.23	5.197	5.3
13.33	9.186	3.9
13.43	9.966	3.9
13.53	7.887	4.3
13.63	9.082	3.9
13.71	4.368	4.3
13.81	8.082	4.1
13.92	9.095	3.9
14.02	10.771	3.5
14.12	12.876	3.3
14.22	3.495	6.5
14.32	1.428	12.5
14.42	3.021	8.8
14.52	6.081	5.9
14.62	7.328	5.3
14.73	6.100	6.3
14.83	3.722	7.7
14.93	2.027	10.7
15.03	2.386	4.8
15.13	5.377	3.2
15.23	4.368	3.5

4(+) SCATTERING
LAB ANGLE= 80.00

ENERGY (LAB)	C.SECT MB/SR (LAB)	% ERROR REL
11.71	13.217	3.0
11.81	11.002	3.1
11.91	5.087	4.9
12.01	6.300	3.9
12.11	7.513	3.8
12.21	8.264	3.6
12.32	9.638	3.4
12.42	5.652	4.4
12.52	4.755	4.7
12.62	7.932	3.7
12.72	7.791	2.7
12.82	13.212	2.8
12.92	16.566	2.5
13.02	9.459	4.0
13.13	16.829	2.6
13.23	18.931	2.7
13.33	15.111	4.8
13.43	6.159	10.4
13.53	13.279	5.3
13.63	6.522	9.8
13.71	11.156	5.3
13.81	7.029	9.1
13.92	7.120	9.0
14.02	9.706	6.9
14.12	4.509	13.8
14.22	3.469	7.3
14.32	4.187	7.1
14.42	4.405	7.0
14.52	5.165	6.4
14.62	6.081	5.8
14.73	9.121	4.7
14.83	13.389	3.9
14.93	10.173	4.5
15.03	9.638	2.4
15.13	12.644	2.1
15.23	8.573	2.5

2(-) SCATTERING
LAB ANGLE= 80.00

ENERGY (LAB)	C.SECT MB/SR (LAB)	% ERROR REL
11.91	1.958	10.5
12.01	1.021	11.6
12.11	0.857	14.4
12.21	1.783	9.9
12.32	2.300	7.6
12.42	0.984	12.2
12.52	0.906	11.8
12.62	2.027	7.7
12.72	1.452	7.9
12.82	1.151	10.2
12.92	0.974	19.5
13.02	1.988	9.6
13.13	1.754	9.7
13.23	6.341	4.2
13.33	2.857	7.5
13.43	3.196	6.9
13.53	1.585	10.8
13.63	0.728	17.5
13.71	0.935	10.8
13.81	0.247	36.1
13.92	0.377	27.6
14.02	0.780	19.7

3(-),1(-) SCATTERING
LAB ANGLE= 80.00

ENERGY (LAB)	C.SECT MB/SR (LAB)	% ERROR REL
12.62	6.987	4.2
12.72	7.060	3.0
12.82	10.162	5.5
12.92	11.362	3.1
13.02	5.730	5.0
13.13	6.617	4.2
13.23	7.471	4.6
13.33	6.574	4.9
13.43	6.029	5.8
13.53	7.120	4.5
13.63	7.471	4.6
13.71	6.582	3.6
13.81	8.588	4.1
13.92	7.380	4.4
14.02	5.808	5.3
14.22	3.391	7.5
14.32	2.470	10.2
14.42	1.676	13.2
14.52	1.851	12.3
14.62	3.118	8.9
14.73	2.729	12.5
14.83	3.698	8.9
14.93	4.210	8.5

0(+) SCATTERING
C.MASS ANGLE=155.76

ENERGY (LAB)	C.SECT MB/SR (C.MASS)	% ERROR REL
11.71	8.113	4.4
11.81	14.537	3.2
11.91	8.912	4.1
12.01	1.977	7.8
12.11	3.768	6.3
12.32	28.494	2.3
12.42	3.186	7.7
12.62	6.996	6.3
12.72	2.789	10.3
12.82	6.026	6.8
12.92	9.330	5.0
13.02	3.386	13.9
13.13	3.668	10.4
13.23	5.785	7.7
13.33	1.074	36.0
13.43	0.274	103.5
13.53	1.144	28.6
13.63	1.207	27.2
13.71	2.309	13.3
13.81	0.721	15.9
13.92	10.935	4.0
14.02	6.922	5.0
14.12	9.830	4.2
14.22	13.217	3.6
14.32	5.786	6.7
14.42	0.776	18.2
14.52	0.741	18.6
14.62	5.797	6.6
14.73	5.727	6.7
14.83	6.762	6.2
14.93	5.527	6.8

0(+) SCATTERING
C.MASS ANGLE= 70.01

ENERGY (LAB)	C.SECT MB/SR (C.MASS)	% ERROR REL
13.23	10.079	2.8
13.33	15.701	2.6
13.43	14.378	2.1
13.53	15.578	3.1
13.63	20.758	3.0
13.71	11.372	3.0
13.82	6.333	5.0
13.92	13.924	4.4
14.02	3.277	6.8
14.12	9.052	3.6
14.22	7.987	4.1
14.32	18.392	2.7
14.42	11.579	4.8
14.52	8.067	8.6
14.62	11.425	1.5
14.73	7.337	2.7
14.83	2.672	4.8
14.93	1.624	7.2
15.03	1.714	3.8
15.13	2.919	2.9
15.23	3.417	2.7

2(-) SCATTERING
LAB ANGLE= 60.00

ENERGY (LAB)	C.SECT MB/SR (LAB)	% ERROR REL
13.53	1.173	8.3
13.63	1.077	8.8
13.71	0.318	22.6
13.82	0.566	10.0
13.92	1.098	7.6
14.02	2.916	4.1
14.12	2.615	4.5
14.22	2.036	5.1
14.32	2.925	4.4
14.42	1.492	6.5
14.52	0.478	15.2
14.62	1.925	5.1
14.73	2.507	6.7
14.83	2.070	8.0
14.93	0.587	39.1
15.03	0.805	11.1
15.13	3.541	3.9
15.23	2.305	7.1

4(+) SCATTERING
LAB ANGLE= 60.00

ENERGY (LAB)	C.SECT MB/SR (LAB)	% ERROR REL
13.23	18.898	2.2
13.33	8.867	3.3
13.43	5.498	3.3
13.53	10.417	2.1
13.63	6.017	2.8
13.71	13.015	1.9
13.82	9.877	2.1
13.92	16.548	1.6
14.02	12.743	1.9
14.12	8.971	2.2
14.22	2.003	5.6
14.32	8.297	2.4
14.42	16.665	1.6
14.52	16.118	1.7
14.62	7.129	2.8
14.73	13.162	2.5
14.83	17.079	2.3
14.93	20.807	2.7
15.03	21.773	1.4
15.13	20.298	1.5
15.23	27.137	1.3

APPENDIX III

Tabulation of $\approx$25 kev
Excitation Function Measurements
as listed in table 4.2

ENERGY (LAB)	0(+) SCATTERING C.MASS ANGLE= 91.40		2(+) SCATTERING LAB ANGLE= 80.00		4(+) SCATTERING LAB ANGLE= 80.00		2(-) SCATTERING LAB ANGLE= 80.00	
	C.SECT MB/SR (C.MASS)	% ERROR REL	C.SECT MB/SR (LAB)	% ERROR REL	C.SECT MB/SR (LAB)	% ERROR REL	C.SECT MB/SR (LAB)	% ERROR REL
12.045	6.362	3.8	12.788	3.0	6.342	4.1		
12.070	7.031	3.7	11.792	3.1	4.759	4.8		
12.096	5.086	4.3	11.216	3.1	4.392	5.0		
12.121	1.276	8.6	9.906	3.3	6.247	4.2		
12.146	0.8C8	10.7	8.627	3.6	8.C19	3.7		
12.171	1.958	7.0	8.874	3.5	6.269	4.1		
12.196	4.029	4.8	9.549	3.4	5.797	4.3		
12.221	6.644	3.8	13.818	2.4	7.506	3.7		
12.247	9.643	3.1	13.375	2.9	9.927	3.3		
12.272	13.961	2.6	14.434	2.7	11.425	3.1		
12.297	22.188	2.0	13.763	2.8	12.935	2.9		
12.322	30.659	1.1	10.096	2.4	11.333	2.0		
12.348	35.083	1.6	5.933	4.3	8.4C7	3.5		
12.373	3C.764	1.7	5.755	4.4	7.599	3.8		
12.398	25.419	1.9	7.044	4.0	7.903	3.7		
12.423	22.163	1.4	9.439	2.4	7.212	2.7		
12.448	22.553	1.8	9.166	3.1	5.124	4.2		
12.474	20.782	1.9	8.327	3.2	4.679	4.3		
12.499	21.061	1.3	8.214	2.3	4.075	3.2		
12.524	21.388	1.3	9.094	2.2	4.960	2.9		
12.549	18.824	1.4	11.325	2.1	5.564	2.8		
12.575	13.901	1.6	15.337	1.7	6.859	2.5		
12.600	6.781	2.3	20.247	1.5	7.815	2.4		
12.625	4.563	2.8	23.912	1.4	8.046	4.1		
12.650	9.374	3.1	25.471	2.1	7.935	3.7		
12.676	16.175	2.4	25.786	2.1	6.625	4.0		
12.701	20.316	2.5	23.102	2.5	6.247	4.8		
12.726	20.556	2.4	18.728	2.9	7.463	4.4		
12.751	16.C48	2.8	12.942	3.5	8.637	4.1		
12.776	11.727	3.2	8.0C8	4.4	11.349	3.6	1.328	12.8
12.802	7.885	3.9	5.926	5.0	12.956	3.3	1.216	12.3
12.827	6.316	4.4	5.898	5.0	13.571	3.2	1.132	12.2
12.852	2.912	6.4	9.154	4.0	15.01C	3.1	C.797	15.7
12.877	2.646	6.7	10.426	3.7	17.233	2.9	0.643	16.8
12.903	3.654	4.4	1C.323	3.0	18.817	2.1	0.679	12.4
12.928	3.187	3.4	10.004	2.2	17.35C	1.6	C.906	9.0
12.953	3.973	3.0	15.761	1.7	24.868	1.3	1.564	6.7
12.978	3.077	4.1	12.483	2.3	12.387	2.2	1.977	6.1
13.003	5.273	3.7	12.537	2.7	1C.499	2.9	2.004	7.0
13.029	6.693	3.3	10.960	2.8	9.132	3.1	2.C29	6.7
13.054	8.265	2.1	10.755	1.9	12.5C7	1.7	1.849	5.2
13.079	11.141	1.8	10.755	2.0	12.507	1.8	1.849	5.2
13.104	13.801	2.3	10.633	2.9	14.75C	2.4	1.769	7.3
13.129	13.498	2.3	1C.960	2.8	17.182	2.2	1.845	7.4
13.155	13.714	2.3	9.585	3.1	19.580	2.1	2.759	5.8
13.180	12.469	2.4	8.31C	3.3	20.654	2.0	3.774	4.9
13.205	9.254	2.8	6.272	3.8	21.652	2.0	4.407	4.5
13.230	7.699	3.1	5.820	3.9	19.253	2.1	4.948	4.2
13.256	7.487	2.2	5.342	2.9	19.C77	1.5	5.421	2.8
13.281	6.223	2.7	6.378	2.9	19.140	1.7	5.241	3.2
13.306	6.033	3.9	7.757	3.7	18.029	2.4	4.696	4.8
13.332	8.4C7	3.3	9.769	3.3	15.6C8	2.6	3.428	5.6
13.357	11.262	3.3	1C.007	3.8	14.675	3.1	2.865	7.1
13.382	15.252	2.8	10.482	3.8	12.215	3.4	2.348	7.9
13.407	15.238	2.8	10.79C	3.6	9.001	4.0	2.697	7.3
13.432	15.225	2.8	11.684	3.5	6.764	4.6	2.991	6.9
13.457	13.909	2.9	10.915	3.7	6.736	4.6	3.201	6.7

ENERGY (LAB)	0(+) SCATTERING C.MASS ANGLE=130.00		2(+) SCATTERING LAB ANGLE=120.00		4(+) SCATTERING LAB ANGLE=120.00	
	C.SECT MB/SR (C.MASS)	% ERROR REL	C.SECT MB/SR (LAB)	% ERROR REL	C.SECT MB/SR (LAB)	% ERROR REL
12.045	9.920	4.3	9.380	3.2		
12.070	14.165	3.6	11.197	2.9		
12.096	13.520	3.7	11.141	2.9		
12.121	12.641	3.8	12.352	2.8		
12.146	13.884	3.7	11.234	2.9		
12.171	17.099	3.3	11.806	3.1		
12.196	19.290	3.1	13.414	2.7		
12.221	16.698	3.3	11.709	3.0		
12.247	13.368	3.7	10.684	3.1		
12.272	8.560	4.7	10.666	3.4		
12.297	3.694	7.1	12.194	3.0		
12.322	3.260	4.8	15.750	1.7		
12.348	7.810	4.9	21.527	2.5		
12.373	10.999	4.1	27.945	1.9		
12.398	12.055	3.9	29.808	2.0		
12.423	13.497	2.6	26.958	1.4		
12.448	12.683	3.4	23.797	1.8		
12.474	9.738	3.9	20.374	2.1		
12.499	5.221	3.8	19.014	1.5		
12.524	2.739	5.2	17.303	1.8		
12.549	2.345	5.6	18.947	1.7		
12.575	2.533	5.4	20.541	1.6		
12.600	3.110	4.9	17.188	2.1		
12.625	3.767	4.4	12.881	3.4		
12.650	6.356	5.4	12.082	3.2		
12.676	9.452	4.4	13.972	3.7		
12.701	6.442	6.2	15.078	3.8		
12.726	2.674	9.6	14.047	4.0		
12.751	1.126	14.8	14.035	3.5		
12.776	0.453	23.4	15.873	3.1		
12.802	0.719	18.6	14.656	3.4		
12.827	1.126	14.8	13.861	3.5	21.747	2.5
12.852	2.267	10.5	9.501	4.5	22.344	2.4
12.877	1.345	13.6	9.650	4.5	18.394	2.6
12.903	1.004	12.2	11.946	3.6	15.597	2.2
12.928	1.304	7.6			14.073	1.7
12.953	1.684	6.6			17.106	1.5
12.978	1.290	9.1			19.455	1.7
13.003	1.342	10.5			19.770	2.0
13.029	1.933	8.8			17.609	2.1
13.054	0.826	9.5			16.830	1.5
13.079	0.450	12.8			16.353	1.6
13.104	0.685	14.7			16.052	2.2
13.129	0.938	12.6			15.903	2.2
13.155	1.051	11.9			16.312	2.2
13.180	1.642	9.5			16.290	2.2
13.205	2.055	8.5			15.917	2.3
13.230	1.023	12.1			12.655	2.5
13.256	0.361	14.3			9.885	2.0
13.281	0.188	22.3			7.582	2.6
13.306	0.305	24.7			7.974	3.5
13.332	1.290	12.0			9.818	3.1
13.357	1.970	11.2			9.352	3.7
13.382	2.752	9.5			9.290	3.7
13.407	2.299	10.4			9.750	3.6
13.432	2.471	10.0			10.222	3.7
13.457	2.971	9.1			9.563	3.8

ENERGY (LAB)	O(+) SCATTERING C.MASS ANGLE=147.41 C.SECT MB/SR (C.MASS)	% ERROR REL	O(+) SCATTERING C.MASS ANGLE=163.93 C.SECT MB/SR (C.MASS)	% ERROR REL
12.045	20.200	3.1	34.127	1.9
12.070	24.404	2.8	30.048	2.1
12.096	27.748	2.7	24.444	2.5
12.121	27.983	2.6	23.397	4.3
12.146	23.729	2.9	24.078	2.4
12.171	22.156	2.9	24.286	2.3
12.196	17.022	3.4	16.512	2.9
12.221	14.016	3.8	13.018	3.1
12.247	25.577	2.8	22.294	2.4
12.272	53.531	1.9	29.300	2.1
12.297	82.443	1.5	27.454	2.2
12.322	83.245	1.0	19.471	1.6
12.348	57.706	1.8	15.010	3.1
12.373	29.205	2.6	17.915	2.7
12.398	14.813	3.6	22.477	2.4
12.423	8.585	3.4	20.088	1.8
12.448	5.561	5.3	14.279	2.8
12.474	4.662	5.8	7.800	3.9
12.499	5.315	3.8	2.716	4.5
12.524	6.277	3.5	0.880	7.6
12.549	5.030	3.9	3.281	4.1
12.575	5.663	3.7	13.824	2.0
12.600	19.129	2.0	33.301	1.3
12.625	40.726	1.4	44.434	1.1
12.650	40.039	2.2	39.018	1.8
12.676	22.713	2.9	25.720	2.3
12.701	15.696	4.1	16.127	3.3
12.726	11.342	4.8	12.372	4.0
12.751	15.475	4.1	9.749	4.4
12.776	19.308	3.7	5.321	6.1
12.802	18.838	3.7	3.038	8.4
12.827	14.067	4.3	1.803	13.5
12.852	8.670	5.5	1.353	20.3
12.877	11.329	4.8	3.562	8.4
12.903	16.779	3.0	9.765	3.7
12.928	20.623	1.9	15.226	1.9
12.953	17.479	2.1	17.188	1.8
12.978	14.974	2.7	18.695	2.0
13.003	14.870	3.2	19.610	2.3
13.029	15.246	3.2	19.592	2.4
13.054	15.156	2.3	16.226	1.8
13.079	12.113	2.5	10.033	2.3
13.104	8.933	4.3	7.814	3.7
13.129	8.808	4.2	10.297	3.2
13.155	11.194	3.7	14.355	2.8
13.180	14.886	3.2	16.257	2.5
13.205	17.796	3.0	13.566	2.8
13.230	13.986	3.3	8.045	3.6
13.256	5.933	3.6	3.621	3.9
13.281	4.200	4.8	2.713	5.1
13.306	7.236	5.2	3.914	7.2
13.332	11.020	4.2	6.397	4.7
13.357	12.307	4.6	8.470	4.7
13.382	9.713	5.2	9.919	4.5
13.407	6.336	6.4	9.232	4.5
13.432	3.338	8.8	6.497	5.4
13.457	1.617	12.7	5.322	5.8

APPENDIX IV

Tabulation of Angular
Distribution Measurements
at the energies of table 4.3

INCIDENT ENERGY= 11.674MEV

0(+) SCATTERING

ANGLE C.MASS	C.SECT MB/SR	% ERROR REL
17.98	7126.375	4.0
23.94	2151.821	4.0
29.87	445.299	4.0
35.76	84.678	4.0
41.61	118.822	4.0
47.41	131.435	6.7
53.16	66.658	4.0
58.84	17.579	5.2
64.46	1.529	12.6
70.01	6.210	4.0
75.48	6.943	16.7
80.87	7.764	14.1
86.18	8.023	4.0
91.40	7.474	4.0
96.53	8.047	4.0
101.57	5.870	4.0
106.53	4.219	4.6
111.39	3.754	4.0
116.17	5.612	4.1
120.87	8.686	4.0
125.47	11.571	4.0
130.00	12.709	9.8
134.46	12.875	4.0
138.84	11.159	5.0
143.15	7.962	4.8
147.41	5.138	4.0
151.61	5.145	4.0
155.76	7.381	4.0
159.86	24.014	4.0
163.93	44.171	4.0

2(+) SCATTERING

ANGLE C.MASS	C.SECT MB/SR	% ERROR REL
18.26	26.084	15.9
24.31	22.995	6.8
30.33	25.130	4.0
36.31	30.693	4.0
42.25	39.669	4.4
48.13	45.307	4.0
53.95	41.647	4.0
59.70	32.461	4.0
65.38	21.703	6.2
70.98	19.970	4.0
76.50	24.832	4.0
81.92	31.349	4.0
87.26	33.494	4.5
92.51	27.496	4.0
97.65	18.664	4.0
102.70	14.661	4.0
107.65	13.400	4.0
112.50	16.663	4.0
117.26	18.210	4.0
121.92	19.456	4.0
126.49	16.330	4.0
130.97	13.944	4.0
135.37	14.823	4.0
139.69	18.157	4.0
143.94	26.680	4.0
148.12	35.751	4.0
152.24	41.920	4.0
156.31	45.811	4.0

4(+) SCATTERING

ANGLE C.MASS	C.SECT MB/SR	% ERROR REL
18.97	18.402	16.5
25.24	17.179	5.6
31.48	17.118	4.0
37.68	16.832	4.0
43.82	16.850	4.0
49.89	14.874	4.0
55.89	13.615	4.0
61.81	12.245	4.0
67.64	11.767	4.0
73.38	11.910	4.0
79.01	13.143	4.0
84.54	14.490	4.0
89.95	14.930	4.0
95.25	15.481	4.0
100.43	16.565	4.0

INCIDENT ENERGY= 12.217MEV

0(+) SCATTERING

ANGLE C.MASS	C.SECT MB/SR	% ERROR REL
17.98	7233.293	4.0
23.94	1558.267	4.0
29.87	135.204	6.7
35.76	288.349	4.0
41.61	294.981	4.0
47.41	99.768	5.0
53.16	7.930	15.7
58.84	30.995	6.2
64.46	39.655	4.0
70.01	12.496	4.0
75.48	1.463	10.0
80.87	11.833	5.7
86.18	14.573	8.5
91.40	6.634	4.0
96.53	2.976	8.3
101.57	13.739	4.0
106.53	27.774	4.1
111.40	24.550	4.0
116.17	12.236	4.9
120.87	1.810	9.4
125.48	4.891	4.0
130.00	16.584	4.0
131.79	24.015	4.0
134.46	29.534	4.3
138.84	30.281	8.5
143.15	23.906	7.6
147.41	13.428	4.0
149.09	11.588	4.0
151.61	5.290	4.0
155.76	0.851	7.8
159.86	3.225	9.6
163.93	13.162	4.0
165.55	22.793	6.9

2(+) SCATTERING

ANGLE C.MASS	C.SECT MB/SR	% ERROR REL
18.25	40.973	8.9
24.30	55.725	4.0
30.31	61.882	4.0
36.29	37.040	4.0
42.22	14.102	4.6
48.09	4.758	16.7
53.91	10.967	8.3
59.66	14.483	13.0
65.33	14.632	4.0
70.93	10.563	8.5
76.45	9.503	4.0
81.87	9.204	6.9
87.21	10.883	4.0
92.45	10.842	4.0
97.60	8.388	4.8
102.64	6.869	4.0
107.60	7.500	4.0
112.45	11.962	4.0
117.21	17.066	4.0
121.87	20.783	4.0
126.44	20.438	4.0
130.93	15.890	4.0
132.70	15.023	4.5
135.33	12.726	4.0
139.65	11.602	4.0
143.90	13.348	7.0
148.09	17.325	5.8
149.74	17.555	6.6
152.21	18.774	4.7
156.28	18.075	5.4
160.31	15.221	25.3

4(+) SCATTERING

ANGLE C.MASS	C.SECT MB/SR	% ERROR REL
18.90	21.207	13.2
25.16	14.435	4.0
31.38	13.396	4.0
37.55	11.549	4.0
43.67	9.382	5.6
49.72	7.771	4.0
55.71	6.756	4.0
61.61	7.247	4.0
67.43	8.788	4.0
73.15	9.049	4.0
78.77	8.390	4.0
84.29	6.966	4.0
89.70	5.665	4.9
94.99	6.691	4.0
100.17	9.367	10.0
105.23	14.388	4.0
110.17	17.468	7.6
114.99	20.352	4.0
119.70	19.405	6.2
128.77	17.017	4.0
141.61	15.065	4.0

INCIDENT ENERGY= 12.257MEV

0(+) SCATTERING

ANGLE C.MASS	C.SECT MB/SR	% ERROR REL
17.98	7634.273	4.0
23.94	1513.976	4.0
29.87	248.152	5.1
35.76	375.385	4.0
41.61	284.187	4.0
47.41	67.933	4.0
53.16	9.455	14.1
58.84	49.507	4.0
64.46	53.017	4.0
70.01	15.433	8.1
75.48	2.551	15.8
80.87	15.859	4.0
86.18	22.562	4.0
91.40	13.407	4.0
96.53	1.935	6.2
101.57	4.618	5.1
106.53	17.832	8.9
111.40	16.874	4.0
116.17	10.735	4.0
120.87	4.856	8.3
125.48	5.668	5.0
130.00	9.423	4.0
131.79	14.899	9.9
134.46	18.865	4.0
138.84	25.412	5.3
143.15	32.883	12.2
147.41	39.369	4.9
149.09	24.976	25.4
151.61	28.296	4.0
155.76	7.502	17.5
159.86	2.226	4.0
163.93	27.719	4.0
165.55	42.371	11.2

2(+) SCATTERING

ANGLE C.MASS	C.SECT MB/SR	% ERROR REL
18.25	46.815	9.0
24.29	85.990	5.1
30.31	90.673	4.0
36.28	57.128	4.0
42.21	20.627	4.0
48.09	8.119	6.6
53.90	15.756	4.0
59.65	23.036	4.0
65.33	21.369	4.0
70.93	12.678	7.7
76.44	9.641	5.8
81.87	10.358	6.1
87.20	13.165	4.0
92.45	12.365	4.5
97.59	11.220	4.0
102.64	8.316	4.0
107.59	8.558	4.3
112.44	10.462	4.0
117.20	14.747	4.0
121.87	15.224	8.9
126.44	16.491	4.0
130.92	13.137	4.0
132.69	12.286	5.3
135.32	10.209	4.0
139.65	9.441	4.0
143.90	11.631	7.7
148.08	14.740	6.2
149.74	15.919	7.2
152.21	16.778	7.0
156.28	17.768	5.2
160.30	14.803	17.3

4(+) SCATTERING

ANGLE C.MASS	C.SECT MB/SR	% ERROR REL
18.90	30.135	14.8
25.15	21.022	5.6
31.37	18.732	6.8
37.54	14.770	4.0
43.66	11.962	4.0
49.71	9.524	11.2
55.69	8.937	4.0
61.60	8.526	5.2
67.41	8.863	4.0
73.14	9.629	4.0
78.76	9.355	4.0
84.27	8.783	5.2
89.68	8.099	4.5
94.97	9.628	5.4
100.15	11.917	4.0
105.21	13.891	4.0
110.15	18.497	4.0
119.68	19.901	4.0
128.75	18.441	5.6
141.59	19.848	4.0

INCIDENT ENERGY= 12.307MEV

0(+) SCATTERING

ANGLE C.MASS	C.SECT MB/SR	% ERROR REL
17.98	7943.953	4.0
23.94	1599.484	4.0
29.87	338.381	4.0
35.76	358.716	4.0
41.61	272.261	4.0
47.41	84.113	4.0
53.16	22.782	4.0
58.84	50.373	4.0
64.46	58.719	4.0
70.01	28.310	4.0
75.48	5.801	6.3
80.87	12.254	4.1
86.18	25.357	4.0
91.40	25.293	4.0
96.53	11.742	4.0
101.57	3.587	6.8
106.53	4.340	7.1
111.40	10.961	4.0
116.17	15.332	4.2
120.87	11.513	4.0
125.48	4.626	4.0
130.00	2.715	7.3
131.79	6.928	4.7
134.46	16.073	4.0
138.84	44.304	4.0
143.15	71.503	4.0
147.41	82.231	4.0
149.09	73.778	4.0
151.61	63.058	4.0
155.76	26.319	4.0
159.86	3.892	8.6
165.55	54.446	4.0

2(+) SCATTERING

ANGLE C.MASS	C.SECT MB/SR	% ERROR REL
18.25	29.968	11.9
24.29	64.718	4.0
30.31	77.642	4.0
36.28	55.988	4.0
42.21	24.003	5.3
48.09	8.844	4.0
53.90	14.420	4.4
59.65	22.655	4.0
65.33	22.611	4.0
70.92	16.680	4.3
76.44	8.491	6.5
81.86	8.159	8.5
87.20	10.874	4.0
92.44	11.832	4.5
97.59	11.348	4.0
102.64	8.595	4.0
107.59	7.332	4.0
112.44	8.393	4.0
117.20	12.193	4.0
121.86	15.872	4.0
126.43	17.124	4.0
130.92	16.902	4.0
132.69	16.149	4.0
135.32	15.108	4.1
139.64	12.244	10.6
143.90	13.288	12.6
148.08	14.871	8.5
149.74	14.657	15.9
152.21	16.707	7.2
156.28	16.337	7.8
160.30	15.278	18.7

4(+) SCATTERING

ANGLE C.MASS	C.SECT MB/SR	% ERROR REL
18.89	30.709	10.2
25.14	23.246	4.0
31.36	18.612	4.0
37.53	16.063	4.0
43.65	14.738	4.0
49.70	12.753	4.3
55.68	11.685	4.0
61.58	10.668	4.0
67.40	9.377	4.0
73.12	9.115	4.0
78.74	9.251	4.0
84.25	9.519	4.0
89.66	9.833	4.0
94.95	9.895	8.9
100.13	12.432	4.0
105.19	13.155	4.6
110.13	13.108	4.0
119.66	11.502	4.0
128.73	7.838	12.9
137.39	9.340	4.6
141.58	11.504	4.0

INCIDENT ENERGY= 12.358MEV

0(+) SCATTERING

ANGLE C.MASS	C.SECT MB/SR	% ERROR REL
17.98	7659.961	4.0
23.94	1601.523	4.0
29.87	322.693	4.0
35.76	322.520	4.0
41.61	244.324	4.0
47.41	89.234	4.0
53.16	19.049	4.5
58.84	38.829	4.0
64.46	50.267	4.0
70.01	26.997	5.6
75.48	2.801	9.6
80.87	6.804	4.0
86.18	25.795	4.0
91.40	35.168	4.0
96.53	25.188	4.0
101.57	10.448	4.0
106.53	4.290	4.0
111.40	8.404	4.0
116.17	12.811	4.0
120.87	12.029	4.0
125.48	7.629	4.0
130.00	7.303	4.1
131.79	9.854	4.0
134.46	17.475	4.0
138.84	36.645	4.0
143.15	54.890	4.0
147.41	57.069	4.0
149.09	57.661	4.0
151.61	46.454	4.0
155.76	25.309	4.0
159.86	11.084	4.0
165.55	24.799	4.0

2(+) SCATTERING

ANGLE C.MASS	C.SECT MB/SR	% ERROR REL
18.25	39.018	9.3
24.29	74.035	4.0
30.30	95.534	4.0
36.28	76.114	4.0
42.21	44.454	4.0
48.08	26.846	4.0
53.90	28.897	4.0
59.65	33.922	4.0
65.32	34.280	4.0
70.92	27.400	6.1
76.43	16.833	4.0
81.86	9.148	8.5
87.20	6.486	4.0
92.44	4.871	8.9
97.58	5.331	5.2
102.63	4.556	6.6
107.58	5.588	4.3
112.43	8.362	4.0
117.19	12.585	4.7
121.86	18.316	4.0
126.43	23.291	4.1
130.91	27.256	4.0
132.68	27.124	4.0
135.32	28.361	4.0
139.64	29.106	4.0
143.89	28.794	7.1
148.08	29.046	10.5
149.73	30.005	7.8
152.20	33.424	8.0
156.28	39.629	4.0
160.30	38.476	8.3

4(+) SCATTERING

ANGLE C.MASS	C.SECT MB/SR	% ERROR REL
18.88	17.042	19.2
25.14	14.176	4.8
31.35	15.005	4.0
37.52	14.263	4.0
43.63	14.799	4.0
49.68	11.616	4.0
55.66	8.227	4.4
61.56	6.583	4.3
67.38	5.867	4.0
73.10	5.352	4.2
78.72	5.095	4.0
84.23	6.071	4.0
89.64	6.765	4.0
94.93	7.587	5.8
100.11	10.326	4.0
105.17	10.948	4.0
110.11	11.685	4.0
119.64	9.596	4.0
141.56	6.980	14.3

INCIDENT ENERGY= 12.404MEV

0(+) SCATTERING

ANGLE C.MASS	C.SECT MB/SR	% ERROR REL
17.98	7189.695	4.0
23.94	1478.277	4.0
29.87	334.082	4.0
35.76	288.636	4.0
41.61	195.679	5.7
47.41	68.291	4.0
53.16	21.096	4.0
58.84	33.144	4.0
64.46	31.920	4.0
70.01	12.139	4.0
75.48	1.001	14.0
80.87	9.490	4.0
86.18	22.584	4.0
91.40	22.598	4.0
96.53	16.797	4.0
101.57	6.835	4.0
106.53	2.655	8.9
111.40	2.319	7.1
116.17	4.214	7.0
120.87	5.116	5.2
125.48	8.043	4.0
130.00	11.241	4.0
131.79	13.550	4.0
134.46	16.780	4.0
138.84	19.030	4.0
143.15	19.371	6.1
147.41	13.204	4.0
149.09	16.130	4.0
151.61	8.472	4.0
155.76	8.335	9.1
159.86	11.611	4.0
165.55	28.083	4.0

2(+) SCATTERING

ANGLE C.MASS	C.SECT MB/SR	% ERROR REL
18.24	59.793	8.4
24.29	98.424	4.0
30.30	125.190	4.0
36.28	107.594	4.0
42.21	69.945	4.0
48.08	44.684	4.0
53.89	38.805	4.0
59.64	44.402	4.0
65.32	47.016	4.0
70.91	41.711	4.0
76.43	30.036	4.0
81.86	17.167	4.0
87.19	8.690	4.0
92.43	7.535	5.2
97.58	10.145	4.0
102.63	13.309	4.0
107.58	12.096	4.0
112.43	10.549	4.0
117.19	12.000	4.0
121.85	19.101	4.0
126.42	29.638	4.0
130.91	39.272	4.0
132.68	38.211	4.0
135.31	39.177	4.0
139.64	33.557	6.7
143.89	32.491	6.5
148.08	32.797	10.7
149.73	44.836	5.6
152.20	45.862	7.2
156.27	64.933	4.0
160.30	74.884	4.6

4(+) SCATTERING

ANGLE C.MASS	C.SECT MB/SR	% ERROR REL
18.88	26.378	10.1
25.13	22.033	7.6
31.34	18.179	4.0
37.51	14.623	4.0
43.62	10.936	4.0
49.67	7.687	4.2
55.65	5.793	4.0
61.55	5.096	4.0
67.36	4.528	4.0
73.08	4.461	7.3
78.70	3.760	4.0
84.21	4.183	4.0
89.62	5.141	4.0
94.91	7.413	6.5
100.09	10.105	4.0
105.15	11.100	4.0
110.09	13.280	4.5
119.62	12.375	4.0
137.36	7.117	4.0

INCIDENT ENERGY= 12.700MEV

0(+) SCATTERING

ANGLE C.MASS	C.SECT MB/SR	% ERROR REL
17.98	6540.301	4.0
23.94	1563.066	4.0
29.87	466.324	4.0
35.76	250.794	4.0
41.61	150.737	4.0
47.41	84.547	4.0
53.16	60.837	4.0
58.85	52.601	4.0
64.46	25.853	4.0
70.01	4.258	5.5
75.48	7.626	4.0
80.87	25.224	4.0
86.18	32.033	4.0
91.40	19.484	7.0
96.53	5.887	4.0
101.58	1.530	6.7
106.53	6.654	4.0
111.40	8.509	4.0
116.17	5.339	4.0
120.87	0.859	8.2
125.48	0.968	7.3
130.01	5.203	4.2
131.80	7.384	5.0
134.46	11.217	4.0
138.84	14.065	4.0
143.15	14.536	4.0
147.41	10.964	4.0
149.09	9.138	4.0
151.61	6.297	4.0
155.76	1.492	5.7
159.86	3.214	4.0
163.93	16.591	4.0
165.55	25.796	4.0

2(+) SCATTERING

ANGLE C.MASS	C.SECT MB/SR	% ERROR REL
18.24	26.170	21.6
24.28	41.043	4.7
30.29	44.445	4.0
36.26	36.536	4.0
42.19	28.293	4.2
48.06	27.109	4.0
53.88	29.219	4.0
59.62	27.788	4.0
65.30	20.549	4.0
70.89	12.247	4.0
76.40	8.148	4.0
81.83	10.513	4.0
87.16	15.785	4.0
92.41	21.223	4.0
97.55	22.258	4.0
102.60	17.306	4.0
107.55	9.126	4.0
112.40	2.790	6.0
117.16	2.599	4.3
121.83	8.109	4.0
126.40	15.091	4.0
130.89	18.744	4.0
132.66	19.915	6.5
135.29	19.005	4.0
139.62	16.861	4.0
143.87	15.480	4.0
148.06	15.262	4.8
149.72	14.183	4.7
152.19	20.483	4.0
156.26	28.941	4.0
160.29	36.374	4.0
164.28	41.568	4.0
165.86	43.810	4.0

4(+) SCATTERING

ANGLE C.MASS	C.SECT MB/SR	% ERROR REL
25.09	7.600	15.4
31.29	9.257	4.0
37.45	8.581	4.0
43.55	6.793	4.0
49.59	4.945	4.6
55.56	3.632	7.2
61.46	3.255	4.0
67.26	3.246	5.4
72.97	3.682	4.0
78.59	3.618	4.0
84.10	3.384	4.0
89.50	3.915	5.5
94.79	6.020	4.0
99.96	9.398	4.0
105.02	12.991	4.0
109.96	17.585	4.0
114.79	21.749	4.0
119.50	23.588	4.0
124.09	23.088	4.5
128.58	22.991	4.6
132.97	21.061	4.0
134.70	18.190	6.5
137.26	19.862	4.0

INCIDENT ENERGY= 13.694MEV

0(+) SCATTERING

ANGLE C.MASS	C.SECT MB/SR	% ERROR REL
17.98	5768.480	4.0
23.94	995.911	4.0
29.87	214.215	4.0
35.76	315.957	4.0
41.61	217.966	4.0
47.42	54.706	4.0
53.16	8.991	19.4
58.85	34.535	4.0
64.47	40.084	4.0
70.01	18.387	4.0
75.48	2.116	14.9
80.87	6.405	4.0
86.18	18.341	4.0
91.40	23.087	4.0
96.53	18.617	4.0
101.58	12.331	4.0
106.53	7.517	4.0
111.40	3.882	4.8
116.18	1.571	7.7
120.87	1.944	5.0
125.48	5.719	4.0
130.01	9.768	4.0
131.80	10.609	4.0
134.46	10.146	4.0
138.84	6.427	4.0
143.16	2.304	6.3
147.41	0.879	7.9
149.10	1.280	5.4
151.61	1.888	6.1
155.76	2.719	4.8
159.86	1.516	5.4
163.93	0.832	6.2
165.55	1.549	4.0

2(+) SCATTERING

ANGLE C.MASS	C.SECT MB/SR	% ERROR REL
18.22	31.169	4.0
24.25	47.808	4.0
30.26	47.117	4.0
36.22	38.894	4.0
42.14	32.947	4.0
48.01	29.197	4.0
53.82	19.898	4.0
59.56	11.231	4.0
65.23	10.372	4.0
70.82	14.424	4.3
76.33	17.053	4.0
81.75	14.026	4.0
87.09	7.645	4.0
92.33	4.899	4.0
97.47	5.997	4.0
102.52	8.982	4.0
107.47	10.757	4.8
112.32	10.853	4.0
117.08	10.251	4.0
121.75	8.988	4.0
126.33	8.124	4.0
130.82	6.606	4.0
132.59	6.077	4.2
135.22	5.335	6.7
139.55	5.418	7.5
143.81	7.178	7.8
148.01	10.083	10.8
149.67	10.882	7.3
152.14	12.235	4.8
156.22	11.764	4.5
160.25	10.500	4.0

4(+) SCATTERING

ANGLE C.MASS	C.SECT MB/SR	% ERROR REL
18.76	13.219	22.6
24.97	17.435	4.0
31.14	18.664	7.0
37.27	20.655	4.0
43.35	16.073	4.0
49.37	9.974	4.0
55.31	4.508	4.0
61.18	3.487	10.4
66.97	6.994	4.2
72.67	10.524	5.9
78.27	12.331	11.2
83.76	12.345	4.0
89.15	11.543	4.0
94.44	11.497	4.0
99.61	12.606	4.0
104.66	14.405	4.0
109.61	15.651	4.0
114.43	14.130	4.0
119.15	10.022	14.7
123.76	9.326	4.0
128.26	9.910	4.0
132.66	11.814	6.0
134.39	15.287	6.8
136.97	18.213	4.0
141.18	22.849	4.0
145.31	27.505	4.0

2(-) SCATTERING

ANGLE C.MASS	C.SECT MB/SR	% ERROR REL
25.24	2.990	5.0
31.48	3.769	4.7
37.67	4.329	7.6
43.81	4.439	11.5
49.88	4.044	8.7
55.88	2.781	6.7
61.80	1.517	4.1
67.63	0.635	7.9
73.37	0.392	11.4
79.00	0.579	10.4
84.53	0.671	8.9
89.94	0.929	11.5
95.24	0.869	7.0
100.42	0.791	9.2
105.48	1.008	9.1
110.42	1.573	8.3
115.24	2.659	6.2
124.52	5.313	4.8
129.00	6.215	4.0

3(-),1(-) SCATTERING

ANGLE C.MASS	C.SECT MB/SR	% ERROR REL
19.21	25.947	9.0
25.57	15.443	6.5
31.89	9.259	4.0
38.16	8.376	4.0
44.37	11.589	4.0
50.52	16.066	4.0
56.58	18.009	4.0
62.56	17.166	4.1
68.45	12.499	7.3
74.23	7.731	6.9
79.91	4.485	4.0
85.47	4.100	5.1
90.91	5.562	4.0
96.23	6.311	4.0
101.42	7.026	4.0
106.49	6.279	4.0

INCIDENT ENERGY= 13.920MEV

0(+) SCATTERING

ANGLE C.MASS	C.SECT MB/SR	% ERROR REL
17.98	5775.809	4.0
23.94	878.513	4.0
29.87	137.187	4.4
35.76	313.283	4.0
41.61	228.309	4.0
47.42	59.757	4.0
53.16	1.348	23.8
58.85	25.368	4.0
64.47	33.078	4.0
70.01	17.091	4.0
75.48	2.464	6.1
80.87	1.075	9.8
86.18	3.665	4.5
91.40	4.125	7.2
96.53	4.804	4.0
101.58	6.487	4.0
106.53	7.051	6.3
111.40	4.861	4.9
116.18	2.135	4.0
120.87	2.211	4.0
125.48	5.428	4.0
130.01	9.048	4.0
134.46	7.804	4.0
138.84	3.942	4.0
143.16	0.972	5.9
147.41	2.084	4.0
151.61	6.113	4.0
155.76	10.937	4.0
159.86	13.038	4.0
163.93	12.785	4.0

2(+) SCATTERING

ANGLE C.MASS	C.SECT MB/SR	% ERROR REL
18.21	26.596	5.8
24.25	46.604	4.0
30.25	52.892	4.0
36.22	39.665	4.0
42.14	20.742	4.0
48.00	19.476	4.0
53.81	14.594	4.0
59.55	11.805	4.0
65.22	11.053	4.0
70.81	10.578	4.0
76.32	9.846	4.0
81.74	8.888	4.0
87.07	8.729	4.0
92.31	8.490	4.0
97.45	6.066	4.0
102.50	4.363	4.9
107.45	4.540	4.0
112.31	7.993	4.0
117.07	12.961	4.0
121.73	15.915	4.0
126.31	12.983	4.0
130.80	7.246	6.9
135.21	2.619	23.9
139.54	2.690	28.4
143.80	8.518	8.9
148.00	16.573	5.4
152.13	23.944	4.0
156.21	27.596	4.0
160.25	25.454	4.0

4(+) SCATTERING

ANGLE C.MASS	C.SECT MB/SR	% ERROR REL
18.74	25.805	7.6
24.95	24.436	4.0
31.11	29.190	4.0
37.24	32.170	4.0
43.31	25.798	11.9
49.32	19.063	4.0
55.27	11.923	4.0
61.13	10.006	4.0
66.91	11.985	4.0
72.61	14.906	4.0
78.20	13.817	4.0
83.70	9.707	4.0
89.09	5.994	4.0
94.37	6.309	4.0
99.54	9.921	4.0
104.59	14.599	4.0
109.54	16.360	4.0
114.36	14.984	4.0
119.08	11.995	4.0
123.69	8.546	4.2
128.20	7.619	4.0
136.91	10.579	4.0
141.13	13.114	4.0
145.26	14.290	4.0
149.32	14.764	4.0
153.31	16.010	4.0
157.23	17.722	4.0

2(-) SCATTERING

ANGLE C.MASS	C.SECT MB/SR	% ERROR REL
25.21	1.625	11.8
49.82	0.494	19.0
55.81	0.598	14.3
61.73	0.748	4.4
67.55	0.639	6.3
73.28	0.777	7.8
78.91	0.803	5.8
84.44	0.771	10.1
89.85	0.593	6.1
95.14	0.319	10.6
105.38	0.495	10.5
110.32	1.233	9.7
115.14	2.366	6.2
119.84	3.312	5.9
124.43	3.847	6.4

3(-),1(-) SCATTERING

ANGLE C.MASS	C.SECT MB/SR	% ERROR REL
19.18	15.104	31.4
25.53	10.123	4.0
31.84	10.046	4.0
38.10	11.238	4.0
44.30	11.807	22.7
50.43	11.580	4.8
56.49	10.054	4.0
62.46	8.356	4.0
68.34	6.659	4.0
74.12	5.979	4.0
79.79	6.247	4.0
85.34	7.280	4.0
90.78	7.859	4.0
96.10	7.049	4.0
101.29	5.982	4.0
106.35	4.486	4.0
111.29	3.398	4.0
116.10	3.558	4.0

INCIDENT ENERGY= 14.094MEV

0(+) SCATTERING

ANGLE C.MASS	C.SECT MB/SR	% ERROR REL
17.98	4956.191	4.0
23.94	826.631	4.0
29.87	250.348	4.0
35.76	297.500	4.0
41.61	172.411	4.0
47.42	37.541	4.0
53.16	15.383	4.0
58.85	35.602	4.0
64.47	29.852	4.0
70.01	8.100	7.3
75.48	3.980	5.4
80.87	15.497	5.1
86.18	21.893	5.8
91.40	14.459	8.2
96.53	5.091	11.4
101.58	0.329	12.9
106.53	1.192	10.8
111.40	2.224	13.6
116.18	2.394	15.5
120.87	2.450	4.0
125.48	3.230	4.6
130.01	3.267	4.1
131.80	2.878	7.0
134.46	1.605	12.7
138.84	0.965	6.5
143.16	3.604	5.9
147.41	9.264	4.0
149.10	10.423	4.0
151.61	11.665	4.0
155.76	10.595	4.0
159.86	5.568	4.0
163.93	3.187	4.0
165.55	4.145	4.0

2(+) SCATTERING

ANGLE C.MASS	C.SECT MB/SR	% ERROR REL
18.21	48.442	9.2
24.24	89.081	4.0
30.25	83.542	9.2
36.21	45.605	4.0
42.13	18.097	4.0
47.99	23.406	4.0
53.80	34.305	4.0
59.54	29.738	4.0
65.21	15.902	4.0
70.80	7.451	4.0
76.30	8.865	4.0
81.73	13.603	4.8
87.06	14.517	4.0
92.30	11.776	4.0
97.44	8.296	4.0
102.49	4.981	4.0
107.44	2.858	16.9
112.29	3.746	13.4
117.05	7.135	7.3
121.72	9.486	4.0
126.30	9.484	4.0
130.79	7.000	6.7
132.56	5.578	12.8
135.20	4.224	15.1
139.53	3.701	20.7
143.79	4.497	15.1
147.99	4.341	22.0
149.65	4.859	17.4
152.12	3.293	25.8
156.20	3.094	18.7
160.24	5.900	6.3
164.24	11.029	4.0

4(+) SCATTERING

ANGLE C.MASS	C.SECT MB/SR	% ERROR REL
24.93	10.568	7.2
31.09	14.712	4.8
37.21	15.972	4.0
43.28	15.866	4.0
49.29	11.675	4.0
55.23	7.753	4.0
61.09	6.351	4.0
66.87	7.461	4.0
72.56	8.493	4.0
78.15	8.258	4.0
83.65	6.523	4.0
89.04	5.098	4.0
94.32	5.753	4.0
99.48	7.370	4.0
104.54	9.680	4.0
109.48	11.521	4.2
114.31	12.551	4.0
119.03	13.707	4.0
123.64	13.839	4.0
128.15	14.595	4.0
132.56	13.878	4.0
134.29	14.372	4.5
136.87	12.836	4.0
141.09	12.892	4.0
145.22	14.126	4.0
149.28	17.860	4.0
150.89	20.180	4.0
153.28	23.641	4.0
157.21	33.271	4.0
161.09	45.119	4.0
166.45	61.576	4.0

2(-) SCATTERING

ANGLE C.MASS	C.SECT MB/SR	% ERROR REL
25.18	4.218	15.7
31.41	2.744	11.9
37.59	1.651	39.2
43.71	1.883	15.7
49.78	2.859	10.8
55.76	3.010	4.9
61.67	2.638	4.0
67.49	2.427	4.0
73.22	2.667	4.0
78.85	2.694	4.0
84.37	2.278	4.9
89.78	1.420	4.3
95.07	0.633	11.8
100.25	0.206	16.5
105.31	0.224	11.6
110.25	0.555	10.1
115.07	1.271	5.0
119.78	2.393	7.6
124.36	2.861	4.1
128.84	3.238	4.0
133.22	2.962	4.7
137.49	2.520	4.4
141.67	1.878	4.9

3(-),1(-) SCATTERING

ANGLE C.MASS	C.SECT MB/SR	% ERROR REL
25.50	9.925	8.9
31.80	9.559	4.5
38.05	11.616	4.0
44.24	12.765	4.0
50.37	10.925	4.0
56.42	8.507	4.7
62.38	6.894	4.0
68.26	7.536	4.0
74.03	8.732	4.0
79.70	9.428	4.0
85.25	8.447	4.0
90.69	6.034	4.6
96.00	4.381	4.0
101.19	3.246	12.8
106.25	2.005	4.0
111.19	2.342	4.0
116.00	2.904	5.4
120.68	3.772	4.0

INCIDENT ENERGY= 14.301MEV

0(+) SCATTERING

ANGLE C.MASS	C.SECT MB/SR	% ERROR REL
17.98	4935.316	4.0
23.94	958.628	4.0
29.87	194.010	4.0
35.76	193.042	4.0
41.61	131.314	4.0
47.42	42.903	4.0
53.16	9.809	21.9
58.85	20.392	4.4
64.47	23.984	4.4
70.01	13.855	4.0
75.48	5.994	8.4
80.87	7.275	20.5
86.18	16.358	5.3
91.40	20.816	4.1
96.53	15.993	6.0
101.58	6.757	5.0
106.53	1.019	9.6
111.40	0.587	7.0
116.18	2.208	9.9
120.87	2.809	4.0
125.48	1.952	13.5
130.01	0.766	29.0
131.80	0.758	33.0
134.46	0.568	18.8
138.84	0.857	27.9
143.16	1.292	26.0
147.41	2.645	22.3
149.10	2.630	10.7
151.61	3.771	14.4
155.76	5.066	5.4
159.86	6.419	4.0
163.93	8.563	8.1
165.55	9.896	7.4

2(+) SCATTERING

ANGLE C.MASS	C.SECT MB/SR	% ERROR REL
18.21	44.500	8.4
24.24	76.895	4.0
30.24	58.897	4.0
36.20	22.187	4.4
42.12	13.171	4.8
47.98	23.936	4.9
53.79	25.906	7.9
59.53	14.622	11.7
65.19	7.201	5.7
70.78	6.811	9.9
76.29	8.454	15.0
81.71	7.178	20.8
87.04	3.394	22.8
92.28	1.691	12.7
97.43	3.263	4.1
102.47	6.454	4.0
107.43	9.513	4.0
112.28	10.697	4.0
117.04	10.530	4.0
121.71	9.022	4.0
126.29	7.155	4.9
130.78	6.026	4.0
132.55	6.165	4.0
135.19	7.132	5.3
139.52	11.488	7.1
143.78	17.684	4.0
147.98	24.377	4.0
149.64	26.455	4.0
152.11	27.992	4.0
156.20	29.691	4.5
160.24	28.460	4.1
164.24	26.574	5.6
165.83	24.833	4.0

4(+) SCATTERING

ANGLE C.MASS	C.SECT MB/SR	% ERROR REL
18.71	19.959	11.5
24.91	19.091	4.0
31.07	18.121	4.0
37.19	16.430	4.0
43.25	12.725	6.0
49.25	9.763	16.3
55.19	6.426	17.4
61.05	5.171	21.0
66.82	3.785	22.2
72.51	3.292	22.1
78.10	2.574	19.1
83.59	2.765	12.6
88.98	3.642	8.7
94.26	4.404	13.0
99.43	5.179	11.3
104.48	5.749	8.3
109.42	5.878	4.0
114.26	5.452	6.4
118.98	5.424	6.8
123.59	5.126	4.0
128.10	5.084	5.2
132.51	5.223	8.8
134.24	4.933	11.6
136.82	5.482	12.2
141.04	5.560	11.2
145.18	5.649	5.7
149.25	7.147	4.6
150.85	7.727	4.0
153.24	9.305	4.0
157.18	13.772	4.0
161.06	19.484	5.0
164.90	27.504	4.0
166.43	30.435	6.7

2(-) SCATTERING

ANGLE C.MASS	C.SECT MB/SR	% ERROR REL
25.16	2.780	21.7
31.38	1.308	23.7
37.55	0.803	26.5
43.67	0.868	18.8
49.73	1.700	15.2
55.71	1.583	9.6
61.61	1.480	8.4
67.43	1.524	7.5
73.15	1.959	5.2
78.78	2.523	4.0
84.29	2.469	6.5
89.70	2.026	7.9
95.00	1.171	10.7
100.17	0.863	11.5
105.23	0.768	12.6
110.17	1.634	6.8
114.99	2.603	7.3
119.70	4.006	5.4
124.29	4.933	5.0
128.77	3.670	7.4
137.42	3.099	4.0
141.61	2.722	4.0
145.70	3.475	4.0

3(-),1(-) SCATTERING

ANGLE C.MASS	C.SECT MB/SR	% ERROR REL
25.46	6.939	14.4
31.75	6.295	6.8
37.99	6.698	8.3
44.18	5.778	13.3
50.30	3.914	13.9
56.34	4.644	4.3
62.30	6.713	4.0
68.17	9.524	4.0
73.94	10.890	4.3
79.60	9.761	4.3
85.15	7.084	4.0
90.58	4.597	6.3
95.89	2.696	4.0
101.08	1.523	4.8
106.14	1.176	19.6
111.08	1.936	18.8
115.89	2.949	4.5

INCIDENT ENERGY= 14.501MEV

0(+) SCATTERING

ANGLE C.MASS	C.SECT MB/SR	% ERROR REL
17.98	4943.012	4.0
23.94	761.987	4.0
26.91	297.229	4.4
29.87	211.867	4.0
35.76	250.928	4.0
41.61	119.643	4.0
47.42	12.326	6.1
50.30	4.133	18.2
53.16	16.593	4.0
58.85	43.600	4.0
64.47	36.127	4.0
70.01	8.952	4.0
72.76	1.362	14.4
75.48	2.029	10.1
80.87	24.917	4.0
86.18	52.480	4.0
91.40	54.637	4.0
96.54	30.937	4.0
101.58	7.733	4.0
106.53	5.305	4.0
111.40	16.344	4.0
116.18	21.839	4.0
120.87	15.178	4.0
125.48	4.727	4.6
130.01	2.006	7.5
131.80	3.206	5.3
134.46	5.813	4.0
138.84	8.760	4.0
143.16	7.013	4.0
147.41	2.390	4.1
149.10	1.130	8.3
151.61	0.137	21.2
155.76	0.695	9.4
159.86	1.603	5.8
163.93	1.425	4.0
165.55	1.005	6.3

2(+) SCATTERING

ANGLE C.MASS	C.SECT MB/SR	% ERROR REL
18.20	50.703	6.9
24.23	83.885	4.0
27.24	81.963	4.0
30.23	63.514	4.0
36.20	24.659	4.0
42.11	15.490	4.0
47.98	26.493	4.0
50.89	29.266	4.0
53.78	27.149	4.0
59.52	14.959	4.0
65.18	5.064	4.0
70.77	3.952	4.0
73.54	5.721	4.0
76.28	6.718	4.0
81.70	8.173	4.0
87.03	7.635	4.0
92.27	5.524	4.0
97.41	3.592	4.0
102.46	4.630	4.0
107.41	6.968	4.0
112.27	7.908	4.0
117.03	7.012	4.0
121.70	4.383	5.0
126.27	3.946	5.7
130.77	6.396	5.9
132.54	8.399	4.0
135.18	9.444	4.0
139.51	9.823	4.0
143.77	7.737	4.0
147.97	4.626	5.9
149.63	4.558	5.3
152.11	6.024	4.0
156.19	11.252	4.0
160.23	18.841	4.0
164.23	26.847	4.0

4(+) SCATTERING

ANGLE C.MASS	C.SECT MB/SR	% ERROR REL
18.70	28.334	13.5
24.89	19.610	4.0
27.97	18.821	4.0
31.05	18.455	4.0
37.16	18.141	4.0
43.22	16.031	4.0
49.22	11.626	4.0
52.19	10.318	4.0
55.15	8.891	4.0
61.00	9.508	4.0
66.78	12.535	4.0
72.46	14.673	4.0
75.27	14.293	4.0
78.05	13.429	4.0
83.54	9.126	4.0
88.92	5.087	4.0
94.20	4.740	4.0
99.37	6.931	4.0
104.42	10.741	4.0
109.37	12.352	4.0
114.20	12.107	4.0
118.92	11.559	4.0
123.54	9.689	4.0
128.05	8.704	4.0
132.46	8.325	4.0
134.19	7.883	4.0
136.77	8.034	4.0
141.00	8.217	4.1
145.14	10.773	4.0
149.21	13.788	4.0
150.82	14.971	4.0
153.21	18.076	4.0
157.15	24.140	4.0
161.04	30.524	4.0
164.89	36.864	5.4
166.41	38.357	5.9

2(-) SCATTERING

ANGLE C.MASS	C.SECT MB/SR	% ERROR REL
25.13	6.119	7.4
28.24	4.841	6.4
31.35	3.391	10.2
37.51	2.863	10.6
43.63	3.397	5.9
49.68	3.683	4.0
52.68	3.532	4.0
55.65	2.757	4.0
61.55	1.211	5.8
67.37	0.328	9.1
73.09	0.580	6.2
75.91	0.798	7.3
78.71	1.375	5.4
84.22	1.884	9.2
89.63	1.562	6.9
94.92	0.943	6.3
100.09	0.432	12.4
110.09	0.684	8.6
114.92	1.316	7.5
119.62	2.715	9.2
137.36	5.678	4.0
141.55	4.548	9.7
145.65	3.857	7.0
149.67	3.128	4.7
151.26	2.676	6.6

3(-),1(-) SCATTERING

ANGLE C.MASS	C.SECT MB/SR	% ERROR REL
25.42	6.914	4.0
28.57	6.402	4.0
31.71	5.186	4.0
37.94	3.402	4.0
44.12	2.528	4.0
50.23	2.763	8.4
53.26	4.259	4.0
56.27	3.862	4.0
62.22	4.085	4.0
68.08	4.085	5.9
73.84	3.605	4.2
76.69	3.160	13.1
79.50	2.880	4.0
85.05	2.092	4.0
90.48	1.593	9.9
95.79	1.212	5.4
100.97	1.393	6.3
106.04	1.964	5.0
110.97	3.008	4.1
115.79	3.935	5.1

INCIDENT ENERGY= 14.700MEV

0(+) SCATTERING

ANGLE C.MASS	C.SECT MB/SR	% ERROR REL
17.98	5033.012	4.0
23.94	688.148	4.0
29.87	229.954	4.0
35.76	258.552	4.0
41.61	104.462	4.0
47.42	8.588	7.3
53.16	14.946	4.0
58.85	31.171	4.0
64.47	25.116	4.0
70.01	11.470	4.0
75.48	2.536	5.7
80.87	10.797	4.0
86.18	32.624	4.0
91.40	46.558	4.0
96.54	35.345	4.0
101.58	13.570	4.0
106.53	2.230	8.2
111.40	6.258	4.0
116.18	12.050	4.0
120.87	9.601	4.0
125.48	3.477	4.1
130.01	2.003	4.7
131.80	3.887	4.0
134.46	5.284	5.9
138.84	7.635	4.0
143.16	5.638	4.1
147.41	1.942	4.0
149.10	1.565	4.0
151.61	1.848	5.1
155.76	5.224	4.0
159.86	9.998	4.0
163.93	11.104	4.0
165.55	9.088	4.0

2(+) SCATTERING

ANGLE C.MASS	C.SECT MB/SR	% ERROR REL
18.20	64.586	4.0
24.23	89.101	4.0
30.23	49.249	4.0
36.19	12.371	4.0
42.11	26.664	4.0
47.97	49.974	4.0
53.77	39.413	4.4
59.51	10.830	4.0
65.17	1.213	10.4
70.76	8.505	4.0
76.27	12.549	4.0
81.69	9.302	4.0
87.02	5.992	5.2
92.26	7.128	4.0
97.40	7.687	4.0
102.45	6.187	4.0
107.40	4.131	4.0
112.25	5.162	4.0
117.02	8.385	4.0
121.68	11.907	4.0
126.26	10.713	4.0
130.76	7.990	4.0
132.53	6.691	4.0
135.17	7.206	4.0
139.50	8.132	4.0
143.76	10.366	4.0
147.96	11.313	4.0
149.62	11.391	4.0
152.10	12.245	4.0
156.18	12.025	4.0
160.22	14.688	4.0
164.23	17.427	4.0
165.82	18.992	4.0

4(+) SCATTERING

ANGLE C.MASS	C.SECT MB/SR	% ERROR REL
24.87	5.423	7.9
31.02	5.426	6.3
37.13	5.829	4.0
43.19	4.602	4.5
49.18	4.342	4.0
55.11	5.780	4.0
60.96	8.167	4.0
66.73	9.327	4.0
72.42	7.902	4.0
78.00	5.750	4.0
83.49	4.499	4.0
88.87	5.568	4.9
94.15	8.326	4.0
99.32	11.666	4.0
104.37	13.545	4.0
109.31	12.958	4.0
114.15	11.471	4.0
118.87	10.108	4.0
123.49	10.626	4.0
128.00	13.212	4.0
132.41	18.093	4.0
134.15	20.340	4.0
136.73	21.332	4.0
140.96	22.507	4.0
145.11	20.701	4.0
149.18	17.790	4.0
150.79	16.285	4.0
153.18	12.640	4.0
157.13	9.667	4.8
161.02	7.748	14.1
164.87	10.907	9.5
166.40	11.933	22.4

2(-) SCATTERING

ANGLE C.MASS	C.SECT MB/SR	% ERROR REL
18.86	27.335	11.5
25.11	19.000	5.5
31.32	9.190	4.0
37.48	3.329	6.2
43.59	3.056	5.8
49.63	5.908	4.0
55.60	7.913	4.0
61.50	7.610	4.0
67.31	5.176	4.0
73.02	2.175	4.0
78.64	0.870	5.6
84.15	1.162	4.3
89.56	2.001	4.0
94.85	2.083	4.0
100.02	1.332	5.1
105.08	0.636	7.6
110.02	0.328	18.7
114.84	0.543	9.2
119.55	0.821	8.9
124.15	1.465	6.9
128.64	1.642	6.4
133.02	2.710	4.1
137.30	2.700	5.1
141.49	3.013	4.9
145.60	3.104	4.6
149.62	3.552	4.0
151.21	3.881	4.0
153.58	3.113	4.0
157.47	2.547	4.5

3(-),1(-) SCATTERING

ANGLE C.MASS	C.SECT MB/SR	% ERROR REL
19.08	44.478	8.6
25.39	29.702	4.0
31.67	20.158	4.0
37.89	14.495	4.0
44.07	11.884	4.0
50.17	10.526	4.0
56.20	8.286	4.0
62.15	5.363	4.2
68.00	2.888	4.3
73.76	2.127	6.2
79.41	2.386	7.0
84.96	2.634	4.0
90.38	2.814	4.0
95.69	3.189	4.0
100.88	3.631	4.0
105.94	4.600	4.0
110.88	5.432	4.0
115.69	6.054	4.0
120.38	6.008	5.7
138.00	8.356	4.0

INCIDENT ENERGY= 14.902MEV

0(+) SCATTERING

ANGLE C.MASS	C.SECT MB/SR	% ERROR REL
17.98	4998.516	12.0
23.94	773.765	4.0
29.87	260.624	4.0
35.76	160.873	4.0
41.62	61.475	4.0
47.42	30.602	4.0
53.16	40.484	4.0
58.85	31.454	4.0
64.47	8.098	4.0
70.01	1.258	10.7
75.48	12.224	4.0
80.88	22.881	4.0
86.18	19.616	4.0
91.40	8.398	4.0
96.54	1.538	10.8
101.58	3.717	4.0
106.53	8.764	4.0
111.40	9.208	4.5
116.18	4.837	4.0
120.87	0.615	8.4
125.48	0.841	5.9
130.01	3.361	4.0
131.80	4.195	4.0
134.46	4.720	4.0
138.84	3.049	4.0
143.16	1.160	4.7
147.41	0.834	5.4
149.10	1.319	5.8
151.61	2.084	4.0
155.76	3.011	4.0
159.86	2.897	4.0
163.93	2.271	4.0
165.55	2.511	4.0

2(+) SCATTERING

ANGLE C.MASS	C.SECT MB/SR	% ERROR REL
18.20	79.014	9.9
24.23	91.501	4.0
30.22	47.446	4.0
36.18	11.487	5.1
42.10	22.007	4.0
47.96	41.471	4.0
53.76	34.494	4.0
59.50	16.283	4.0
65.16	4.531	4.0
70.75	5.966	4.0
76.26	11.119	4.0
81.68	11.168	4.0
87.01	6.149	4.0
92.24	2.381	4.5
97.39	4.728	4.4
102.43	10.178	4.0
107.39	13.124	4.0
112.24	10.616	4.0
117.00	5.987	6.7
121.67	3.655	6.8
126.25	4.755	5.4
130.75	6.614	4.0
132.52	7.583	4.0
135.16	7.705	4.0
139.49	7.587	4.0
143.76	6.935	4.0
147.95	7.147	5.6
149.62	7.459	5.5
152.09	7.494	4.0
156.18	8.891	4.0
160.22	11.039	4.0
164.22	13.348	4.0
165.81	14.102	4.0

4(+) SCATTERING

ANGLE C.MASS	C.SECT MB/SR	% ERROR REL
18.67	39.527	14.5
24.85	38.080	4.0
31.00	32.890	4.0
37.11	20.017	4.0
43.16	12.210	4.0
49.15	11.505	4.0
55.08	15.016	4.0
60.92	18.705	4.0
66.69	18.828	4.0
72.37	17.655	4.0
77.96	15.734	4.0
83.44	14.465	4.0
88.82	13.212	4.0
94.10	10.875	4.0
99.26	9.086	4.0
104.32	8.130	4.0
109.26	8.118	4.0
114.10	8.241	5.2
118.82	8.162	4.0
123.44	8.475	4.0
127.95	8.874	4.0
132.37	10.242	4.0
134.10	10.952	4.0
136.69	12.146	4.0
140.92	12.631	4.0
145.07	12.787	4.0
149.14	13.762	4.0
150.76	14.956	4.0
153.15	14.925	4.0
157.10	19.131	4.0
161.00	23.723	4.6
164.85	28.806	8.5

2(-) SCATTERING

ANGLE C.MASS	C.SECT MB/SR	% ERROR REL
25.08	5.457	10.4
31.29	3.226	5.3
37.44	1.525	11.3
43.55	1.054	8.1
49.59	1.434	5.6
55.56	1.215	4.0
61.45	1.186	4.0
67.25	0.963	4.0
72.96	0.553	6.6
78.58	0.283	15.6
84.09	0.279	17.0
89.49	0.535	6.0
94.78	0.722	5.4
99.95	0.590	5.7
105.01	0.351	10.6
109.95	0.138	9.6
114.78	0.403	14.2
119.49	0.660	25.6
124.08	0.664	8.3
128.57	0.903	6.7
132.96	1.240	5.2
134.68	1.371	6.8
137.25	1.903	4.0
141.44	2.394	4.0
145.55	2.892	4.0
149.58	2.791	4.0
151.17	2.849	4.4
153.54	2.624	4.0
157.44	2.993	4.0

3(-),1(-) SCATTERING

ANGLE C.MASS	C.SECT MB/SR	% ERROR REL
25.36	8.842	9.8
31.63	8.853	4.1
37.85	11.511	4.0
44.01	12.364	4.0
50.11	10.160	4.0
56.13	5.780	4.0
62.07	2.615	10.7
67.93	1.184	10.1
73.68	2.146	4.0
79.33	3.919	4.0
84.87	5.090	4.0
90.29	4.980	4.6
95.60	3.790	5.6
100.78	2.842	4.5
105.84	3.043	4.0
110.78	4.481	4.0
115.59	7.006	4.0
120.29	8.993	4.0
137.92	11.882	4.0
142.07	12.856	4.0

Appendix V

The automatic search code, JIB 3, written by F.G. Perey (unpublished) and the coupled channels code, Jupitor-1, written by T. Tamura (ORNL-4152 unpublished), were subject to some modifications by the author.

(a) JIB 3

In addition to the coding necessary for the calculations described in chapter 7 the following options were incorporated :

(i) 4-parameter potential (V, R, W, a) in addition to the original option of 6-parameters;

(ii) automatic one/two dimensional grids with search optional at each grid point; and

(iii) plotting routine.

The code was satisfactorily checked against several sets of test data as well as against the elastic scattering predictions of Jupitor-1.

(b) Jupitor-1

As this code was originally prepared for a CDC-1604 computer in which the word length is 48 bits, the major alteration was to use double precision word lengths of 64 bits as an alternative to the standard word length of 32 bits of the IBM 360/50 computer. This required substantial re-arrangement of the COMMON block and an overlay of the two fairly well defined segments of the code. The plotting routine was also modified to enable plotting of differing ranges of angles for each state. A full description of the code is given in the unpublished report ORNL-4152, together with several sets of test data, which were used for final checking purposes. As an additional check of the code a calculation performed using the standard calculation of table 6.1 was submitted to Dr Tamura for execution via the original code; the cross sections of the two calculations agreed to within 0·1%.

REFERENCES

Al 63 E. Almqvist, D.A. Bromley, J.A. Kuehner and B. Whalen; Phys. Rev. 130 (1963) 1140.

Al 67 J.P. Aldridge, J. John, C.P. Robinson, W.J. Wallace, K.R. Chapman and R.H. Davis; Bull. Am. Phys. Soc. 12 (1967) 462.

Al 68 J.P. Aldridge, G.E. Crawford and R.H. Davis; Phys. Rev. 167 (1967) 1053.

Au 62 N. Austern, R.M. Drisko, E. Rost and G.R. Satchler; Phys. Rev. 128 (1962) 733.

Au 65 N. Austern; Proc. of Summer Study Group on Physics of Emperor Tandem van de Graaff Region - Brookhaven Rpt. BNL-948, (1965) p. 527.

Ba 64 W.H. Barkas and M.J. Berger; Studies of Penetration of Charged Particles in Matter, National Acad. Sciences - National Res. Council Publication 1133 (1964) p. 103.

Bi 66 F.W. Bingham; Preprint; and Bull. Am. Phys. Soc. 10 (1965) 539.

Bl 64 J.S. Blair, N. Cue, G.W. Farwell and D. Shreve; Annual Prog. Rpt. Univ. Washington (1964) p. 8.

Bl 65 J.S. Blair; Lectures in Theoretical Physics Vol VIIIC, Univ. of Colorado Press (1965) p. 343.

Bo 53 A. Bohr and B.R. Mottleson; Mat. Fys. Medd. 27 (1963) No 16.

Br 60 G.E. Brown; Proc. Int. Conf. on Nucl. Structure ed. D.A. Bromley and E.W. Vogt, Univ. of Toronto Press, (1960) p. 135.

Br 64 G.E. Brown; Unified Theory of Nuclear Models, North Holl. Pub. Co. (1964).

Br 65 H.W. Broek, Y.L. Yntema, B. Buck and G.R. Satchler; Nuc. Phys. 64 (1965) 259.

Br 67 K.H. Bray; Ph.D. Thesis, Australian National University, (1967) unpublished.

Bu 63 B. Buck; Phys. Rev. 130 (1963) 712; and B. Buck, A. P. Stamp and P.E. Hodgson; Phil. Mag. 8 (1963) 1805.

Ca 62 E.B. Carter; Ph.D. Thesis, Florida State University, (1962) unpublished.

Ca 64 E.B. Carter, G.E. Mitchell and R.H. Davis; Phys. Rev. 133 (1964) B1421.

Ch 58 D.M. Chase, L. Wilets and A.R. Edmonds; Phys. Rev. 110 (1958) 1080.

Cl 60 R.L. Clarke, E. Almqvist and E.B. Paul; Nuc. Phys. 14 (1960) 472.

Da 63 R.H. Davis; Proc. of Third Conf. on Reactions between Complex Nuclei, ed. A. Ghiroso, R.M. Diamond and H.E. Conzett, Univ. of California Press, (1963) p. 61.

Da 66 R.H. Davis; Symposium on Recent Progress in Nucl. Phys. with Tandems, Heidelberg (1966), Preprint.

Dr 63 R.M. Drisko, G.R. Satchler and R.H. Bassel ; Phys. Letts. 5 (1963) 347.

Ei 62 W.W. Eidson and J.G. Cramer; Phys. Rev. Letts. 9 (1962) 497.

Ei[1] 62 W.W. Eidson and R.D. Bent; Phys. Rev. 128 (1962) 1312.

Er 66 T. Ericson and T. Mayer-Kuckuk; Ann. Rev. Nucl. Sci. 16 (1966) 199.

Ev 61 F. Everling, L.A. Koenig, J.H.E. Mattouch and A.H. Wapstra; U.S.A. A.E.C. Nucl. Data Tables (1961).

Ev 65 H.C. Evans, M.A. Eswaran, H.E. Gove, A.E. Litherland, and C. Broude; Can. J. Phys. 43 (1965) 82.

Fu 68 C.B. Fulmer, J.B. Benveniste and A.C. Mitchell; Phys. Rev. 165 (1968) 1218.

Gl 67 N.K. Glendenning; Int. School of Physics 'Enrico Fermi' Course XL, Academic Press (1967).

Go 60 H.E. Gove; Proc. Int. Conf. on Nucl. Structure ed. D.A. Bromley and E.W. Vogt, Univ. of Toronto Press (1960) p. 438.

Go 65 H.E. Gove; Proc. of Summer Study Group on Physics of Emperor Tandem van de Graaff Region - Brookhaven Rpt. BNL-948, (1965) p. 361.

Ha 66 H. Hay; Australian National University, (1966) unpublished.

Ha 68 H. Hay; Australian National University, (1968) unpublished.

He 68 D.L. Hendrie, N.K. Glendenning, B.G. Harvey, O.N. Jarvis, H.H. Duhm, J. Saudinos and J. Mahoney; Phys. Letts. 26B (1968) 127.

Ho 63 P.E. Hodgson; Optical Model of Elastic Scattering, Oxford Univ. Press (1963).

Ho 66 C.N. Holbrow and R. Middleton; Univ. of Pennsylvania Report (1966) unpublished.

Ho[1] 66 P.E. Hodgson; Advances in Physics 15 (1966) 329.

HV 65 High Voltage Corporation Memorandum; Dec 1965.

Ig 59 G. Igo; Phys. Rev. 115 (1959) 1665 and Phys. Rev. Letts. 1 (1958) 72.

Iv 67 M. Ivascu, G. Semenescu, M. Titirici and E. Marincu; Rev. Roum. Phys. 12 (1967) 525 and Private Communication.

Ki 65 H.J. Kim; Phys. Letts. 19 (1965) 296.

Ko 64 J. Kokame, K. Fukunaga, H. Nakamura, and N. Inoue; Phys. Letts. 8 (1964) 342.

Ko 65 J. Kokame, K. Fukunaga, H. Nakamura and N. Inoue; J. Phys. Soc. Japan 20 (1965) 475.

Ku 60 J.A. Kuehner, B. Whalen, E. Almqvist and D.A. Bromley; Proc. of Int. Conf. on Nucl. Structure, ed. D.A. Bromley and E.W. Vogt, Univ. of Toronto Press, (1960) p. 261.

La 58 A.M. Lane and R.G. Thomas; Rev. Mod. Phys. 30 (1958) 257.

Li 61 A.E. Litherland, J.A. Kuehner, H.E. Gove, M.A. Clark and E. Almqvist; Phys. Rev. Letts. 7 (1961) 98.

Li 65 A.E. Litherland; Nuclear Structure and Electromag. Interactions, ed. N. MacDonald, Oliver and Boyd, (1965) p. 136.

Lo 66 J. Lowe and D. Watson; Phys. Letts. 23 (1966) 261.

Lu 66 B.T. Lucas, S.W. Cosper and O.E. Johnson; Phys. Rev. 144 (1966) 972.

Ma 67 J.B. Marion and B.A. Zimmerman; Nucl. Inst. 51 (1967) 93.

Mc 65 I. McCarthy; Lectures in Nuclear Physics, Univ. of Oregon, (1965) unpublished.

Mc 66 L. McFadden and G.R. Satchler; Nucl. Phys. 84 (1966) 177.

Me 65 M.A. Melkanoff, J. Raynall and T. Sawada; Methods of Computational Physics V (1965).

Me 67 M.K. Mehta, W.E. Hunt and R.H. Davis; Phys. Rev. 160 (1967) 791.

Mi 64 G.E. Mitchell, E.B. Carter and R.H. Davis; Phys. Rev. 133 (1964) B1434.

Mi 67 R. Middleton; Univ. of Pennsylvania Report, (1967) unpublished.

Mo 65 P.A. Moldauer; Proc. of Summer Study Group on Physics of Emperor Tandem van de Graaff Region - Brookhaven Rpt. BNL-948, (1965) p. 527.

Mo 67 J.M. Morris; Ph.D. Thesis, Australian National University (1967) unpublished; and J.M. Morris and T.R. Ophel; Nuc. Inst. 40 (1966) 245.

Mo[1] 67 P.A. Moldauer; Phys. Rev. Letts. 18 (1967) 249.

Na 68 I. M. Naqib and J.S. Blair; Phys. Rev. 165 (1968) 1250.

Oh 64 G.H. Ohlsen and P.G. Young; Nucl. Phys. 52 (1964) 134.

Ok 62 S. Okai and T. Tamura; Nucl. Phys. 31 (1962) 185.

Pa 65 M.K. Pal; Lectures on Nuclear Structure and Levels, Australian National University, (1965) unpublished.

Pe 63 F.G. Percy and G.R. Satchler; Phys. Letts. 5 (1963) 212.

Pr 62 M.A. Preston; Physics of the Nucleus, Addison-Wesley (1962) p. 485.

Ro 63 E. Rost; Phys. Rev. 128 (1962) 2708.

Ro 67 F.A. Rose, P.B. Tollefsrud and H.T. Richards; Bull. Am. Phys. Soc. 12 (1967) 29.

Sa 60 G.R. Satchler; Oak Ridge Lab. Rpt. ORNL-2861 (1960).

Sa 65 G.R. Satchler; Nucl. Phys. 70 (1965) 177.

Sa[1] 65 G.R. Satchler; Lectures in Theoretical Physics, Vol VIIIC, Univ. of Colorado Press (1965) p. 73.

Sc 65 J.P. Schiffer; Proc. of Summer Study Group on Physics of Emperor Tandem van de Graaff Region - Brookhaven Rpt. BNL-948, (1965) p. 477.

Se 58 L. Seidlitz, E. Bleuler and D.J. Tendham; Phys. Rev. 110 (1958) 682.

Se 64 S.M. Seltzer and M.J. Berger; Studies of Penetration of Charged Particles in Matter, National Acad. Sciences - National Res. Council Publication 1133 (1964) p. 187.

Si 59 E.A. Silverstein; Nucl. Inst. 4 (1959) 53.

Si 66 P.P. Singh, B.A. Watson, J.J. Kroepfl and T.P. Martin; Phys. Rev. Letts. 17 (1966) 17.

So 66 S.S. So, C. Mayer-Boricke and R.H. Davis; Nucl. Phys. 84 (1966) 641.

Sp 65 A. Springer; Ph.D. Thesis, Univ. of California, (1965) unpublished; and Phys. Rev. Letts. 14 (1965) 538.

St 65 P.H. Stelson and L. Grodzens; Nucl. Data A1 (1965) 21.

Ta 64 T. Tamura and T. Teresawa; Phys. Letts. 8 (1964) 41.

Ta 65 T. Tamura; Rev. Mod. Phys. 37 (1965) 679.

Ta^1 65 T. Tamura; Nucl. Phys. 73 (1965) 24.

Ta 67 T. Tamura; Oak Ridge Report ORNL-4152, (1967) unpublished.

Ta^1 67 M. Takeda, S. Kato and T. Yamazaki; Contributions to Int. Conf. on Nucl. Structure (Tokyo 1967) p. 280.

Th 67 W.J. Thompson, G.E. Crawford and R.H. Davis; Nucl. Phys. A98 (1967) 228.

Vo 64 E.W. Vogt, D. McPherson, J.A. Kuehner and E. Almqvist; Phys. Rev. 136 (1964) B99.

Wa 66 B.A. Watson, B.M. Barden, W.W. Eidson, J.J. Kroepfl and P.P. Singh, Preprint (1966).

Wh 63 W. Whaling; Handbuch der Physik XXXIV (1963).

Wi 39 E.J. Williams; Proc. Roy. Soc. (London) A169 (1939) 531.

Wi 66 C. Williamson and J.P. Boujot; Energy Loss Tables C.E.A. - R3042, (1966).

Wu 62 T.Y. Wu and T.H. Ohmura; Quantum Theory of Scattering, Prentice-Hall, (1962) p. 443.

Yo 65 P.G. Young; Ph.D. Thesis, Australian National University, (1965) unpublished.